



ЕЛЕКТРОТЕХНИЧКИ ФАКУЛТЕТ
УНИВЕРЗИТЕТА У БАЊАЛУЦИ

FACULTY OF ELECTRICAL ENGINEERING
UNIVERSITY OF BANJALUKA

ЕЛЕКТРОНИКА *ELECTRONICS*

ГОДИШТЕ 3, БРОЈ 2, ДЕЦЕМБАР 1999. • VOLUME 3, NUMBER 2, DECEMBER 1999.

FACULTY OF ELECTRICAL ENGINEERING BANJALUKA

Address: Patre 5, 78000 Banjaluka, Republic of Srpska, Bosnia and Herzegovina
Phone: +387 51 211 408, +387 51 212 002
Fax: +387 51 211 408

ELECTRONICS

Editor: Prof. Branko L. Dokić Ph. D.
Faculty of Electrical Engineering, University of Banjaluka
Republic of Srpska
e-mail: bdokic@etf-bl.rstel.net

Program Committee:

- Nikolaos Uzunoglu, National Technical University of Athens, Greece
- Barry Jefferies, University of Hertfordshire, UK
- Vojin Oklobdzija, University of California, Davis, USA
- Bratislav Milovanović, Faculty of Electronics Niš, FR Yugoslavia
- Milić Stojić, Faculty of Electrical Engineering Beograd, FR Yugoslavia
- Vojislav Arandelović, Institute "Vinča" Beograd, FR Yugoslavia
- Veljko Milutinović, Faculty of Electrical Engineering Beograd, FR Yugoslavia
- Ilija Stojanović, SANU Beograd, FR Yugoslavia
- Vladimir Katić, Faculty of Technical Science Novi Sad, FR Yugoslavia
- Aleksandar Ilišković, Faculty of Electrical Engineering Banjaluka, RS
- Milorad Božić, Faculty of Electrical Engineering Banjaluka, RS

Secretary: Goran Ninković, M. Sc., Faculty of Electrical Engineering
University of Banjaluka, Republic of Srpska
e-mail: ngogi@etf-bl.rstel.net

Language editors: Milena Mandić
Radomir Kosić

Publisher:

Faculty of Electrical Engineering, University of Banjaluka, Republic of Srpska
Address: Patre 5, 78000 Banjaluka
Phone: +387 51 211 408, +387 51 212 002
Fax: +387 51 211 408

Printed in:

GLAS - SRPSKI, Banjaluka
Number of printed copies: 300

BIOGRAPHY OF PROF. BRATISLAV MILOVANOVIĆ



Prof. Bratislav Milovanović was born in Rosica, Serbia, in 1948. He received the B.S., M.Sc. and the Ph.D. degrees from the Faculty of Electronic Engineering, University of Niš in 1972, 1975 and 1979, respectively. From 1979 till 1985 he worked as a research fellow, research assistant, assistant and assistant professor at the same faculty. In 1985, he was extraordinarily promoted to associate professor, and in 1990 he became a full professor. From 1994, he is a Head of the Department of Telecommunications.

As a research fellow and teacher he participated in the realization of the teaching process of 12 subjects at the undergraduate studies and 11 subjects at the postgraduate studies. He founded a teaching laboratory (Laboratory for hyperfrequencies), as well as a research laboratory (Laboratory for microwave technique and satellite television). Prof. Milovanović is an author of two textbooks. He supervised 4 PhD theses, 10 MSc theses and about 80 diploma papers.

The main areas of his scientific interests are microwave technique and satellite communications. He is the author of 245 scientific papers, and 28 of them were published in the world-known journals, 70 papers were presented at the international conferences, 13 papers were published in the Yugoslav journals, etc. Also, he is an editor of 4 proceedings of conferences (2 of them are the international ones). He is a reviewer of many world-leading international journals and conferences, a member of the Editorial Board of the international journal "Facta Universitatis - Series: Electronics and Energetics" and the journal "Electronics" (Republic of Srpska). As a chairman or member of the program committees, he gave the significant contribution to the organization of scientific conferences and meetings (TELSIKS, TELFOR, ETRAN, YU INFO, JUŽEL).

Prof. Milovanović was a head of over 20 projects in the field of fundamental and applied researches. According to the criterion of the Ministry of Science and Technology of the Republic of Serbia, he is one of the most successful researchers in the field of electrical engineering and information technologies.

In 1993, Prof. Milovanović organized the conference on telecommunications in modern satellite, cable and broadcasting services - TELSIS, which is an International IEEE conference from 1997 and gathers a great number of international and Yugoslav experts. Prof. Milovanović is a member of several international and national organizations and societies. He was a vice-dean in the period from 1989-1991, and a dean from 1994-1998. He is a President of the Administrative Committee of Ei-Holding Co. Niš. He was a member and vice-president of the Board for Electrical Engineering in the Ministry of Science and Technology of the Republic of Serbia.

Prof. Milovanović was awarded many prizes, such as the annual prize of Radio-television Belgrade, the October prize of the town of Niš for results achieved in the development of SATV equipment, the medallion of the University of Niš, and many others.

P R E F A C E

I would like to express my great pleasure as well as to emphasize that I am honored by the invitation of the Dean of the Faculty of Electrical Engineering in Banjaluka, Prof.Dr. Branko Dokić, the editor of the journal Electronics, the scientific periodical of the University in Banjaluka, to be a guest-editor of this issue of this journal.

The collaboration between the Faculty of Electrical Engineering in Banjaluka and the Faculty of Electronic Engineering in Niš is an example of a really successful cooperation through many years. This has begun with the collaboration of fellow students of these faculties, through the participation in training the teaching staff, and up to the partnership in scientific-research activities. Here, I would like to emphasize the participation of teachers and associates of these two faculties in the scientific conferences (Industrial Energetics, MIEL, and TELSIS).

The teachers and associates of the Faculty of Electrical Engineering in Banjaluka were the permanent participants of the TELSIS conferences, and their papers were very interesting for the scientists from the whole world. As the result of their continuous and successful participation in TELSIS conferences, as the guest-editor of this issue of the journal Electronics and the Programme Committee Chairman of the international IEEE Scientific Conference TELSIS'99, I have decided to select the papers from this year's Conference.

The 4th International IEEE Conference on Telecommunications in Modern Satellite, Cable, and Broadcasting Services - TELSIS'99 was held at the Faculty of Electronic Engineering of the University of Niš, Yugoslavia, from October 13 through 15, 1999. Starting from the first TELSIS Conference held in 1993, up to this year's Conference, the scientific and organizing levels of TELSIS conferences were in the continuous ascent. The latest TELSIS Conference, held in the extremely bad post-war conditions, had a really high scientific level, 148 papers were accepted for presentation (23 of them were invited papers by the authors from 20 countries). The technical sponsorships were obtained from IEEE Microwave Theory and Technique Society (MTT-S), Antennas and Propagation Society (AP-S), IEEE Communications Society (ComSoc), and IEEE Region 8 as well. In addition, for the first time, the Conference Proceedings is accepted as an IEEE publication this year.

The papers from the field of VF and microwave electronics, presented at this year's Conference, were chosen for this issue. These papers were written by the authors from the U.S.A., Japan, Germany, Republic of China, Republic of Srpska and Yugoslavia, with original scientific contributions, and 5 of them were invited papers. Most of the papers are improved versions of manuscripts presented at this year's Conference.

I would like to thank the authors of the papers who have accepted my choice of papers with pleasure, and prepared manuscripts for publishing in very short period of time. I hope that this issue of the journal Electronics will contribute to the further increase in the scientific reputation of Electronics and to the standing of the Faculty of Electrical Engineering in Banjaluka. Since I am certain that it will really happen, I will be happy if I contribute to it as a guest-editor.

B. D. Milovanović

LARGE SIGNAL CHARACTERIZATION OF HETEROJUNCTION BIPOLAR TRANSISTORS

Akhil Garlapati, Sheila Prasad
Northeastern University, Boston, USA.

Abstract - A large signal Ebers-Moll model for the analysis of an AlGaAs/GaAs Heterojunction Bipolar Transistor (HBT) is presented. The parasitic elements of the equivalent circuit are extracted from the s -parameter measurements under cutoff bias conditions. A semi-analytical approach is used to extract the intrinsic parameters of the small signal equivalent circuit. The equivalent circuit element parameters are evaluated from the frequency dependent scattering parameters measured under multiple bias. Only a few elements were evaluated from the numerical optimisation. Appropriate equations given by device physics are fitted to the bias variation of intrinsic parameters so that the large signal parameters can be extracted.

I. INTRODUCTION

Heterojunction bipolar transistors (HBT's) are presently used in many high frequency power applications because of their high cutoff frequency, current handling capability and breakdown voltage. Hence, a detailed analysis of HBT's has become important to further improve its design for optimum performance. For this purpose, many small signal and large signal models have been developed in the past. Several models, including the numerical model, the conventional Gummel-Poon model and the modified Ebers-Moll model have been presented by Teeter [1]. Several investigations of large signal HBT models are still being performed, since this model is essential for most practical applications [2, 3, 4].

This paper presents a simple Ebers-Moll model based on the quasi-static technique which makes use of multi-bias scattering parameters and DC measurements to extract a bias-dependent nonlinear equivalent circuit model. Section 2 presents the small signal equivalent circuit of an HBT and the method of extracting the small signal parameters.

The large signal Ebers-Moll model is presented in section 3, followed by the extraction of the model parameters using the DC measurements.

II. SMALL SIGNAL MODEL

The device under investigation is the AlGaAs/GaAs Heterojunction Bipolar Transistor. The small signal equivalent circuit of the device is shown in Fig. 1. Although there are many variations of the small signal equivalent circuit, the intrinsic part of the equivalent circuit is always the T or π topology. The T type intrinsic equivalent circuit is used in this work since it

is more physically meaningful than the circuit with the π topology. The different combinations of the lumped elements added to the intrinsic HBT circuit, as seen in Fig. 1, are used to more accurately characterize the frequency response of the HBTs.

Fig. 2 depicts the physical significance [5] of each of the circuit elements in Fig. 1. The active portion of the HBT is modeled using C_{be} , C_{bc} , r_e , α , R_{bc}

and C_f , where $\alpha = \frac{\alpha_F}{1 + jf/f_\alpha} e^{-j\omega\tau}$. α_F is the dc

value of the transport factor, τ is the collector current transit time and f_α is the α 3dB frequency. The contact resistance and emitter region resistance comprise R_E , the extrinsic emitter resistance. The

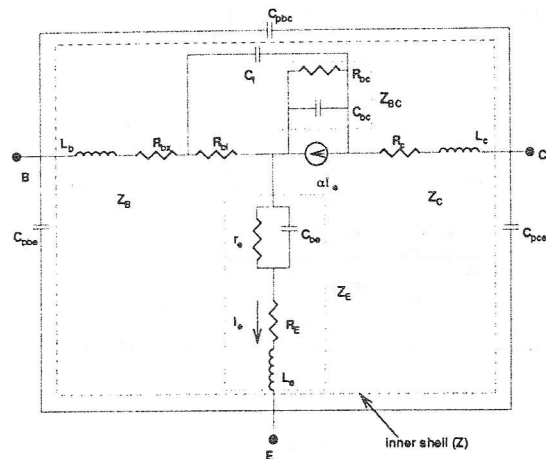


Figure 1: Equivalent circuit for the small signal model

extrinsic collector resistance is divided into three parts: R_{c1} , R_{c2} and R_{c3} respectively of the resistance due to the n-collector, the n+ access region and collector contact. The intrinsic collector resistance is represented by R_{ci} which characterizes the distributed effect of the base-collector junction at the collector side. Since it is difficult to distinguish between R_{ci} , R_{c1} , R_{c2} , R_{c3} and also, because the distributed effect at the collector side of the base-collector junction is not as significant as at the base side, all four elements are lumped together as R_c in Fig. 1.

Similarly, the extrinsic base resistance consists of a contact resistance, R_{b1} , and an access resistance, R_{b2} . R_{b1} and R_{b2} are lumped together as R_{bx} in Fig. 1. R_{bi} is the intrinsic base resistance. The distributed effect of the base-collector junction is

modeled by the elements $R_{bi}, R_{bx}, C_f, C_{bc}$ and $R_{bc} \cdot C_{pbe}, C_{pbc}, C_{pce}$ model the coupling between the base-emitter, the base-layer, L_e, L_b and L_c are the contact leads of the emitter, the base and the collector respectively.

All the above-mentioned parameters of the small-signal model are extracted using a partially analytical approach. RF-measurements indicate that the HBT under zero bias ($I_b = 0$ A, $V_{CE} = 0$ V) can be represented by a passive network. Therefore, in this case, the transport factor α is negligible. The parasitic elements, $C_{pbe}, C_{pbc}, C_{pce}$, are evaluated from the reverse bias scattering parameter measurements. These parasitics are deembedded from the circuit and the elements of the equivalent circuit, excluding the parasitic effects, are extracted from the resulting Z-parameters [6]. The extrinsic and intrinsic base resistances, and the base-collector capacitance are extracted by optimizing the error between the simulated and measured S-parameters.

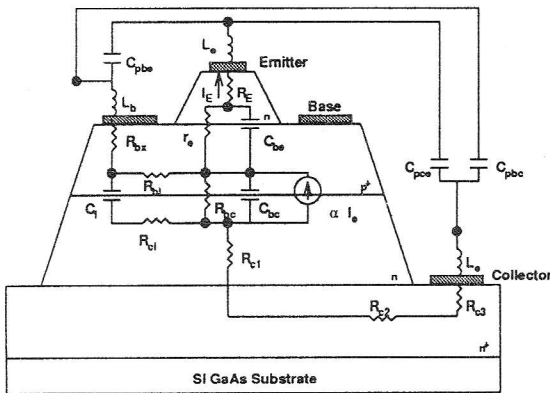


Figure 2: Physical significance of the small signal equivalent circuit elements

The elements R_b, L_e, R_e and R_c are basically constant over the entire frequency range of interest and do not show a significant variation with bias. Therefore, these elements can be considered to be fixed. The bias-dependent elements are $C_e, C_{jc}, R_{jc}, \alpha_F, \tau, f_\alpha$ and r_e . It has been shown that the consideration of the bias variation of these elements is sufficient for accurate small-signal modeling.

III. LARGE SIGNAL MODEL

A modified Ebers-Moll model is used to model the large signal behavior of the single-finger AlGaAs/GaAs HBT. The Ebers-Moll model is implemented in a commercial circuit simulator, LIBRA. The schematic of the modified Ebers-Moll

model [7, 8] for the HBT is shown in Fig. 3. Four diodes are used to model the non-linearity of the HBT. The variation of forward current gain with the collector current is modeled by the two diodes, D_{be} , and D_{se} . The diode, D_{be} represents the electron injection from the emitter and the diode, D_{se} , models the neutral base recombination, space charge region recombination, surface recombination and the other base leak currents. The two diodes, D_{bc} , and D_{sc} , model the dependence of the reverse current gain on the bias. The diode, D_{bc} , models the electron injection from the collector to base and the hole injection from the base to the collector. Diode, D_{sc} , models the neutral base recombination, space charge region recombination, surface recombination and the other base leakage currents resulting from the reverse operation. The distributed base-collector junction is modeled by the split base-collector capacitance. The transit time is easily included in the current gain of the Ebers-Moll model.

The effect of the collector transit time, τ , is included in the base-transport factor, α . However, the transit time is a function of the applied bias and it is difficult to implement the bias dependence of τ in the commercial circuit simulator LIBRA. Therefore, the value of the extracted τ at the bias point where the large signal analysis is carried out is used. Since the bias point is almost in the middle of the load line loci, the extracted value of τ at the bias point should be approximately the average value of τ from the dynamic load line loci. The error in the assumption does not significantly affect the present model as seen from a comparison of the simulated and measured DC characteristics.

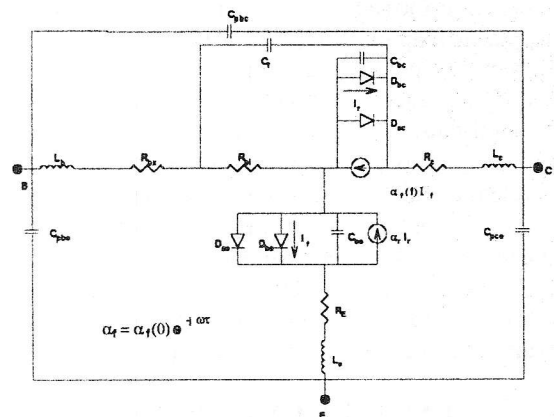


Figure 3: The schematic of the HBT's Ebers-Moll model

The Ebers-Moll model presented in this report is very similar in form to a previously published extensive large-signal model developed by Grossman and Choma [2]. However, when attempting to implement their model in SPICE, Grossman and Choma had not been able to include the transit time effect in their calculations because of the difficulties

involved in working exclusively in the time domain. This problem was circumvented with the Ebers-Moll model in this research by implementing the transit time delay in the frequency domain. Hence, the delay was simply represented as $e^{-jm\omega_0\tau}$ where m is the harmonic number and ω_0 is the fundamental frequency. The conduction current of the diodes and the displacement current of the nonlinear capacitors are implemented in the time domain whereas the injection current generators are implemented in the frequency domain. The two domains, time and frequency, are linked using the LIBRA harmonic balance software.

The base, collector and emitter DC currents used to describe the device, which comprise the Ebers-Moll model, are expressed as:

$$I_c = \alpha_f I_{be} \left[e^{\frac{qV'_{BE}}{n_f kT}} - 1 \right] - I_{bc} \left[e^{\frac{qV'_{BC}}{n_r kT}} - 1 \right] - I_{sc} \left[e^{\frac{qV'_{BC}}{n_{sc} kT}} - 1 \right] \quad (1)$$

$$I_b = I_{sc} \left[e^{\frac{qV'_{BC}}{n_{sc} kT}} - 1 \right] + I_{se} \left[e^{\frac{qV'_{BE}}{n_{se} kT}} - 1 \right] + (1 - \alpha_r) I_{sc} \left[e^{\frac{qV'_{BE}}{n_r kT}} - 1 \right] \quad (2)$$

$$I_e = I_{be}^M \left[e^{\frac{qV'_{BE}}{n_f kT}} - 1 \right] + I_{se} \left[e^{\frac{qV'_{BE}}{n_{se} kT}} - 1 \right] - \alpha_r I_{bc}^M \left[e^{\frac{qV'_{BC}}{n_r kT}} - 1 \right] \quad (3)$$

where V'_{BE} and V'_{BC} are the intrinsic base-emitter and base-collector junction voltages.

$$V'_{BE} = V_{BE} - I_e R_E - I_b R_b \quad (4)$$

$$V'_{BC} = V_{BC} - I_c R_c - I_b R_b \quad (5)$$

Large signal parameters are extracted by fitting these equations to the DC measurements. The forward Gummel-Poon plot at $V_{BC} = 0V$ is used to extract the current gain β_f , forward saturation current I_{be} , the base emitter leak saturation current I_{se} , the forward current ideality coefficient n_f , and the base emitter leakage emission coefficient n_{se} . Since the power dissipation at $V_{BC} = 0V$ is relatively small, the self-heating effect is negligible in the model parameter extraction procedure.

Simulated and measured scattering parameters are shown in Fig. 4,5,6,7. It can be seen that there is a good match between the simulation and measurements.

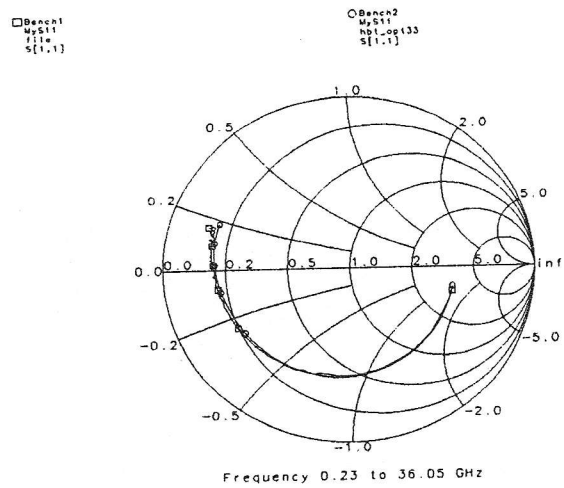


Figure 4: S11 - Simulated and measured

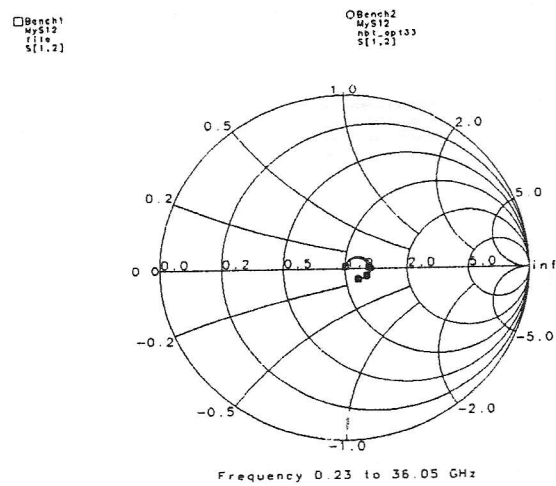


Figure 5: S12 - Simulated and measured

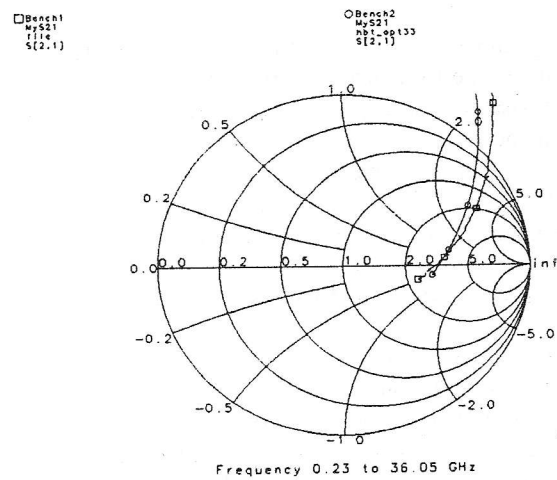


Figure 6: S21 - Simulated and measured

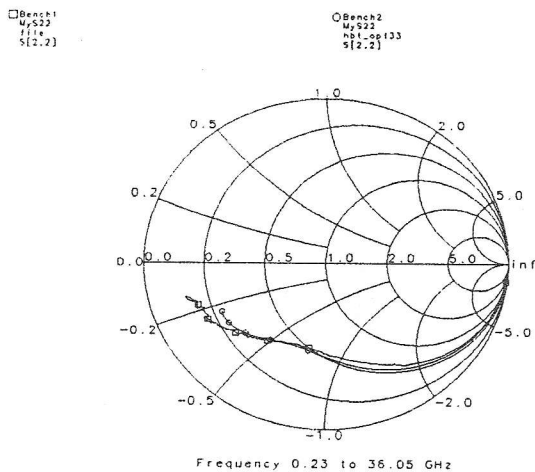


Figure 7: S22 - Simulated and measured

The simulated and the measured Gummel-Poon plot is shown in Fig. 8. It can be seen that there is a good match between the simulated and the measured characteristics. The values of the various parameters of the presented model are given in Table 1.

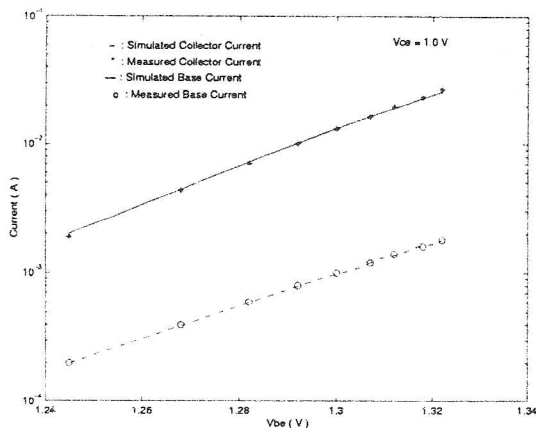


Figure 8: Simulated and measured Gummel-Poon plot

CONCLUSION

A simple Ebers-Moll model for predicting the nonlinear performance of a HBT has been presented. It is based on the experimental characterization of the frequency and bias-dependent behavior of the device small-signal parameters. The model parameters are deduced by fitting the bias-dependent intrinsic elements to the underlying equations from device physics.

ACKNOWLEDGEMENT

This research was supported in part by the National Science foundation under Grant ECS-9529643. The authors wish to thank Professor C. G. Fonstad of the Massachusetts Institute of Technology, Cambridge Massachusetts, USA for providing the laboratory facilities and Dr. L-W. Yang of TRW for providing the devices.

TABLE 1

Component	Value
L_b	48 pH
L_c	87 pH
L_e	20 pH
C_{pbe}	20 fF
C_{pce}	159 fF
C_{pbc}	0 fF
R_b	170 Ω
R_c	4 Ω
R_e	1 Ω
I_{be}	1e-24 A
n_{be}	1.07
M_{je}	0.6
V_{je0}	1.8 V
C_{je0}	1.2e-13 F
τ_F	0.1 ps
I_{sc}	4.5e-16 A
n_{bc}	2.84
M_{jc}	0.56
V_{jc0}	1.17 V
C_{jc0}	7.8e-14 F
α_F	0.94
f_α	29 GHz
τ	6 ps
α_R	2.25e-11

BIBLIOGRAPHY

- [1] D. A. Teeter, J. R. East, R. K. Mains, and G. I. Haddad, "Large-signal numerical and analytical HBT models," *IEEE Trans. Electron Devices*, vol. ED-40, no. 5, pp. 837-845, 1993.
- [2] P. C. Grossman, and J. Choma, "Large signal modeling of HBT's including self-heating and transit time effects," *IEEE Trans. Microwave Theory Tech.*, vol. MTT-40, no. 3, pp. 449-464, 1992.
- [3] M. Y. Frankel and D. Pavlidis, "An analysis of the large-signal characteristic of AlGaAs/GaAs heterojunction bipolar transistors," *IEEE Trans. Microwave Theory Tech.*, vol. MTT-40, no. 3, pp. 465-474, 1992.
- [4] K. Wu and P. A. Perry, "A new large-signal AlGaAs/GaAs HBT model including self-heating effects, with corresponding parameter-extraction procedure," *IEEE Trans. Microwave Theory Tech.*, vol. MTT-43, no. 17, pp. 1433-1445, 1995.
- [5] H. Kroemer, "Heterojunction bipolar transistors and integrated circuits," *Proc. IEEE*, vol. 70, pp. 13-25, 1982.
- [6] D. R. Pehlke and D. Pavlidis, "Evaluation of the factors determining HBT high frequency performance by direct analysis of s-parameter

- data," *IEEE Trans. Microwave Theory and Tech.*, vol. MTT-40, no. 12, pp. 2367-2373, 1992.
- [7] P. M. Asbeck, M. F. Chang, J. A. Higgins, N. H. Sheng, G. J. Sullivan and K. C. Wang, "GaAlAs/GaAs heterojunction bipolar transistors: issues and prospects for application," *IEEE Trans. Electron Devices*, vol. ED-36, pp. 2032-2042, 1989.
- [8] M. E. Kim, A. K. Oki, G. M. Gorman, D. K. Umemoto and J. B. Camou, "GaAs heterojunction bipolar transistor device and IC technology for high performance analog and microwave applications," *IEEE Trans. Microwave Theory Tech.*, vol. MTT- 37, pp. 1286-1303, 1989.

MEMS TECHNOLOGIES FOR ENABLING HIGH FREQUENCY COMMUNICATIONS CIRCUITS

Victor M. Lubecke¹ and Jung-Chin Chiao²

¹ Bell Laboratories, Lucent Technologies, Murray Hill, USA

² University of Hawaii – Manoa, USA

Abstract – Wireless systems requirements to increased data capacity and decreased size and power consumption have pushed radio frequency integrated circuit (RFIC) technology to extremes. Microelectromechanical systems (MEMS) techniques have been used to demonstrate high-efficiency microwave components that provide a means for economically extending silicon RFIC technology to microwave frequencies to meet these demands. MEMS techniques are also being applied to create cost-effective integrated circuits that can function efficiently at millimeter wavelengths and beyond, to further exploit the advantages of increased bandwidth, reduced size, and unique propagation characteristics available at these higher frequencies. An overview is presented here, of recently demonstrated high-frequency MEMS components and techniques that can enhance existing microwave communications circuits and enable economical millimeter wave communications.

I. INTRODUCTION

The growing importance of the mobile telecommunications market has created a strong interest in circuits and systems with minimal size, cost, and power consumption, which can also handle high data rates. The limits of silicon RF integrated circuit (RFIC) technology are being steadily challenged, and UHF spectral allocations are being fully exploited to meet these demands. The innovative use of microelectromechanical systems (MEMS) technology offers a means for further extending the limits of conventional silicon IC technology at microwave frequencies, and for providing an economical means of accessing the benefits of reduced size and increased bandwidth that are available at even higher frequencies. Conventional RFIC's are designed to exploit the capabilities of CMOS and Bipolar devices. The technology is mature, and a large investment has been made by governments and industry to establish an infrastructure for this technology. However, when operating at frequencies above 2 GHz, parasitic effects in these circuits result in a significant degradation of performance. Electronic

junctions cease to act as effective switches, and substrate coupling limits the quality factor (Q) that can be achieved for resonator and impedance matching elements [1-3]. At higher frequencies, alternative circuit technology is utilized to take advantage of higher speed semiconductor, superconductor, and other thin film devices. These devices are typically implemented in waveguide circuits, or on high resistivity dielectric substrates. Getting optimal performance from these circuits typically involves painstaking assembly and fine-tuning. Without the benefit of a broad commercial infrastructure, these technologies are quite costly, and usually limit applications to scientific research [4].

A broad range of MEMS components has been recently demonstrated, with function and efficiencies that are significantly improved over conventional RFIC technology. These include microswitches, inductors, and varactors with reduced parasitics and improved linearity and dynamic range. Additionally, MEMS technology promises to make millimeter-wave and higher frequencies accessible to commercial telecommunications, in an economical form. High aspect-ratio UV-lithography techniques allow inexpensive plastic waveguide components to be batch fabricated, and MEMS actuators provide a means for tuning the performance of high frequency integrated circuits, in order to optimize impedance matching for cutting edge devices and to tailor antenna patterns to specific applications. An overview of these components and technologies is presented here.

II. MICROWAVE RFIC COMPONENTS

A. MEMS RF Microswitches

Perhaps the most prolific MEMS RF component is the microswitch. In essence, it is a miniaturized version of a mechanical toggle switch, realized through batch IC processes. It offers good insertion loss, fast switching speeds, low power dissipation, and excellent linearity at frequencies where switching with nonlinear devices can be significantly degraded.

Promising realizations of this switch have been demonstrated as cantilevers and membranes that deform when subjected to electrostatic actuation forces. In cantilever switches, one metallic switch-electrode is suspended on a dielectric cantilever or spring, and a voltage is applied between a metal pad on the dielectric and the other metal switch-electrode on the substrate below [3][5]. Insertion loss is largely determined by the metal-to-metal contact of the electrodes during activation, and isolation is dependent on the vertical displacement between the electrodes when not activated. In membrane switches, a thin-film metal air bridge is suspended across a dielectric-coated coplanar transmission line, and an actuation voltage applied between the bridge and the line beneath it to collapse the bridge and capacitively load the transmission line [3][6]. In this case insertion loss and isolation are dependent on the difference in capacitance seen by the line during the on and off states.

In the case of both switch types, it is desirable to have a large displacement between conductors during the off state, and close contact in the on state. Function and reliability of the switches depend on metal or dielectric stress control, electrode stiction, and the durability of the bending components.

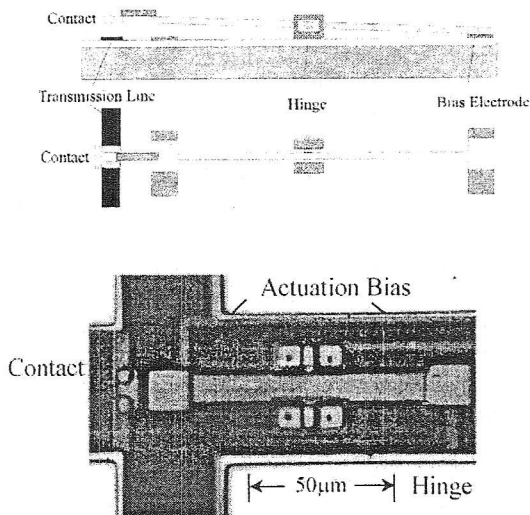


Fig. 1. Concept and microscope photograph of a see-saw-bar switch. The switch has a metal pad on one end of a rocking arm that can bridge the contacts on the substrate when the proper bias is applied.

A see-saw-bar switch, designed to avoid the drawbacks of bending thin-film components, is

shown in Fig. 1 [7]. A see-saw bar, with bias electrodes on both ends, is held by hinges on the sides of the bar. One end of the bar is attached to a metal contact pad that is used to make a connection between the contacts on the substrate. With bias voltages on different bias electrodes, the metal contact can be pulled up or pushed down to open or close the connection. The rigid polysilicon bar helps prevent stiction and degradation associated with the thin-film cantilevers and membranes. A 4- μm air-gap was achieved with an actuation voltage of 20v. The DC series resistance is negligible and RF performance is currently under investigation.

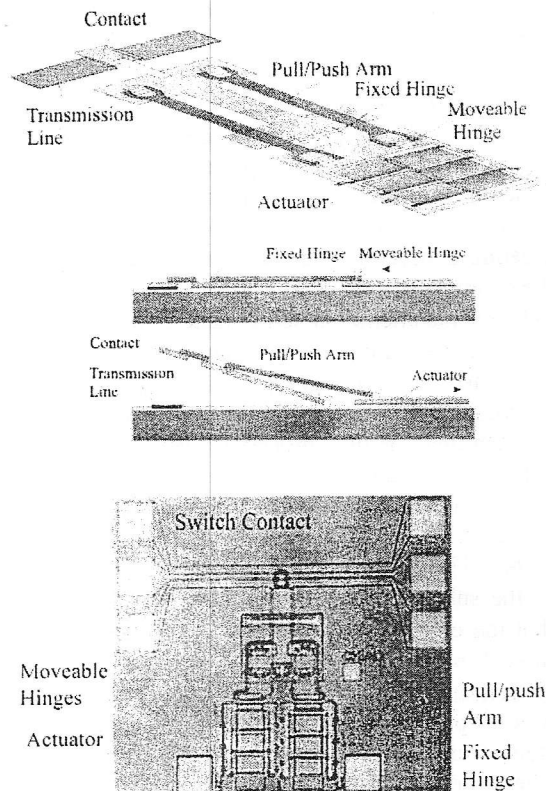


Fig. 2. Concept and microscope photograph of a derrick-type switch. Scratch-drive microactuators are used to pull one hinged electrode over the other, and thus allow for a large "off" displacement as well as excellent isolation between actuation and RF signals.

A derrick-type switch, designed to offer high isolation and low insertion loss, is shown in Fig. 2 [7]. In this design, scratch-drive microactuators [8] are used to pull one hinged electrode over the other, and thus allow for a large "off" displacement, as well as excellent isolation between actuation and RF signals. The microactuators pull away, or push forward, the pull/push arms that connect to the

sides of the support bar through moveable hinges. With one end of the support bar held by fixed hinges on the substrate, the moveable hinges on both ends of the pull/push arms translate the lateral movement of the actuators in to a vertical movement of the support bar. A metal contact pad, attached in the end of the support bar, is pulled up to open or pushed down to close the signal path through the transmission line. In this design, the air gap between the metal contact and the transmission line can be as high as $100\mu\text{m}$. The measured switching time for a $100\text{-}\mu\text{m}$ gap is $150\mu\text{s}$. The strong actuation force of scratch drive actuators provides firm contact between the metal pads. The RF performance and reduction of switching time is currently under study.

B. MEMS RF inductors

Innovative MEMS techniques are also providing a means of reducing the parasitic losses which generally impede the performance of conventional on-chip inductors. This is typically achieved by creating a structure that isolates the inductor from the conductive substrate.

While some attempt is being made to incrementally improve the isolation between the inductor and substrate by achieving increased dielectric thickness and enhanced ground planes within conventional RFIC processes [9], post-process MEMS techniques can extend this improvement. Designs have been demonstrated with the turns of the inductor elevated by a dielectric mesa [10] or stilts [11], and by winding the turns perpendicular to the substrate plane [12]. These designs require that the circuit fabrication process accommodate a three dimensional structure.

A self-assembled inductor, designed as a pre-process planar structure that is released as the final step of circuit fabrication, is shown in Fig.3 [13]. The residual tensile stress between a polysilicon layer and a Cr-Au metal layer is used to achieve a significant warpage of the inductor structure. While normally undesirable, here the warpage provides an automatic means of raising the inductor above the substrate to reduce parasitic effects.

Quality factors up to 14 have been demonstrated for one-turn inductors in the $1\text{-}3\text{nH}$ range, and analysis indicates that with sufficient metal and separation this technique could be used to reach Q's above 25. The technique can also be applied to multi-turn structures for increased inductance. The process is highly repeatable, with 5 copies from different fabrication runs shown to have a variation in inductance of only 1-2%.

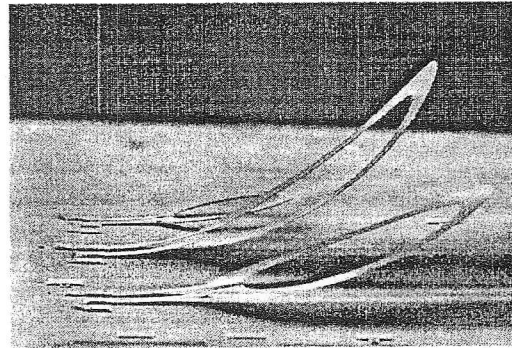
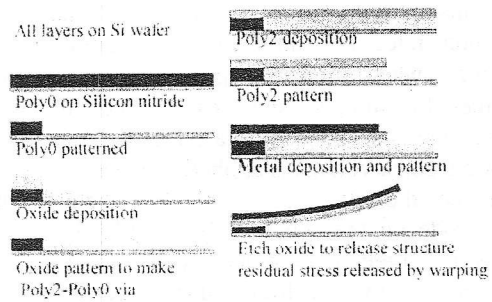


Fig. 3. Fabrication and realization of self assembled RF MEMS inductors. When released, tensile stress between the polysilicon and metal layers causes the inductors to warp away from the substrate, reducing the stray fields in the silicon substrate.

C. MEMS RF Varactors

As in the case of switches, MEMS RF varactors offer high efficiency and linear control, at frequencies where semiconductor devices show significantly degraded performance. In general, these components consist of traditional capacitor geometries like parallel plates and interdigitated elements, but with the addition of a mechanism by which the displacement of the plates or elements can be micromechanically altered to vary the capacitance.

Designs have been demonstrated where electrostatic forces between elements are used to pull one closer to the other [3][14]. In the case of parallel plates, the component works similarly to the metal-membrane air bridge switch described earlier, but with altered spring tension that emphasizes a more gradual transition rather than a collapse. A similar bending effect can be achieved electro-thermally [15]. Such designs must contend with limited tuning range and microphonics.

A MEMS parallel parallel-plate varactor designed to maximize tuning range and minimize microphonic effect is shown in Fig.4 [7]. Microactuators are used to pull or push support arms, which control the height of one parallel

positioned above another. The microhinges on either end of the support arms translate the lateral movement of the microactuators to a vertical motion that varies the gap spacing between the two metal plates. With the actuators on both sides moving toward the plate at the same time pushing the support arms up, the gap spacing is increased. With the actuators moving away from the plate, the gap spacing is reduced. The variable capacitance should follow the formula, $C(x) = \epsilon_0 A/x + C_p$, where A is the plate size, x is the gap spacing, ϵ_0 is the dielectric constant of air and C_p is the parasitic capacitance. The actuators can be programmed so that not only the height of the gap is variable, but the coupling area (A) between two metal plates can also be varied for a linear operation of the variable capacitance.

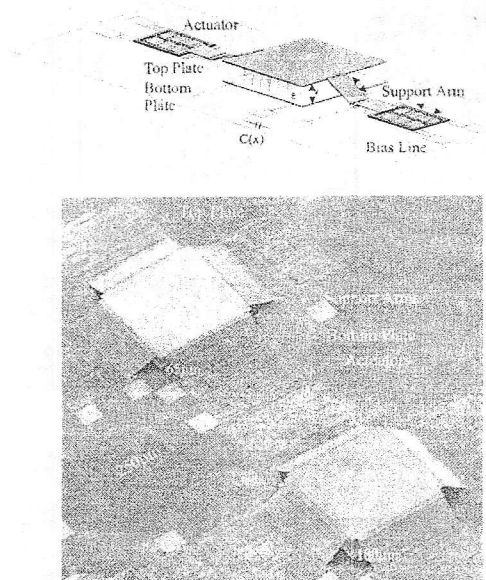


Fig. 4. Architecture and realization of a MEMS parallel-plate variable capacitors. Hinged control arms are used to convert the linear translation of scratch drive actuators into vertical motion for the capacitors upper plate.

Several parallel-plate capacitors, with plate sizes in the ranges from $100\mu\text{m} \times 100\mu\text{m}$ to $2\text{mm} \times 2\text{mm}$, were designed and fabricated, all similar to the one shown in Fig.4. The gap spacing could be varied between $1\mu\text{m}$ and $100\mu\text{m}$, with an increment of 20nm , giving a dynamic range of 1:100. Preliminary results showed a maximum capacitance of 35pF and a minimum capacitance of 0.5pF for a $2\text{mm} \times 2\text{mm}$ capacitor measured using a low-frequency capacitance meter. The breakdown voltages of the MEMS variable capacitors should be much higher than those of diode varactors. The

measured breakdown voltage of the MEMS capacitor is more than 200V , where the measurement was limited by the availability of high-voltage sources.

Another architecture for MEMS parallel-plate capacitors is also under investigation. In some applications, variable capacitors are not required to have a large dynamic range, but a linear operation and compact configuration is desired. Fig.5 shows a circular parallel-plate variable capacitor. The coupling area between top and bottom plates can be varied using the microactuators to rotate the upper plate.

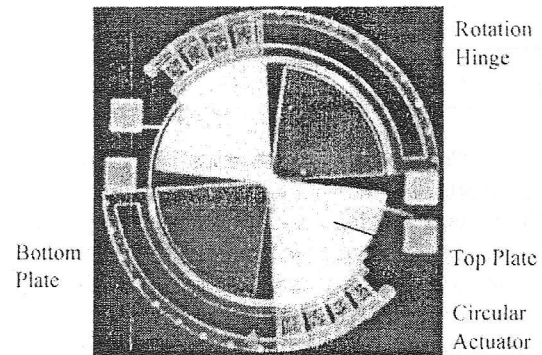
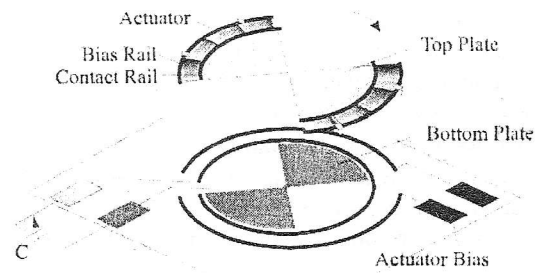


Fig. 5. The concept and a microscope photo of a circular parallel-plate variable capacitor. Microactuators are used to rotate the upper plate to increase or decrease its overlap with the lower plate, thus varying the capacitance.

III. HIGH FREQUENCY WAVEGUIDE COMPONENTS

A. Non-contacting Backshorts

A backshort is a conductive plunger that can be inserted in one end of a waveguide to create a termination or short circuit for radio signals that enter the other end. Adjusting the depth to which the backshort is inserted effectively varies the electrical length of the guide. The use of such variable length tuning stubs is a common means for optimizing the impedance match between a

waveguide/antenna system and an embedded device. At lower frequencies a backshort with a metallic-spring tip can be used to create a physical short circuit with the guide walls. At short millimeter wavelengths and beyond however, it is difficult to realize an effective and repeatable physically contacting short circuit, and so non-contacting designs are more appealing.

Non-contacting backshorts are conductive plungers with a shape which alternately fills and empties a waveguide at intervals of one-quarter wavelength, creating a hi/low impedance cascade which results in a very low impedance termination around the backshorts design frequency [16]. This principle is illustrated in Fig.6. Such backshorts offer repeatable performance without relying on physical contact, and offer the additional benefit of a low-pass condition to support IF signals in the same guide. These components have intricate three-dimensional shapes and at submillimeter wavelengths the feature dimensions can be on the order of microns, which makes fabrication through conventional milling or etching impractical.

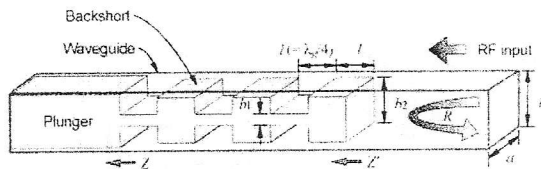


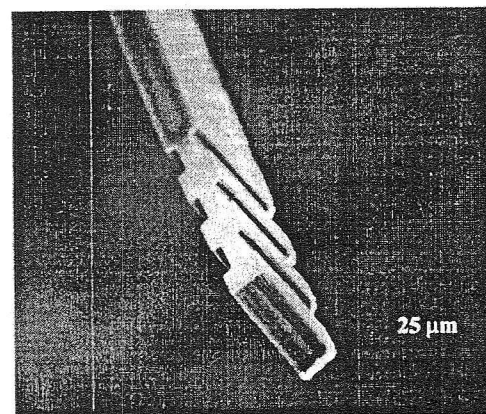
Fig. 6. Conceptual illustration of a non-contacting backshorts in a rectangular (axb) metal waveguide. The varying height of the backshort (b_1 , b_2) causes a cascade of alternately low and high impedance quarter-wavelength waveguide sections, which presents as a very low impedance movable termination to the guide, at the resonant frequency.

Non-contacting backshorts designed for use at 240 GHz, 640 GHz, and 2.5 THz have been realized through micromachining techniques based on the use of ultra-thick UV-sensitive resin [17]. The resin is used as a negative photoresist that is spin-deposited on a sacrificial substrate and exposed to UV light through a shadow mask. The exposed resin is cured by the exposure, allowing the rest of the resin to be dissolved and flushed with solvent. What remain are high aspect-ratio backshort structures with varied and precise feature shapes in the horizontal plane. The processed substrate is then wax-bonded to a superstrate, which allows for the mechanical removal of the substrate and precise reduction of the structure height (waveguide width) using a dicing saw. The backshorts are then metalized through RF sputter-coating, rinsed from

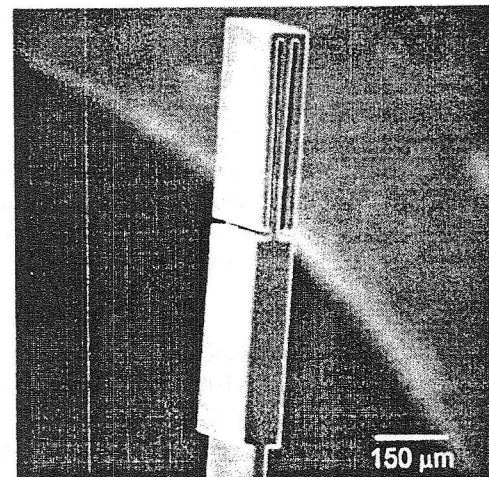
the superstrate with solvent and recovered with filter paper. This process allows hundreds of backshorts to be processed simultaneously in a single batch.

A backshort designed for use at 2.5 THz is shown in Fig.7(a). The tip has a cross-section of approximately $25\text{-}\mu\text{m}$ by $90\text{-}\mu\text{m}$. The backshort shown in Fig.7(b), designed for a mixer which operates at 240 GHz, uses a more compact non-contacting design.

This resin technique can also be combined with silicon micromachining to create complex mechanical forms. An entire mixer block assembly has been proposed, which includes a silicon horn antenna integrated with various waveguide channels for signal routing and tuning [4][18].



(a)



(b)

Fig. 7. Non-contacting waveguide backshorts fabricated using high aspect ratio photo-plastic techniques. A metalized backshort designed for 2.5 THz is shown above (a) and a more compact design for 240 GHz is shown below (b).

B. Dichroic Plates

Perforated metal plates provide an excellent means for producing quasi-optical high-pass filters at high frequencies [19]. The perforations in such dichroic plates serve as waveguides that can support the propagation of signals above a certain cutoff frequency, and signals below this frequency are largely reflected. The attenuation of the cut-off signal is dependent on the plate thickness. The concept for a dichroic plate is illustrated in Fig. 8.

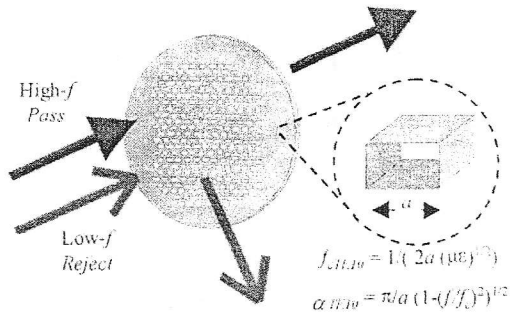


Fig. 8. Conceptual illustration for a frequency selective mirror called a dichroic plate. The perforations in the metallic plate serve as an array of waveguides that can support the propagation of signals above a certain cutoff frequency, with signals below this frequency largely reflected.

At longer millimeter wavelengths, such holes can be conventionally machined, particularly if they are limited to circular shaped apertures. At shorter wavelengths, the dimensions needed for these holes becomes too difficult to realize through conventional machining, and typical planar fabrication processes are not suited to producing structures which are thick enough to serve as waveguides. However, micromachining with thick photo-plastic can be used to produce relatively thick structures, with complex, high-resolution perforations.

A dichroic plate designed to pass 640 GHz signals is shown in Fig. 9 [17]. This particular design depends on a large array of cross-shaped apertures with dimensions on the order of 100 μm , which are too small for conventional milling, and vertical sidewalls on the order of 500 μm , which cannot be achieved through isotropic etching techniques. The entire plate is about 4 cm in diameter, and was realized using only photo-plastic techniques and metal sputter coating. A dichroic plate for 1.0 THz was also fabricated with this technique. At these higher frequencies, useful plates can be made small enough to allow simultaneous batch fabrication of multiple copies.

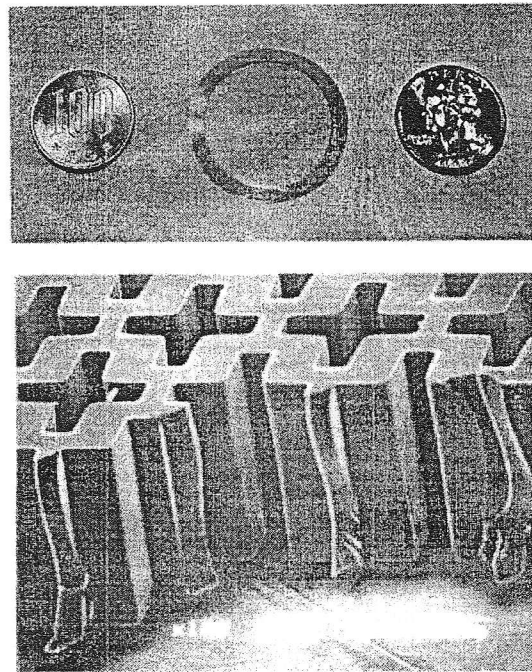


Fig. 9. Dichroic plate for 640 GHz fabricated from ultra-thick epoxy-based photoresist. The 4-cm diameter of the structure is relatively large, yet it contains high-resolution complex apertures on the order of 100 μm , with vertical walls throughout the 500 μm thickness.

IV. HIGH FREQUENCY IC COMPONENTS

A. Reconfigurable Antenna

The use of silicon micromachining to realize very small three dimensional antenna structures for high frequencies was explored as early as 1979 [4][20]. In this case, a tapered dielectric rod was formed, with an integrated membrane supported sensor. Subsequently, other fixed antennas have been realized, featuring more intricate structures [4][21]. A novel millimeter wave "V" (vee) antenna, which uses MEMS techniques both for its fabrication and for re-configuration, is shown in Fig. 10 [9]. The arms of the V-shaped antenna are moveable through pulling or pushing by microactuators. Each antenna arm can be controlled independently with forward- or backward-moving biases. When both antenna arms move in the same direction with a fixed V-angle, the antenna can be used to steer the radiation beam. When the V-angle changes, the radiation beam shape can be adjusted. The reconfigurability and antenna performance have been demonstrated. Beam-steering at 30 and 45 degrees, and beam-shaping for V-angles of 75, 90 and 120 degrees have been demonstrated for a 17.5-GHz MEMS V-antenna.

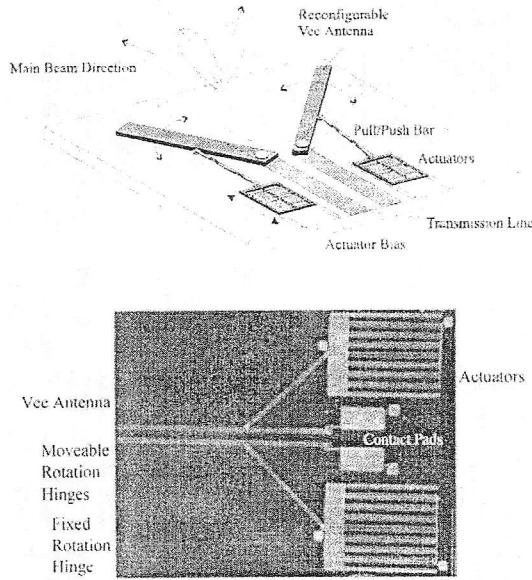


Fig. 10. Concept and realization of a MEMS reconfigurable V-antenna can be rotated using microactuators, to either steer or reshape the antenna beam.

B. Planar Impedance Tuner

A planar version of the non-contacting backshort has also been developed. It is called a sliding planar backshort (SPB). As in the waveguide version, the SPB creates an effective termination or RF short circuit by causing a periodic (quarter-wavelength) version in the impedance of a transmission line. In this case the structure is a metal plate with strategically placed holes, which alternately covers and uncovers a dielectric-coated coplanar transmission line.

A fabrication technique was developed for realizing the SPB with materials and processes common to submillimeter wave circuits, and two SPB tuners were fully demonstrated in a 620 GHz quasi-optical detector circuit [4][22]. The circuit was fabricated on a quartz wafer which fits over a dielectric-filled parabola substrate lens, and is shown in Fig.11(a). An electromechanical version of the SPB structure has also been demonstrated, and can potentially be implemented in a millimeter wave or higher frequency circuits [7]. Various SPB tuners on coplanar transmission lines, like that shown in Fig.11(b), have been designed and fabricated to investigate the tuning characteristics and integration aspects of SPB tuners with microactuators. One application of electromechanical SPB tuners is the impedance matching of MEMS reconfigurable V-antennas to optimize performance for every possible configuration. The concept for a fully

reconfigurable MEMS transceiver that utilizes these devices is shown in Fig.12.

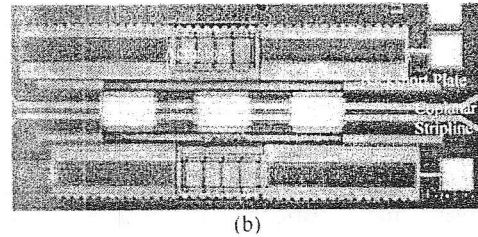
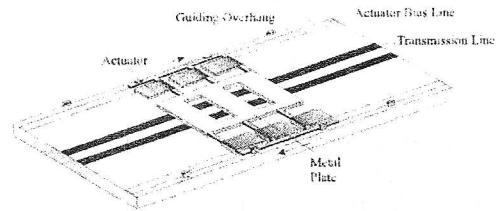
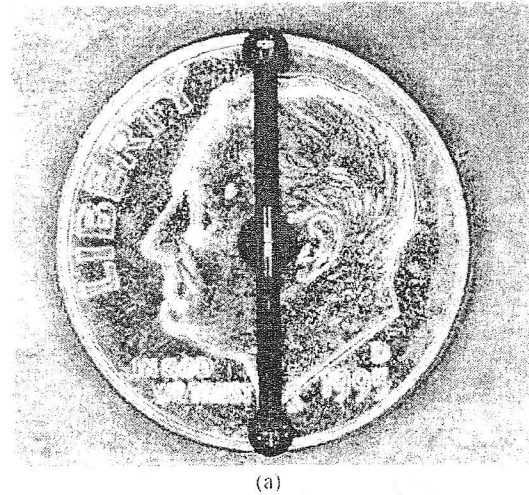


Fig. 11. MEMS tunable 620 GHz quasi-optical integrated circuit (a), and an electromechanical implementation of the tuners (b). Microactuators can be used to add precision interactive control of the tuners in this circuit.

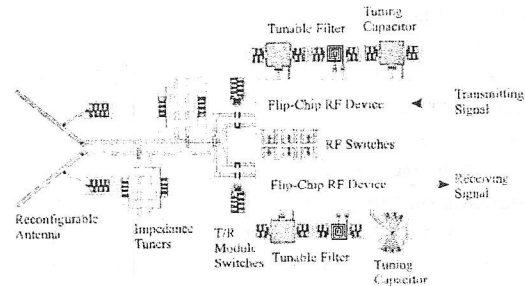


Fig. 12. Architecture of a MEMS reconfigurable transceiver. Microactuators are used to steer and shape the antenna beam, and to retune the circuit for optimal performance.

V. CONCLUSIONS

A variety of components and techniques which can be used to enhance the performance of conventional RFIC's at microwave frequencies, or to make practical the realization of millimeter-wave and higher frequency communications circuits, have been presented here. These include microwave switches, inductors, and varactors with low loss and high linearity, as well as economical realizations of higher frequency waveguide components and reconfigurable IC's. These components and techniques offer great promise for further reductions in size and power consumption of high data-rate personal communications devices and systems.

VI. ACKNOWLEDGMENT

The authors wish to acknowledge the support of Lucent Technologies, the Institute for Physical and Chemical Research (RIKEN, Japan), the NASA Jet Propulsion Laboratory, the University of Hawaii at Manoa, HRL Laboratories, and the US Army Research Office.

VII. REFERENCES

- [1] C. P. Tue, and S. S. Wong, "A Study on Substrate Effects of Silicon-Based RF Passive Components", *IEEE MTT-S Int. Microwave Sym. Dig.*, pp. 607-610, June 1987.
- [2] C. Y. Chi, and G. M. Rebeiz, "Planar microwave and millimeter-wave lumped elements and coupled-line filters using micromachining techniques", *IEEE Trans. Microwave Theory Tech.*, vol. MTT-43, pp. 730-738, April 1995.
- [3] E. R. Brown, "RF-MEMS Switches for Reconfigurable Integrated Circuits", *IEEE Trans. Microwave Theory Tech.*, vol. MTT-46, No. 11, pp. 1868-1880, November 1998.
- [4] V. M. Lubecke, K. Mizuno, G. M. Rebeiz, "Micromachining for Terahertz Applications", *IEEE Trans. Microwave Theory Tech.*, vol. MTT-46, No. 11, pp. 1821-1831, November 1998.
- [5] J. J. Yao, and M. F. Chang, "A surface micromachined miniature switch for telecommunication applications with signal frequencies from DC up to 4 GHz", in *Transducers '95*, pp. 384-387, June 1995.
- [6] C. L. Goldsmith, Z. Yao, S. Eshelman, and D. Denniston, "Performance of Low Loss RF MEMS Capacitive switches", *IEEE Microwave and Guided Wave Letters*, Vol. 8 No. 8, August 1998
- [7] J.-C. Chiao, Y. Fu, D. C. Choudhury, and L.-Y. Lin, "MEMS Millimeterwave Components", *IEEE MTT-S Int. Microwave Sym. Dig.*, pp. 463-466, June 1999.
- [8] T. Akiyama and K. Shono, "Controlled Stepwise Motion in Polysilicon Microstructures", *IEEE/ASME Journal of Microelectromechanical Systems*, vol. 2, no. 3, pp. 106-110, September 1993.
- [9] C. P. Yue and S. S. Wong, "On-chip spiral inductors with patterned ground shields for Si-Based RF IC's", *1997 Symposium on VLSI Circuits Digest of Technical Papers*, pp. 85-86, 1996
- [10] K. Kemogawa, K. Nishikawa, T. Tokumitsu, and M. Tanaka, "A Novel High-Q Inductor Based on Si 3D MMIC Technology and its Application", *IEEE MTT-S Int. Sym. Dig.*, pp. 489-492, June 1999.
- [11] J.-B. Yoon, C.-H. Han, E. Yoon, and C.-K. Kim, "High-Performance Three-Dimensional On-Chip Inductors Fabricated by Novel Micromachining Technology for RF MMIC", *IEEE MTT-S Int. Microwave Sym. Dig.*, pp. 1523-1526, June 1999.
- [12] D. J. Young and B. E. Boser, "A micromachined variable capacitor for monolithic low-noise VCO's", *Technical Digest, 1996 Solid-State Sensor and Actuator Workshop*, Hilton Head Island, South Carolina, June 3-6, 1996, pp. 86-89.
- [13] P. L. Gammel, B. P. Barber, V. M. Lubecke, N. Belk, and M. Frei, "Design, Test, and Simulation of Self-Assembled, Micromachined RF Inductors", *SPIE Symposium on Design, Test, and Microfabrication of MEMS and MOEMS Digest*, Paris, France, pp. 582-601, March-April 1999.
- [14] D. J. Young, V. Malba, J.-J. Ou, A. F. Bernhardt, and B. E. Boser, "Monolithic high-performance three-dimensional coil inductors for wireless communication applications", *Technical Digest, IEEE International Electron Devices Meeting*, Washington, D. C., Dec. 8-11, 1997, pp. 67-70.
- [15] Z. Feng, W. Zhang, B. Su, K. F. Harsh, C. Gupta, V. B. right, and Y. C. Lee, "Design and Modeling of RF MEMS Tunable Capacitors Using Electro-thermal Actuators", *IEEE MTT-S Int. Microwave Sym. Dig.*, pp. 1507-1510, June 1999.
- [16] R. E. Collin, *Foundations for Microwave Engineering*. New York: McGraw-Hill, 1996. lins

- [17] V. M. Lubecke, T. Hamano, C. M. Mann, and K. Mizuno, "Micromachining of photo-plastic submillimeter wave components", in *Proc Asia-Pacific Microwave Conf.*, Yokohama, Japan, Dec. 1998.
- [18] T. W. Crowe, P. J. Koh, W. L. Bishop, C. M. Mann, et al., "Inexpensive Receiver Components for Millimeter Wavelengths", *Eighth International Symposium on Space Terahertz Technology*, pp. 377-384, March 1997.
- [19] P. F. Goldsmith, *Quasioptical Systems*. New York: IEEE Pres., 1998.
- [20] D. B. Rutledge, S. E. Schwarz, T. L. Hwang, D. J. Angelakos, K. K. Mei, and S. Yokota, "Antennas and Waveguides for Far-Infrared Integrated Circuits", *IEEE Journal of Quantum Electronics*, vol. 16, pp. 508-516, May 1980.
- [21] G. M. Rebeiz, D. P. Kasilingam, Y. Guo, P. A. Stimpson, and D. B. Rutledge, "Monolithic millimeter-wave two-dimensional horn imaging arrays", *IEEE Trans. Antennas Propagat.*, vol. AP-38, pp. 1473-1482, September 1990.
- [22] J.-C. Chiao, Y. Fu, I. M. Chio, M. DeLisio, and L.-Y. Lin, "MEMS Reconfigurable Vee Antenna", *IEEE MTT-S Int. Microwave Sym. Dig.*, pp. 1515-1518, June 1999.
- [23] V. M. Lubecke, W. R. McGrath, P. A. Stimpson, and D. B. Rutledge, "Micromechanical tuning elements in a 620 GHz integrated circuit", *IEEE Trans. Microwave Theory Tech.*, vol. MTT-46, No. 12 pp. 2098-2103, December 1998.

APPROXIMATION OF GaAs FET TWO-PORT NETWORK Z-PARAMETERS BY RATIONAL FUNCTIONS

Vidosav S. Stojanović, Saša S. Radovanović
University of Niš, Faculty of Electronic Engineering, Yugoslavia

Abstract—In this paper, a least squares approximation procedure for the measured values of transistor Z parameters by rational functions is described. The orders of polynomials in the denominator and numerator are determined by equivalent circuit or obtained empirically. Some rational functions of Z parameters have one zero and pole which could be canceled so the functions having lower order of polynomial in the denominator and numerator are obtained. All Z parameters have one common pole. This procedure does not include computation of derivatives. The computation of the polynomials in the numerator and denominator of rational function is fully described on the high frequency GaAs FET.

I. INTRODUCTION

Accurate two-port network parameter approximation is an essential tool for reliable nonlinear device modeling and electronic circuit design. In the last two decades numerous methods have been proposed for the approximation of two-port network parameters.

The equivalent circuit approach has been commonly used to characterize active devices. In those models, however, the value of each equivalent circuit element has to be determined by the time consuming iteration or by some additional measurement. In a great number of applications there is no need for the equivalent circuit, but for the rational function. For example, in the software for symbolic analysis of electronic circuits. A characterization of GaAs MESFET using least squares approximation for the measured values of S parameters by rational function are presented in paper [1] and [2]. This approximation technique was developed for small-signal equivalent circuit element extraction. The rational functions in explicit form are not given. In paper [2], explicit relations between GaAs MESFET equivalent circuit elements and coefficients of two-port impedance parameters are presented. However, there was no explanation of how the coefficients in the denominator

polynomials were obtained.

The main aim of this paper is to approximate two-port network Z parameters of GaAs FET using least squares method by the set of rational functions. The set is closely correlated with the equivalent circuit. All Z parameters have one common pole in the denominator. Some of the Z parameters have one zero and a pole which could be canceled so the rational functions having lower order of polynomials in the denominator and the numerator are obtained. The poles of rational functions are away from each other and all polynomials in the denominator have the same first coefficient. This procedure does not include computation of derivatives. The set of rational function approximates measured values of Z parameters with well accuracy.

The approximation procedure is fully described on $400\mu\text{m}$ GaAs MESFET.

We will consider high frequency transistor as a two-port network, generally shown on figure 1.

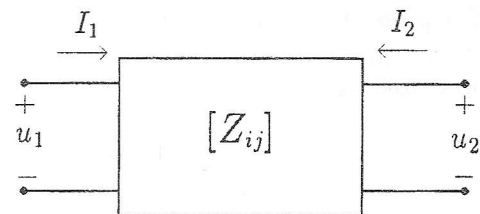


Figure 1. A general two-port network with Z parameters

II. RATIONAL FUNCTIONS

Let n be a number of the complex measured values for each of two-port network impedance parameters on frequencies ω_k , $k = 1, 2, \dots, n$.

$$\hat{Z}_{ij}(\omega_k) = \hat{R}_{ij}(\omega_k) + j\hat{X}_{ij}(\omega_k) \quad (1)$$

$i, j = 1, 2$

where \hat{R}_{ij} and \hat{X}_{ij} denotes the real and imaginary part of the measured values of Z -parameters, respectively.

According to the standard small-signal equivalent circuit, we determine the orders of

polynomials in the numerator and denominator of rational functions.

The measured values of Z parameters (1) are approximated by rational functions in the form of

$$\begin{aligned} Z_{11}(s) &= \frac{A_0^{11} + A_1^{11}s + \dots + A_{N_{11}}^{11}s^{N_{11}}}{s + \frac{s^2}{p_1}} \\ Z_{12}(s) &= \frac{A_0^{12} + A_1^{12}s + \dots + A_{N_{12}}^{12}s^{N_{12}}}{1 + \frac{s}{p_1}} \\ Z_{21}(s) &= \frac{A_0^{21} + A_1^{21}s + \dots + A_{N_{21}}^{21}s^{N_{21}}}{s + \frac{s^2}{p_1}} \\ Z_{22}(s) &= \frac{A_0^{22} + A_1^{22}s + \dots + A_{N_{22}}^{22}s^{N_{22}}}{(1 + \frac{s}{p_1})(1 + \frac{s}{p_2})} \quad (2) \end{aligned}$$

where N_{ij} is known order of the numerator which is determined by equivalent circuit or obtained empirically, $s = \sigma + j\omega$ denotes complex frequency. We will determine rational functions for all Z parameters.

The polynomial in the numerator of parameter Z_{22} could be rewritten as

$$1 + \left(\frac{1}{p_1} + \frac{1}{p_2}\right)s + \frac{1}{p_1 p_2}s^2 \quad (3)$$

The poles of Z_{22} parameter are away from each other, $|p_1| \gg |p_2|$, so the equation (3) can be presented as

$$1 + \frac{s}{p_1} + \frac{1}{p_1 p_2}s^2 \quad (4)$$

If we denote $1/p_1 = B_1$ and $1/p_1 p_2 = B_2$, the rational functions can be separated on the real and imaginary part on real frequencies $s = j\omega$

$$\begin{aligned} Z_{11}(\omega) &= \frac{a_2^{11}\omega + \dots + a_2^{11} \lfloor \frac{N_{11}+2}{2} \rfloor \omega^{2 \lfloor \frac{N_{11}+2}{2} \rfloor - 1}}{\omega + b_1\omega^3} \\ &+ j \frac{a_1^{11} + \dots + a_2^{11} \lfloor \frac{N_{11}+2}{2} \rfloor - 1 \omega^{2 \lfloor \frac{N_{11}+2}{2} \rfloor}}{\omega + b_1\omega^3} \\ Z_{12}(\omega) &= \frac{a_0^{12} + \dots + a_2^{12} \lfloor \frac{N_{12}+1}{2} \rfloor \omega^{2 \lfloor \frac{N_{12}+1}{2} \rfloor}}{1 + b_1\omega^2} \\ &+ j \frac{a_1^{12}\omega + \dots + a_2^{12} \lfloor \frac{N_{12}+1}{2} \rfloor - 1 \omega^{2 \lfloor \frac{N_{12}+1}{2} \rfloor - 1}}{1 + b_1\omega^2} \end{aligned}$$

$$\begin{aligned} Z_{21}(\omega) &= \frac{a_2^{21}\omega + \dots + a_2^{21} \lfloor \frac{N_{21}+2}{2} \rfloor \omega^{2 \lfloor \frac{N_{21}+2}{2} \rfloor - 1}}{\omega + b_1\omega^3} \\ &+ j \frac{a_1^{21} + \dots + a_2^{21} \lfloor \frac{N_{21}+2}{2} \rfloor - 1 \omega^{2 \lfloor \frac{N_{21}+2}{2} \rfloor}}{\omega + b_1\omega^3} \\ Z_{22}(\omega) &= \frac{a_0^{22} + \dots + a_2^{22} \lfloor \frac{N_{22}+1}{2} \rfloor \omega^{2 \lfloor \frac{N_{22}+1}{2} \rfloor}}{1 + b_1\omega^2 + b_2\omega^4} \\ &+ j \frac{a_1^{22}\omega + \dots + a_2^{22} \lfloor \frac{N_{22}+1}{2} \rfloor - 1 \omega^{2 \lfloor \frac{N_{22}+1}{2} \rfloor - 1}}{1 + b_1\omega^2 + b_2\omega^4} \quad (5) \end{aligned}$$

where

$$\begin{aligned} a_l^{i1} &= \sum_{\mu=1}^l (-1)^{\lfloor \frac{l}{2} \rfloor + \mu} A_{l-\mu}^{i1} B_{\mu-1}; \\ l &= 1, \dots, M + N_{i1} + 1 \\ a_l^{ij} &= \sum_{\mu=0}^l (-1)^{\lfloor \frac{l}{2} \rfloor + \mu} A_{l-\mu}^{ij} B_{\mu}; \\ l &= 1, \dots, M + N_{1j} \quad (6) \end{aligned}$$

and

$$b_1 = B_1^2 \quad i \quad b_2 = B_2^2 - 2B_1 \quad (7)$$

for $B_0 = 1$.

The operator $[x]$ -rounds x to the nearest integer towards infinity, and $\lfloor x \rfloor$ -rounds x to the nearest integer towards minus infinity.

In the first step, we divide the imaginary and real part of (5), and equalize the result with the quotient of the imaginary and real part of the measured values

$$\frac{a_1^{i1}\omega_k + \dots + a_2^{i1} \lfloor \nu_1 \rfloor - 1 \omega_k^{2 \lfloor \nu_1 \rfloor - 1}}{a_0^{ij} + a_2^{ij}\omega_k^2 + \dots + a_2^{ij} \lfloor \nu_1 \rfloor \omega_k^{2 \lfloor \nu_1 \rfloor}} = p_k^{i1} \quad (8)$$

$$\frac{a_1^{ij}\omega_k + \dots + a_2^{ij} \lfloor \nu_0 \rfloor - 1 \omega_k^{2 \lfloor \nu_0 \rfloor - 1}}{a_0^{ij} + a_2^{ij}\omega_k^2 + \dots + a_2^{ij} \lfloor \nu_0 \rfloor \omega_k^{2 \lfloor \nu_0 \rfloor}} = p_k^{ij} \quad (9)$$

where

$$\nu_\lambda = \frac{N_{ij} + 1 + \lambda}{2}, \quad \lambda = 0, 1$$

and

$$p_k^{ij} = \frac{X_{ij}(\omega_k)}{R_{ij}(\omega_k)},$$

After polynomial coefficient normalization with α_1^{i1} , both in the numerator and denominator, eqn. (8) could be rewritten as

$$\frac{1 + \dots + \alpha_{2[\nu_1]-1}^{i1} \omega_k^{2[\nu_1]}}{\alpha_2^{i1} \omega_k + \dots + \alpha_{2[\nu_1]}^{i1} \omega_k^{2[\nu_1]-1}} = p_k^{i1} \quad (10)$$

Unknown coefficients $\alpha_2^{i1}, \alpha_3^{i1}, \dots, \alpha_{N_{i1}+2}^{i1}$ of network parameters Z_{i1} , are determined by solving following linear system of $n > N_{i1} + 2$ equations

$$\alpha_2^{i1} p_k^{ij} \omega_k + \dots + \alpha_{\eta}^{ij} \omega_k^{\eta-1} (-p_k^{ij})^{\frac{1+(-1)^\eta}{2}} = 1 \quad (11)$$

where $\eta = \max(2[\nu_1], 2[\nu_1] - 1)$.

The result of the overdetermined linear system of equations (11), for every given pair $i1$, in the least squares sense is

$$[\alpha] = ([S]^T [S])^{-1} [S]^T [p]$$

where

$$[S] = \begin{bmatrix} \omega_1 p_1^{i1} & -\omega_1^2 & \dots & \omega_1^{\eta-1} (-p_1^{i1})^{\frac{1+(-1)^\eta}{2}} \\ \omega_2 p_2^{i1} & -\omega_2^2 & \dots & \omega_2^{\eta-1} (-p_2^{i1})^{\frac{1+(-1)^\eta}{2}} \\ \vdots & & & \\ \omega_n p_n^{ij} & -\omega_n^2 & \dots & \omega_n^{\eta-1} (-p_n^{i1})^{\frac{1+(-1)^\eta}{2}} \end{bmatrix}$$

$$[\alpha] = [\alpha_2^{ij} \quad \alpha_3^{i1} \quad \dots \quad \alpha_{N_{i1}+2}^{ij}]^T$$

and

$$[p] = [p_1^{i1} \quad p_2^{i1} \quad \dots \quad p_n^{i1}]^T$$

Repeating this procedure one can obtain coefficients $\alpha_2^{i1}, \alpha_3^{i1}, \dots, \alpha_{N_{i1}+2}^{i1}$ for parameters Z_{11} and Z_{21} .

It is easy to show that the similar procedure could be performed for parameters having the coefficient $\lambda = 0$ [9]. In this case polynomial coefficients are normalized with α_0^{ij} both in the denominator and numerator

$$\frac{\alpha_1^{1j} \omega_k + \dots + \alpha_{2[\nu_0]-1}^{1j} \omega_k^{2[\nu_0]-1}}{1 + \dots + \alpha_{2[\nu_0]}^{1j} \omega_k^{2[\nu_0]}} = p_k^{1j} \quad (12)$$

The unknown coefficients $\alpha_1^{1j}, \alpha_2^{1j}, \dots, \alpha_{N_{1j}}^{1j}$ of network parameters Z_{1j} , are determined

by solving following linear system of $n > N_{1j} + 1$ equations

$$\alpha_1^{1j} \omega_k - \dots + \alpha_{\eta}^{1j} \omega_k^{\eta} (-p_k^{1j})^{\frac{1+(-1)^\eta}{2}} = p_k^{1j} \quad (13)$$

The result of the predetermined system of equations is

$$[\alpha] = ([S]^T [S])^{-1} [S]^T [p] \quad (14)$$

where

$$[S] = \begin{bmatrix} \omega_1 & -\omega_1^2 p_1^{1j} & \dots & \omega_1^{\eta} (-p_1^{1j})^{\frac{1+(-1)^\eta}{2}} \\ \omega_2 & -\omega_2^2 p_2^{1j} & \dots & \omega_2^{\eta} (-p_2^{1j})^{\frac{1+(-1)^\eta}{2}} \\ \vdots & & & \\ \omega_n & -\omega_n^2 p_n^{1j} & \dots & \omega_n^{\eta} (-p_n^{1j})^{\frac{1+(-1)^\eta}{2}} \end{bmatrix}$$

$$[\alpha] = [\alpha_1^{1j} \quad \alpha_2^{1j} \quad \alpha_3^{ij} \quad \dots \quad \alpha_{N_{1j}+1}^{1j}]^T$$

$$[p] = [p_1^{1j} \quad p_2^{1j} \quad p_3^{1j} \quad \dots \quad p_n^{1j}]^T$$

We now obtain normalized coefficients $\alpha_{1+\lambda}^{ij}, \dots, \alpha_{M+N_{ij}+\lambda}^{ij}$ for both $\lambda = 1$ and $\lambda = 0$.

In the second step of approximation one can obtain the denominator coefficients b_1, b_2 and normalization coefficients α_{λ}^{ij} . Equalizing absolute values of network parameters (5) with absolute measured values (1), one can obtain a linear system of equations

$$\frac{\sqrt{u_{11}^2(\omega_k) + v_{11}^2(\omega_k)}}{\omega + b_1 \omega_k^3} = \frac{q_k^{11}}{\alpha_1^{11}}$$

$$\frac{\sqrt{u_{12}^2(\omega_k) + v_{12}^2(\omega_k)}}{1 + b_1 \omega_k^2} = \frac{q_k^{12}}{\alpha_0^{12}}$$

$$\frac{\sqrt{u_{21}^2(\omega_k) + v_{21}^2(\omega_k)}}{\omega + b_1 \omega_k^3} = \frac{q_k^{21}}{\alpha_1^{21}}$$

$$\frac{\sqrt{u_{22}^2(\omega_k) + v_{22}^2(\omega_k)}}{1 + b_1 \omega_k^2 + b_2 \omega^4} = \frac{q_k^{22}}{\alpha_0^{22}} \quad (15)$$

where

$$\begin{aligned}
 u_{11}(\omega_k) &= 1 + \dots + \alpha_{2[\nu_{11}+\frac{1}{2}]}^{11} \omega_k^{2[\nu_{11}+\frac{1}{2}]} \\
 v_{11}(\omega_k) &= \alpha_2^{11} \omega_k + \dots + \alpha_{2[\nu_{11}+\frac{1}{2}]}^{11} \omega_k^{2[\nu_{11}+\frac{1}{2}]-1} \\
 u_{12}(\omega_k) &= \alpha_1^{12} \omega_k + \dots + \alpha_{2[\nu_{12}]-1}^{12} \omega_k^{2[\nu_{12}]-1} \\
 v_{12}(\omega_k) &= 1 + \dots + \alpha_{2[\nu_{12}]}^{12} \omega_k^{2[\nu_{12}]} \\
 u_{21}(\omega_k) &= 1 + \dots + \alpha_{2[\nu_{21}+\frac{1}{2}]-1}^{21} \omega_k^{2[\nu_{21}+\frac{1}{2}]-1} \\
 v_{21}(\omega_k) &= \alpha_2^{21} \omega_k + \dots + \alpha_{2[\nu_{21}+\frac{1}{2}]}^{21} \omega_k^{2[\nu_{21}+\frac{1}{2}]} \\
 u_{22}(\omega_k) &= \alpha_1^{22} \omega_k + \dots + \alpha_{2[\nu_{22}]-1}^{22} \omega_k^{2[\nu_{22}]-1} \\
 v_{22}(\omega_k) &= 1 + \dots + \alpha_{2[\nu_{22}]}^{22} \omega_k^{2[\nu_{22}]}
 \end{aligned}$$

$$\nu_{ij} = \frac{N_{ij} + 1}{2}, \quad i, j = 1, 2.$$

and

$$q_k^{ij} = \sqrt{R_{ij}^2(\omega_k) + X_{ij}^2(\omega_k)}.$$

This system can be presented as

$$\begin{aligned}
 b_1 \omega_k^3 + a_1^{11} h_k^{11} &= -\omega_k \\
 b_1 \omega_k^2 + a_0^{12} h_k^{12} &= -1 \\
 b_1 \omega_k^3 + a_1^{21} h_k^{21} &= -\omega_k \\
 b_2 \omega_k^4 + b_1 \omega_k^2 + a_0^{22} h_k^{22} &= -1
 \end{aligned} \tag{16}$$

where

$$h_k^{ij} = -\frac{\sqrt{u_{ij}^2(\omega_k) + v_{ij}^2(\omega_k)}}{q_k^{ij}} \tag{17}$$

for $k = 1, 2, \dots, n$.

The result of the linear system of equation in the least squares sense is

$$[b] = ([H]^T [H])^{-1} [H] [J] \tag{18}$$

where

$$[H] = \begin{bmatrix} \omega_1^3 & 0 & h_1^{11} & 0 & 0 & 0 \\ \omega_1^2 & 0 & 0 & h_1^{12} & 0 & 0 \\ \omega_1^3 & 0 & 0 & 0 & h_1^{21} & 0 \\ \omega_1^2 & \omega_1^4 & 0 & 0 & 0 & h_1^{22} \\ \omega_2^3 & 0 & h_2^{11} & 0 & 0 & 0 \\ \omega_2^2 & 0 & 0 & h_2^{12} & 0 & 0 \\ \omega_2^3 & 0 & 0 & 0 & h_2^{21} & 0 \\ \omega_2^2 & \omega_2^4 & 0 & 0 & 0 & h_2^{22} \\ \vdots & \vdots & \vdots & \vdots & \vdots & \vdots \\ \omega_n^2 & \omega_n^4 & 0 & 0 & 0 & h_n^{22} \end{bmatrix},$$

$$[b] = [b_1 \quad b_2 \quad a_1^{11} \quad a_0^{12} \quad a_1^{21} \quad a_0^{22}]^T$$

$$[J] = [-\omega_k \quad -1 \quad -\omega_k \quad -1 \quad -\omega_k \quad -1]^T$$

In the last step of approximation one can compute coefficients b_i and A_k^{ij} by solving equations (6) and (7).

III. EXAMPLE

We will test the above approximation procedure on the measured values of Z parameters of a $400\mu\text{m}$ GaAs MESFET with bias voltage $V_{DS} = 8V$. The frequency is in range of 1–30 GHz [1].

We use the values of Z parameter obtained by transistor equivalent circuit as the measured values which should be approximated by rational functions.

We have approximated the measured values with a great number of rational functions. They could be best approximated with the following orders of polynomials in numerators

$$N_{11} = 3, \quad N_{12} = 2, \quad N_{21} = 1, \quad N_{22} = 2$$

The set of rational functions is determined with 14 coefficients. The values of the coefficients of these rational functions are given in table I. It can be seen that only the polynomial in the numerator of Z_{21} parameter has one zero on the right-half plane because it is not a minimum-phase function. The other two-port parameters are minimum-phase functions.

The real and imaginary part of these rational functions and the measured values of Z -parameters are shown in the Figure 2.

Table I. The coefficients of Z parameters for $400\mu\text{m}$ GaAs MESFET

	A_0, B_1	A_1	A_2	A_3
A^{11}	1.47916866E + 11	4.76398753E + 01	9.93677290E - 10	3.15543756E - 20
A^{12}	1.12607526E + 01	2.86283036E - 10	1.70905549E - 21	
A^{21}	-2.75764662E + 12	1.39520494E + 02		
A^{22}	1.97397468E + 02	1.03126630E - 9	1.17841014E - 20	
B	1.25351430E - 10	6.46157550E - 22		

From the Figure 2 it can be seen that it is possible to approximate measured values of GaAs MESFET Z -parameters with rational functions which have lower orders of the numerators and denominators than orders of rational functions obtained by equivalent circuit. All rational functions have one common pole.

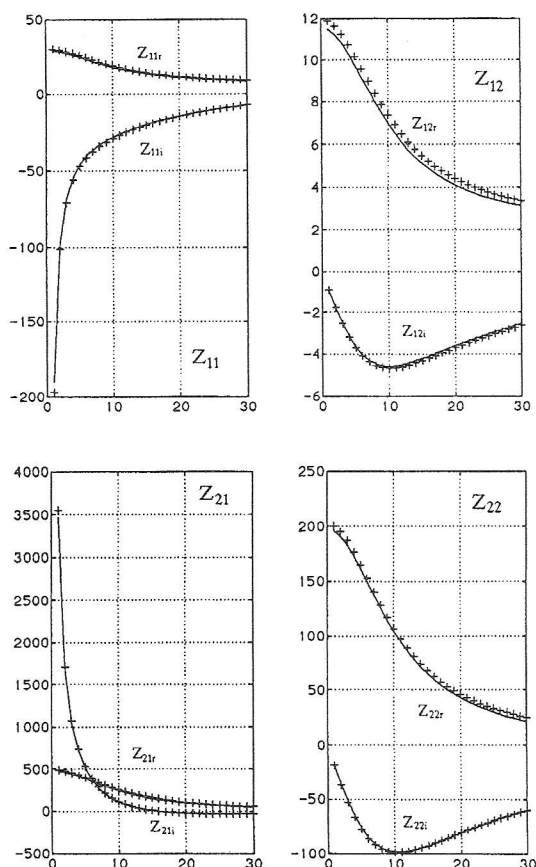


Figure 2. Real and imaginary part of Z -parameters GaAs FET. Plusses and asterisks are measured value of real and imaginary part, respectively. Lines: calculated values using rational function. Dashed-lines: calculated using equivalent circuit.

Figure 3 shows the absolute values and phases of the measured and approximated val-

ues of S parameters. Plusses denote measured values of the real and imaginary part, respectively. Lines denote values obtained by rational functions.

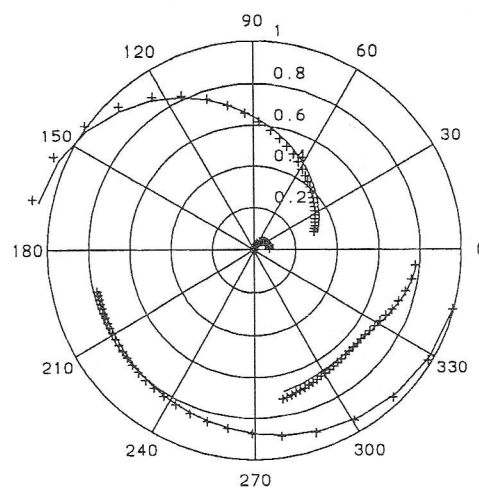


Figure 3. S parameters for $400\mu\text{m}$ GaAs MESFET. Plusses—measured values of real and imaginary part, Lines—approximation by rational functions

All computations were realized with the software package MATLAB. Double precision computation is not satisfying for these computations so the quadruple precision is well recommended for the approximation of the measured values by rational functions.

IV. CONCLUSION

In this paper, a least squares approximation procedure for the measured values of transistor Z parameters by rational functions is described.

Analyzing the GaAs FETs it is shown that some of the Z -parameters has one zero and pole which could be canceled so we can perform the approximation of Z -parameters with rational functions having lower order of polynomials than the functions obtained by equivalent circuit.

All Z -parameters have the same polynomial coefficients in the denominator. The procedure does not include computation of derivatives.

One example of Z -parameter approximation by rational functions is given in the last part of the paper. We analyzed $400\mu\text{m}$ GaAs MESFET. The real and imaginary part of Z -parameter rational functions are compared with the values of Z -parameters obtained by equivalent circuit.

The application of rational function is more convenient than application of equivalent circuit, because the software for network analyzing (for example PSPICE) is not required. These rational functions could be generally used in software for microwave network optimization.

BIBLIOGRAPHY

- [1] K. Nagatomo, Y. Daido, M. Shimizu, and N. Okubo "GaAs MESFET Characterization Using Least Squares Approximation by Rational Functions" IEEE Transactions on microwave theory and techniques, Vol. 41, No 2, pp. 199-206, February 1993.
- [2] E. Wasige, H. Ntchalhatou and G. Kompa: "An Analytical Modelparameter extraction procedure for GaAs FETs Based On Least Squares Approximation" in International IEEE workshop on Experimentally Based FET Device Modelling and Related Nonlinear Circuit Design, pp. 40.1-40.7, 1997.
- [3] K. Trondle, D. Krstić, H. Dirndorfen: "Methode zur Bestimmung breitbandiger Funktionserzatzschaltungen für Transistoren", AEU, 31, pp.436-438, 1997.
- [4] V. Stojanović, H. Dirndorfer: "Über den Entwurf eines hochratigen digitalen Übertragungssystems mit Hilfe der Pol-Nullstellen-Verteilung Frequenz 37, pp. 155-161, 1983.
- [5] L. Thiele: "An Analytic Approach to Curve Fitting AEU. Band 40, Heft 1, pp. 51-58, 1986.
- [6] L. Thiele: "An Algorithm for Rational Causal Approximation" AEU. Band 40, Heft 2, pp. 124-128, 1986.
- [7] V. Stojanović, D. Milovanović: "Über den Entwurf einer breitbandigen Funktionserzatzschaltung für Transistoren", 29. Intern. Wiss. Koll. TH Ilmenau, pp. 99-102, 1984.
- [8] Vidosav Stojanović and Saša Radovanović: "Least squares approximation of multi-port network parameters by rational functions" FACTA UNIVERSITATES ser. MATHEMATICS AND INFORMATICS, 1998.
- [9] Dean A. Frickey: "Conversions between S , Z , Y , h , $ABCD$ and T Parameters which are Valid for Complex Source and Load Impedances" IEEE Transactions on Microwave theory and techniques, vol. 42, pp. 205-211 No. 2, February 1994.

HF BIPOLAR INTEGRATED CIRCUITS

Nataša Banović, Branko L. Dokić, *Faculty of Electrical Engineering Banjaluka*

Abstract – The comparison of new active pull-down ECL (APD-ECL) circuits is given in this paper. We carried out the SPICE simulation using the $0.8\mu\text{m}$ bipolar parameters to compare time delay of various APD-ECL circuits versus load capacitance. In addition to our results in comparison of latest ECL topologies, this paper also presents the review of contemporary achievements in the field of high frequencies integrated circuits, especially in heterostructural junctions.

Keywords – Active pull-down (APD), Heterostructural junctions.

I. INTRODUCTION

High-speed multiplexers, demultiplexers, decision circuits and frequency dividers are the key components in high-speed optical communication systems. The significant factors in gate performance for high-speed communication applications are speed, noise margin, power dissipation and reliability. The Si bipolar integrated circuit with emitter coupled logic (ECL) is the most promising device for making practical ultra-high speed LSIs. The power dissipation of high-speed bipolar ECL circuits has long been known to limit their VLSI applications. Also, the speed of ECL circuits has been primarily limited by the pull-down transition time. The pull-down transition time is greater than the pull-up time because the output load capacitance is slowly discharged by the fixed current in the emitter-follower stage.

The development of new ECL circuits is characterized with much lower power consumption than conventional ECL. Various active pull-down (APD) schemes have been proposed to reduce the power consumption in the emitter-follower stage and improve the pull-down delay owing to the large transient pull-down current. These schemes are: APD ECL circuit with an ac-coupled active pull-down emitter-follower stage (AC-APD-ECL) [1], charge-buffered APD ECL (CB-APD-ECL) [2], ac-coupled complementary push-pull ECL (AC-PP-ECL) [3], direct-coupled complementary push-pull ECL (DC-PP-ECL) [4], ECL circuit with ac-coupled self-biased dynamic current source and APD emitter-follower stage (AC-CS-APD-ECL) [5], Darlington ECL circuit [6], cross-coupled APD ECL circuit (CC-APD-ECL) [7], compensated APD ECL circuit with self-adjusting driving capability (FC-APD-ECL) [8], ECL circuit with self-biased feedback-controlled pull-down emitter-follower (FPD-EF-ECL) [9], compensated nonsaturating APD (CNS-APD-ECL) [10], feedback controlled current source in an APD ECL circuit

(FCCS-APD-ECL) [11], capacitor-free level-sensitive APD ECL circuit with self-adjusting driving capability (LS-APD-ECL) [12]. The comparison of these circuits is presented in this paper. In all of the cases it is essential to reduce the power consumed by the ECL circuit and yet maintain the driving capabilities and switching speed. But, many of these circuits have onerous restrictions, such as requiring high performance pnp devices, special capacitor structures, loss of wired-OR capability and use of both, true and complement gate outputs. The review of contemporary achievements in the field of high frequencies bipolar integrated circuits, especially in heterostructural junctions, is also discussed.

II. COMPARISON OF APD ECL AND ECL PERFORMANCE

The essence of a high-speed, low power operation is the ability to achieve both a low standby current and a large dynamic current during the switching transient. The current and logical voltage levels in bipolar circuits are typically set by passive resistors. That is the reason for a high DC power consumption and a slow pull-down transition. The approach of overcoming these constraints is by replacing the passive resistors with active devices. When applied to the emitter follower resistor, this approach results in various active pull-down schemes [13].

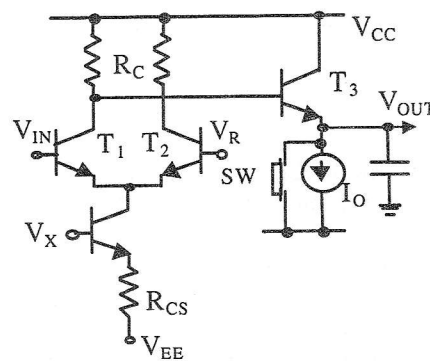


Fig. 1. Conceptual schematic of a high-speed/low power ECL gate.

Conceptual schematic of a high-speed/low-power ECL gate is given in Fig. 1. An active pull-down element acts like a switch (SW) in parallel with a small standby current source. The switch must be controlled by the logic stage to provide a large transient pull-down current consistent with the logic inputs. At steady state, the SW is opened, and I_O maintains a low DC current through the emitter-follower T_3 . During the output high-to-low transition,

the SW is closed and draws a large transient current from the output node, pulling it down quickly.

AC coupling has the advantage of completely blocking the DC signal. Special device elements, like capacitors and charge buffered diodes, may be needed. The AC coupled active pull-down ECL circuit utilizes a capacitor to couple a transient voltage pulse to the base of an npn pull-down transistor (Fig. 2.a). This reduces the DC power consumption in the emitter-follower stage, and the large transient pull-down current improves the pull-down delay (Fig. 2.b) [1].

Another approach is to replace capacitor with charge-buffered coupling, which results in the charge-buffered APD ECL (CB-APD-ECL) [2].

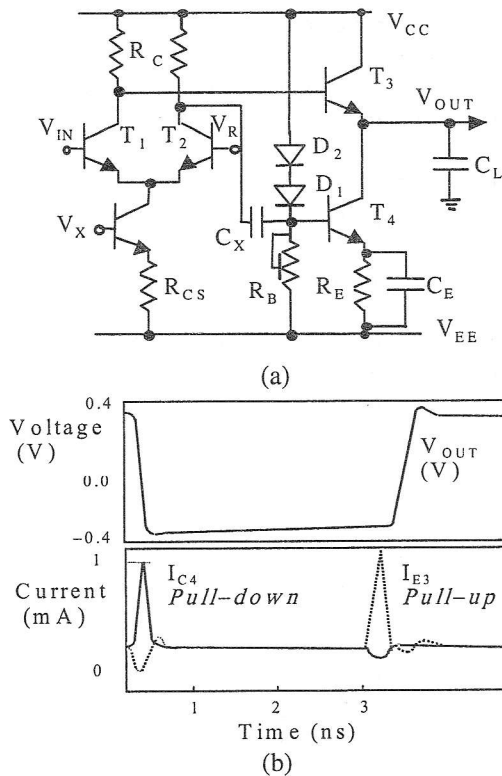


Fig. 2. AC-APD-ECL circuit (a), output voltage and current waveforms for the APD-ECL circuit (b).

Complementary push-pull approaches typically offer the most significant improvement on power/speed and load-driving capabilities, although at the expense of complicated process technology [3] [4]. Several other very effective ECL circuits were reported [5] [6] [7] [8], most notably the circuit named FPD-EF-ECL [9]. This circuit has a remarkable simplicity and allows versatile logic implementations through collector-dotting and emitter-dotting. CNS-APD-ECL circuit, presented in [10], has high active/inactive current ratio. It uses a clamp voltage to compensate variations in supply and temperature. The circuit is stable and is not prone to oscillation or excessive ringing. FCCS-APD-ECL [11] has good product power-delay. Also, the ability to drive large capacitive loads is substantially improved.

Very good performances has capacitor-free level-sensitive APD ECL circuit with self-adjusting driving capability (LS-APD-ECL) [12].

A. Simulation results

For comparison purposes, the performances of various APD-ECL circuits are assessed by SPICE simulation using transistor models based on a sub-micron process (0.8 μ m bipolar parameters). The typical device parameters are listed in Table 1. We have compared time delay of conventional ECL and various APD-ECL circuits versus load capacitance. The results, including both, rise time and fall time, are given in Table 3. Their graphic presentation is given in Fig. 3. The superior load driving capability of APD-ECL circuits is visible. At 2mW/gate, the pull-down driving capability of the FPD-EF or CNS-APD-ECL circuits is almost identical to the pull-up capability. The LS-APD-ECL and ACCS-APD-ECL have a faster pull-down transition than a pull-up for heavy loads. The performance advantages of the APD-ECL circuits over conventional ECL are shown in the simulated power-delay curves in Fig. 4. Specific data is given in Table 2.

Table 1. Typical device parameters at 0.8 μ m design rule.

Device	npn	pnp
Design Rule	0.80 μ m	0.80 μ m
A_E (Wafer, μ m ²)	0.50x4.0	0.50x4.0
Base Transit Time	6.0 ps	6.0 ps
C_{EB}	6.6 fF	16 fF
C_{CB}	3.9 fF	14 fF
C_{CS}	12 fF	9.3 fF
R_E	14 Ω	15 Ω
R_B	164 Ω	82 Ω

Table 2. Specific data.

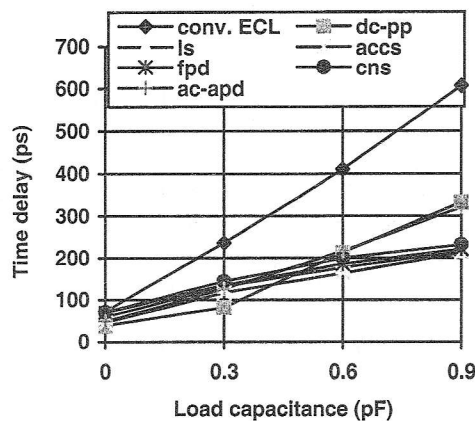
	P=2mW/gate	$C_L=0.3$ pF
Conv. ECL	592 ps/pF	167 ps/mW
AC-APD-ECL	303 ps/pF	50 ps/mW
FPD-EF-ECL	168 ps/pF	77 ps/mW
CNS-APD-ECL	177 ps/pF	65.5 ps/mW

III. HETEROSTRUCTURAL JUNCTIONS

Modern communication systems require low-cost radio-frequency (RF) integrated circuits for frequencies at or above 1 GHz. The application frequency continues to climb, so various analog applications are in multi-GHz frequency range [14]. Advanced silicon technologies are starting to enter the market formerly occupied by GaAs FET technology. The advantages of silicon technologies in relation to GaAs are: chip costs, a higher integration level, good thermal conductivity, low leakage currents and the ability to integrate logic functions.

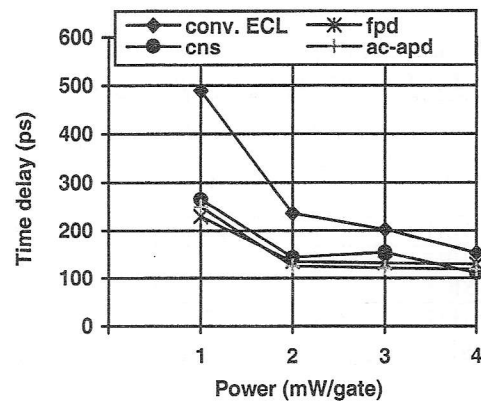
Table 3. Delay versus load capacitance for various APD-ECL circuits.

LOAD CAPACITANCE, C_L [pF]		UNLOADED CIRCUIT	0.3 pF	0.6 pF	0.9pF
Conventional ECL circuit	Rise time, [ps]	60.00	148.36	166.50	212.00
	Fall time, [ps]	86.20	324.70	656.00	1000.00
	Average delay, [ps]	73.10	236.50	411.20	606.00
Basic AC-APD-ECL circuit	Rise time, [ps]	49.60	125.00	166.00	212.40
	Fall time, [ps]	47.80	127.93	268.20	430.00
	Average delay, [ps]	48.70	126.50	217.10	321.20
DC-PP-ECL circuit	Rise time, [ps]	36.10	120.25	158.37	189.00
	Fall time, [ps]	39.57	42.00	268.81	478.49
	Average delay, [ps]	37.85	81.12	213.60	333.70
LS-APD-ECL circuit	Rise time, [ps]	70.00	156.00	205.00	241.46
	Fall time, [ps]	49.00	108.60	150.24	192.41
	Average delay, [ps]	59.50	132.30	177.62	216.94
ACCS-APD-ECL circuit	Rise time, [ps]	58.26	142.00	197.35	260.00
	Fall time, [ps]	33.00	90.00	130.00	164.00
	Average delay, [ps]	45.63	116.00	163.67	212.00
CC-APD-ECL circuit	Rise time, [ps]	63.80	128.00	174.68	212.24
	Fall time, [ps]	125.00	290.00	480.30	704.3
	Average delay, [ps]	94.40	209.00	327.50	458.27
FPD-EF-ECL circuit	Rise time, [ps]	58.00	126.00	179.50	215.46
	Fall time, [ps]	81.80	143.00	192.29	227.50
	Average delay, [ps]	69.90	134.50	185.90	221.50
CNS-APD-ECL circuit	Rise time, [ps]	66.00	131.00	198.00	216.00
	Fall time, [ps]	77.73	156.00	201.14	247.23
	Average delay, [ps]	71.86	143.50	199.60	231.62

**Fig. 3.** Delay versus load capacitance at $P=2\text{mW/gate}$, ($V_{EE}=-3\text{V}$, $\Delta V \approx 800\text{mV}$, $f=100\text{MHz}$).

The major disadvantage of silicon bipolar technology for communication systems is the low breakdown voltage which is also the reason for the limitation of the current gain to the value of $\beta=140$. Heterostructural bipolar transistors (HBTs) have better performances than homostructural bipolar transistors. They have higher current gain ($\beta=n \times 100$), lower base resistance and higher cutoff frequency (Fig. 5). The current gain for the heterostructural transistor approximately is [15]:

$$\beta \approx \beta_1 e^{\Delta V_G / \phi_t} \approx \left(\frac{N_e D_n W_e}{N_b D_p W_b} \right) e^{\Delta V_G / \phi_t}, \quad (1)$$

**Fig. 4.** Simulated power-delay curves of loaded ($C_L=0.3\text{pF}$) AC-APD, FPD-EF, CNS-APD and conventional ECL ($V_{EE}=-3\text{V}$, $\Delta V \approx 800\text{mV}$, $f=100\text{MHz}$).

where β_1 is a current gain of homostructural transistor, N_e and N_b are doping concentrations in emitter and base, D_n and D_p are diffusion constants of electrons and holes, W_e and W_b are emitter and base widths, ΔV_G is a voltage different in energy gaps of heterojunction materials, ϕ_t is a temperature potential. Since ΔV_G can achieve $n100\text{mV}$ ($V_G(\text{Ge})=0.72\text{eV}$, $V_G(\text{Si})=1.12\text{eV}$, $V_G(\text{GaAs})=1.4\text{eV}$, $V_G(\text{AlGaAs})=1.8\text{eV}$) from Eq. (1) follows that β is much greater than β_1 . For a given current gain SiGe HBT does not require high difference in a doping concentration of base and emitter, so it allows a high base doping concentration.

That is the reason for a lower base resistance and higher cutoff frequency.

There are HBTs in GaAs, Si and SiGe technology. The low breakdown voltage BV_{CEO} is not a problem specific to SiGe technology. From designer's point of view SiGe heterojunction bipolar transistors are very similar to Si bipolar junction transistors (BJTs). SiGe HBT has a high speed and high gain at lower current density because of reduced base-emitter capacitance. Also, for a given collector current density SiGe HBT requires a lower input voltage, what is very useful when moving to lower supply voltages. The comparison of advanced Si BJT, standard HBT and HBTs designed for higher breakdown voltages is given in Table IV. A higher breakdown voltage results in degradation of f_T and f_{max} [16].

Today, the most promising production technologies are based on self-aligning double-polysilicon processes. To improve device characteristics, it is necessary to reduce the parasitic capacitance between base and collector regions and also to make shallower junctions. SiGe base bipolar transistors are fabricated using self-aligned processes. A maximum cutoff frequency of 113 GHz was obtained using the SiGe drift base technique with a germanium fraction of 25% at the base/collector junction [17].

Table 4. Technological parameters for advanced Si bipolar process and several SiGe HBTs.

Technology	BV_{CEO} (V)	BV_{CB0} (V)	f_T (GHz)	f_{max} (GHz)
Advanced Si BJT	2.9	10	36	38
SiGe HBT	2.5	9.9	61	74
SiGe HBT with SIC*	3.5	9	50	50
SiGe HBT no SIC*	6.0	13	30	55

*SIC - Selective Implanted Collector.

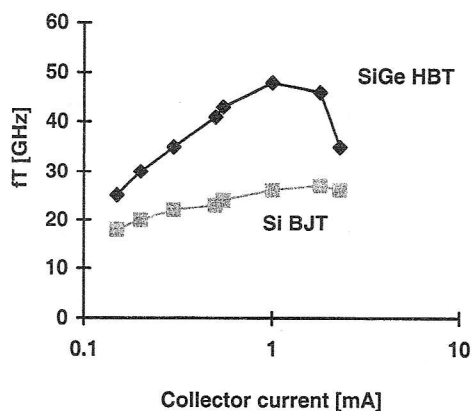


Fig. 5. Cutoff frequency f_T for SiGe HBT and Si BJT versus collector current ($A_E=0.5 \times 2.5 \mu m^2$).

IV. CONCLUSION

The major disadvantage of conventional ECL circuits is the reciprocal relationship of the pull-down delay and DC power. To solve this problem various active-pull-down circuits have been proposed. All of these circuits have better performances in comparison to the conventional ECL. The average driving capability is improved from 592 ps/pF (conv. ECL) to 168 ps/pF (FPD-EF-ECL). From the power savings point of view, almost all APD-ECL circuits consume 2x less, than the conventional ECL, for the same delay.

Si/SiGe heterojunction bipolar transistors have been used to implement high speed bipolar and BiCMOS LSIs. Higher doping concentration in the base than in the emitter has made it possible to reduce base resistance and to reach cutoff frequencies above 100 GHz.

REFERENCES

- [1] K. Y. Toh, *et al.*, "A 23-ps/2.1mW ECL Gate with an AC-Coupled Active Pull-Down Emitter-Follower Stage", *IEEE Journal of Solid-State Circuits*, vol. 24, No.5, pp. 1301-1306, Oct. 1989.
- [2] C. T. Chuang, K. Chin, "High-Speed Low-Power Charge-Buffered Active Pull-Down ECL Circuit", *IEEE Journal of Solid-State Circuits*, vol. 26, No. 5, pp. 812-815, May 1991.
- [3] C. T. Chuang, D. D. Tang, "High-Speed Low-Power AC-Coupled Complementary Push-Pull ECL Circuits", *IEEE Journal of Solid-State Circuits*, vol. 27, No.4, pp. 660-663, April 1992.
- [4] C. T. Chuang, K. Chin, "High-Speed Low-Power Direct-Coupled Complementary Push-Pull ECL Circuit", *IEEE Journal of Solid-State Circuits*, vol. 29, No. 7, pp. 836-839, April 1994.
- [5] C. T. Chuang, *et al.*, "High-Speed Low-Power ECL Circuit with AC-Coupled Self-Biased Dynamic Current Source and Active-Pull-Down Emitter-Follower Stage", *IEEE Journal of Solid-State Circuits*, vol. 27, No. 8, pp. 1207-1210, August 1992.
- [6] C. T. Chuang, *et al.*, "High-Speed Low-Power Darlington ECL Circuit", *IEEE Journal of Solid-State Circuits*, vol. 28, No. 12, pp. 1374-1376, Dec. 1993.
- [7] C. T. Chuang, *et al.*, "High-Speed Low-Power Cross-Coupled Active Pull-Down ECL Circuit", *IEEE Journal of Solid-State Circuits*, vol. 30, No. 6, pp. 701-705, June 1995.
- [8] K. Ueda *et al.*, "A Fully Compensated Active Pull-Down ECL Circuit with Self-Adjusting Driving Capability", *IEEE Journal of Solid-State Circuits*, vol. 31, No.1, pp. 46-53, Jan. 1996.
- [9] H. J. Shin, "A Self-Biased Feedback-Controlled Pull-Down Emitter Follower for High-Speed Low-Power Bipolar Logic Circuits", *IEEE Journal of Solid-State Circuits*, vol. 2

9, No. 4, pp. 523-528, Apr. 1994.

- [10] N. P. Jouppi, "A Fully-Compensated APD Circuit with 10:1 Ratio Between Active and Inactive Current", Bipolar/BiCMOS Circuits and Technology Meeting, pp. 111-114, 1994.
- [11] V. G. Oklobdzija, "An ECL Gate with Improved Speed and Low-Power in a BiCMOS Process", *IEEE Journal of Solid-State Circuits*, vol. 31, No. 1, pp. 77-83, Jan. 1996.
- [12] T. Kuroda *et al.*, "Capacitor-Free Level-Sensitive Active Pull-Down ECL Circuit with Self-Adjusting Driving Capability", *IEEE Journal of Solid-State Circuits*, vol. 31, No. 6, pp. 819-827, June 1996.
- [13] N. Banović, B. L. Dokić, "Basic VLSI and ULSI ECL cells", *Proceedings of Intel*, Banjaluka 1997.
- [14] D. Hame, "High Performance BiCMOS Process Integration: Trends, Issues and Future Directions", *IEEE BCTM*, pp. 36-43, 1997.
- [15] B. L. Dokić, *Integrisana kola - digitalna i analogna*, Glas srpski, Banjaluka, 1999.
- [16] R. Gotzfried, "Design of RF Integrated Circuits Using SiGe Bipolar Technology", *IEEE Journal of Solid-State Circuits*, vol. 33, No. 9, pp. 1417-1422, Sept. 1998.
- [17] T. Nakamura *et al.*, "Recent Progress in Bipolar Transistor Technology", *IEEE Transactions on Electron Devices*, vol. 42, No. 39, pp. 390-398, March 1995.

ANALYSES OF STRUCTURE DESIGN AND I_{DS} , NONLINEAR MODELING FOR 5-WATT MULTI-CELL MICROWAVE GaAs MESFET

Yifan Gao¹, Cong Gu²

¹Xian Highway University, China

²Shaanxi Lishan Microelectronics Institute, China

Abstract – The characteristics are described about GaAs MESFET with 5-watt large-gate-width multi-cell structure, including optimal structure design, processes and high breakdown voltage and overcurrent capacity. Also, we put forward the modified I_{DS} nonlinear model, and the agreement with experiment using this typical model was better than the results by directly employing the common models.

Keywords – GaAs MESFET, EMS, Large signal model

I. INTRODUCTION

Nowadays, state-of-the-art microwave power GaAs FETs are extensively used in a wide variety of practical radar, communication, navigation, and sensing system at microwave and even millimeter wave frequencies. Such applications are numerous as test instrumentation, satellite and electronic communication, electronic warfare, electronic scanning through phased arrays, direct broadcast satellite T/R module.

But in microwave power GaAs MESFET design, one of the main problems is that an effective gate width must be much large based on 0.5W/mm power density rule if output power is larger than SW. Meanwhile many other factors should be considered which affect the device performance, i.e. heat sinking, high breakdown voltage and overcurrent capacity etc.. This paper describes that the combination of conventional structure design and novel processes make the FET's best performances, also, we set up the improved nonlinear model to simulate this typical FET I-V characteristics.

II. DESIGN AND PROCESS

Firstly, the FET designed has the following basic structure specifications (shown in Fig. 1), 0.5 μ m of gate-length, 150 μ m of single finger gate-width, 145 μ m of an effective finger gate-width, 12.6mm of overall gate-width, 12.06mm of an effective total gate-width. It is composed of six cells. Each cell has 14 gate-fingers. The gate structure was recessed in sub-micron, and the active regions were formed by Si²⁹⁺ ionized implantation. The maximum saturation current (I_{dss}) is larger than 2.4A and the maximum breakdown voltage is higher than 20V. The Ohm contact resistance ratio ranges from 1.8 to 1.9 % 10⁻

7 Ω /cm². Owing to the FET thickness reduced, only 40 to 50 μ m, the heat sinking requirement was also fitted for. In addition, because the stressless Si₃N₄ layer was grown on the GaAs substrate, the piezoelectric effect was eliminated, which FET passivation processes have realized.

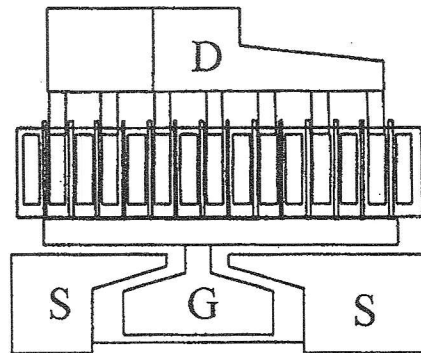


Fig. 1. Plane schematic of one cell: G-gate pad, D-drain pad, S-source pad

Secondly, eight gate pads and seven pads are laid on, as shown in Fig. 2, although this typical FET consists of six cells. One is to shield the gate bonding pads from the interference of outer electromagnetic field, the other is to keep all signals in balance, aiming at increasing the efficiency of power combiner, and also preventing the burnout from the FET self excitation.

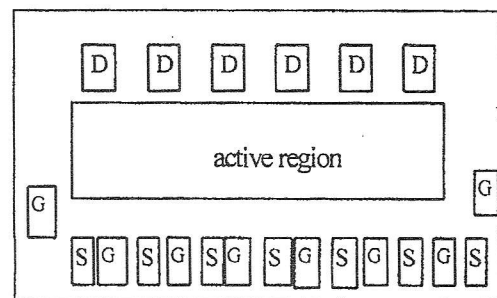


Fig. 2. FET layout of bonding pads

Thirdly, the good Ohm contact resistances are fabricated by complicated processes of the electron beam-heat evaporation and separate evaporation after the wafers were cleaned with the ionized beam. Then the AuGeNi layers fabricated were under the fast metalization. The stability of typical Ohm contact is quite well. This performance is experimented under the 1000A/cm² current through 1600 hours, the

resistance ratio is no apparently changed. The other main process is to increase the breakdown voltage above 20V, by controlling the recessed slope formation eroded by using proportionally different solutions. Therefore this typical FET has many over-advantages, and can be employed in the practical application of hybrid MIC.

III. I_{ds} NONLINEAR MODELING AND SIMULATION

For microwave power FET, necessarily, the nonlinear characteristics should be predicted and simulated in order to obtain the ultimate power output available, because power FET often works in large signals. The other reason is that the conventional device theories such as Shockley gradual channel approximation could not be used in modern submicron GaAs MESFET model. Recently starting with a computer simulation of the device or circuit using two-dimension (2-D) numerical model with rigorous varied boundary condition, although more accurate, is not suitable for use in circuit analysis because of its complexity and numerous parameters. Thus paying attention to the identification of physical mechanisms for the understanding of submicron microwave MESFET, a generally accepted DC model, simple, compact and minimum number of variables, can predict device characteristic trends regardless of size, and for a given device size it can predict the characteristics for all variables. Presently, a variety of nonlinear models used to simulate the MESFET dc characteristics, claim to satisfy the required criteria. We have done the comparative accuracy of the following models through studying, they are three commonly employed models in circuit design, 1) Curtice model [1], [2]; 2) Kacprzak-Materka model [4]; 3) Statz model [3]; 4) A newly improved model, is put forward here based on summed up almost all previous nonlinear theories proposed [5], [6], [7], [8], [9]. The four models compared here shared the topology shown in Fig. 3.

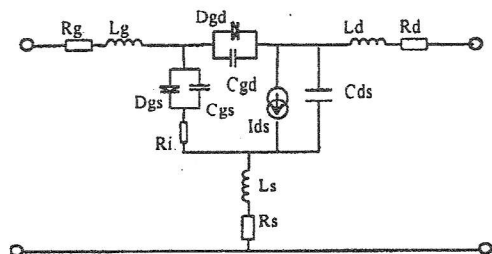


Fig. 3. Common model topology for four model
A newly modified large-signal model for 5W 12.6mm multi-cell microwave power GaAs MESFET is mainly the analytical expressions of $I_{ds}(V_{gs}, V_{ds})$ element operating at microwave frequency. In modeling the several principles is abided by during the deriving model. Firstly, I_{ds} , formulae has fast

convergence, consists of hyperbolic tangent function (TANH) term, has continuity of its first- and second-order differential function, and is dependence of both V_{gs} and V_{ds} .

Secondly, the parameters should be fewer, and the physical interpretations should have in these parameters. Thirdly, the analytical expressions should be fairly simple, not complex.

According to the above-mentioned rules, the analytical formula of the large signal model for microwave high power MESFET are improved and derived. They seem to predict correctly almost all the important trends. The model proposed here is much simpler and its parameters can be interpreted on the DC characteristics. The model has the following expressions:

$$I_{ds} = \begin{cases} I_{dss} \left(1 + \frac{V_{gs}}{V_t}\right)^{(1+\beta V_{gs})^2} \left(1 - \lambda \frac{V_{gs}}{V_t}\right) \tanh(\alpha V_{gs}) & V_t \leq V_{gs} \\ 0 & V_t < V_{gs} \end{cases} \quad (1)$$

$$V_t = V_{t0} + V_{go} + \gamma V_{ds} \quad (1a)$$

Where I_{dss} is saturation current; V_{t0} is threshold voltage of an ideal FET ($V_{t0} = V_p - V_{bi}$, where V_p is pinch-off voltage); β , γ and α are parameters.

Comparison of the model presented with three kinds of the original formula proposed by Materka, Statz and Curtice, using Eq. (2) as RMS error values, we found that the modified I_{dss} , in here are more accuracy. From Fig. 4 and Table I, the model shows that it gives an excellent agreement between measured and calculated I-V characteristics for microwave power GaAs MESFET.

$$RMS = \left(\sum_{i=1}^n |I_{dsi} - \overline{I_{dsi}}|^2 \right)^{1/2} \quad (2)$$

TABLE I
RMS. COMPARISON FOR FOUR MODELS

Model	GaAs MESFET
Statz	$5.283\% \cdot 10^{-2}$
Materka	$4.746\% \cdot 10^{-2}$
Curtice	$8.524\% \cdot 10^{-2}$
Paper resenting	$3.546\% \cdot 10^{-2}$

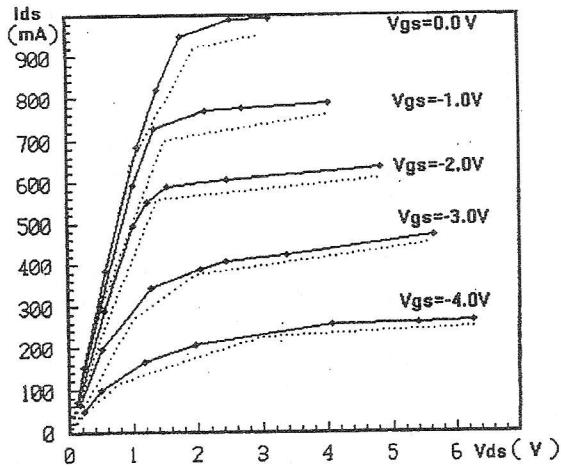


Fig. 4. Comparison of measured and computed data for 6X 0.5 X 150um FET. Black dots – measured
Dashed line – Curtice model, Real line – modified model.

IV. CONCLUSION

A microwave power FET with six-cell 5W has been fabricated, and nonlinear characteristics have been studied for the further application such as multi-FETs combiner for the higher power output. The only drawback in analytical FET models that are used in circuit simulation is that the parameters are dependent on processes adding semi-empirical values. Its application is limited.

BIBLIOGRAFY

- [1] M. Shur, "Analytical Model of GaAs MESFET", *IEEE Trans. Electron Devices*, vol 25, Jun 1978, pp. 612-618.
- [2] W. R. Curtice, "A MESFET Model for Use in the Design of GaAs Integrated Circuits", *IEEE Trans. MTT.*, vol MTT-28, 1980, pp. 448-446
- [3] H. Statz, et al, "GaAs FET Device and Circuit Simulation in SPICE", *IEEE Tran, Electronic Devices*, vol 34, Feb. 1987, pp 160-169.
- [4] Materka, T. Kacprzak, "Computer Calculation of Large-signal GaAs FET Amplifier Characteristics", *IEEE Trans. MTT.*, vol MTT-33, Feb. 1985, pp. 129-135.
- [5] Y. Tajima, et al, "Design of Broad-Band Power GaAs FET Amplifiers", *IEEE Trans. MTT.*, vol MTT-32, Mar. 1984, pp. 261-267.
- [6] K. Jastrzebski, *IEEE Colloquium on Large Signal Devices Model and Parameter Extraction for Circuit Simulation*, London, 1988.
- [7] J. McCamant, et al, "An Improved GaAs MESFET Model for SPICE", *IEEE Trans. MTT.*, vol MTT-37, Aug. 1989, p.822.
- [8] D. E. Root, et al, "Technology-Independent Large-signal FET Models: A Measurement-Based Approach to Active Device Modeling", *Proc. 15th ARMMS Conference*, Bath, English, Sept. 1991.
- [9] Rodriguez, et al, "A New Highly Accurate Microwave Nonlinear MESFET Model", *Microwave J.*, vol. 36, No. 5, Mar. 1993, pp. 280-285.

MICROWAVE FET TRANSISTOR NOISE MODELING USING NEURAL NETWORKS

Vera Marković, Zlatica Marinković

Abstract - Noise modeling of microwave FET transistor (MESFET) by using multilayer neural network approach is presented in this paper. We extracted four noise parameters in terms of conventional small-signal intrinsic equivalent circuit elements and three equivalent temperatures. A four layer neural network was used for successful representation. The results obtained by using neural network are compared with measured data available in manufacturers' catalogues.

Keywords - Neural network, modeling, microwave, MESFET, noise parameters.

I. INTRODUCTION

A neural network has recently gained attention as a fast and flexible vehicle to microwave modeling, simulation and optimization. The neural network can be considered as a matrix function which provides an approximate model of the system. The structure of this function is defined a priori and depends on the type of the problem to deal with (identification, classification, pattern recognition, speech processing, control). The parameters characterizing the neural network are computed for the specific application as a result of an optimization procedure (training process). In this way, proper representation of system response to a given set of input conditions is provided. When the specific set of parameters is computed, the neural network model is defined and can be used for the prediction of the response to new input vectors, without requiring any further computational effort. Neural network capability to provide correct answer to the input which is not included into training set (generalization capability) is the strongest motive for further investigation in the neural network area.

A multilayer perceptron (MLP) network [1] is the most widely used architecture of neural network because its structure is not complex and it is easy to be accomplished. MLP neural network belongs to the type of the classical black-box model. We can neither see nor embed functional dependence into data flow of model, but this dependence is extracted from training data. Therefore, large amount of training data is usually needed to ensure model accuracy. In the training process of neural network, the training data are obtained by either simulation or measurement.

Recently, neural network has successfully been applied to modeling of microwave transistor static characteristics [1].

The full-noise characterization of microwave FET transistors requires the determination of theirs

four noise parameters (minimum noise figure F_{min} , normalized equivalent noise resistance r_n , magnitude and angle of optimum reflection coefficient Γ_{opt}). Since in the microwave frequency range the measurement of the noise parameters is a difficult task, noise models of FET transistors are commonly included in standard microwave software and used in computer aided design (CAD) of microwave circuits.

In the previous work [2], the authors of this paper have developed a procedure for efficient noise prediction of microwave FET transistors extending Pospieszalski's noise model based on using two noise sources [3] by including the correlation between them. A procedure for this model implementation within input files of program Libra [4] was developed.

In this paper we apply neural network approach to noise modeling of microwave FET transistors by using a program NeuroModeler developed by one of the authors of the reference [1]. The learning process is accomplished by using computational results referring to simulated model of different MESFET transistors. The trained neural network is tested for NEC transistor N71000A.

II. MULTILAYER NEURAL NETWORK

A standard multilayer neural network is shown in Fig.1. [5].

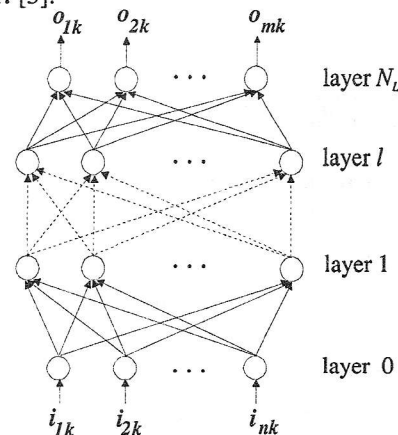


Fig.1. MLP neural network

In this figure, neurons represented by circles are grouped in N_L layers. The l^{th} layer includes N_l neurons. This network consists of an input layer (layer 0) which includes n neurons, an output layer (layer N_L) which includes m neurons, as well as hidden layers.

Neural network is learnt by using data from training set $P = \{p_1, p_2, \dots, p_{N_p}\}$. The sample p_k is

defined by input vector $i_k = (i_{1k} i_{2k} \dots i_{nk})^T$ and by desired output vector $t_k = (t_{1k} t_{2k} \dots t_{mk})^T$, i.e. $p_k = (i_k, t_k)$. On the other hand a network response to the input signal i_k is $o_k = (o_{1k} o_{2k} \dots o_{mk})^T$.

In the considered neural network $v_i^{(l)}$ denotes i th neurons in layer l , while $\varpi_{ij}^{(l)}$ denotes synaptic weight between the output of neuron $v_j^{(l-1)}$ and i th input of neuron $v_i^{(l)}$. When i_k is at the network input, the signal at i th input of neuron $v_j^{(l)}$ is $u_{ijk}^{(l)}$. In this case, the output of neuron $v_j^{(l)}$ is $v_{jk}^{(l)}$. Since, the output signal of neuron $v_i^{(l-1)}$ is led to i th input of neuron $v_j^{(l)}$, then $u_{ijk}^{(l)} = v_{ik}^{(l-1)}$. Finally, as network outputs are outputs from N_L th layer, then: $o_{ik} = v_{ik}^{(N_L)}$.

Each neuron is characterized by an input interaction function (activation signal), an activation function and a threshold level of the activation function. When i_k is at the network input the activation signal of neuron $v_j^{(l)}$ is denoted as $x_{jk}^{(l)}$.

An output signal from this neuron is [5]:

$$v_{jk}^{(l)} = g_j^{(l)}(x_{jk}^{(l)}) \tag{1}$$

where $g_j^{(l)}(x)$ is the activation function.

All neurons have linear input interaction function. Therefore, activation signal of neuron $v_j^{(l)}$ is:

$$x_{jk}^{(l)} = \sum_{i=0}^{N_{l-1}} \varpi_{ij}^{(l)} u_{ijk}^{(l)} = \sum_{i=0}^{N_{l-1}} \varpi_{ij}^{(l)} v_{ik}^{(l-1)} \tag{2}$$

Neurons from input layer have linear activation function, i.e. $v_{ik}^{(0)} = i_{ik}$, while other neurons have a smooth switch function such as sigmoid function $g(x) = 1/(1 + e^{-x})$. A real neuron with a threshold level θ is represented by binary neuron that has one constant input more with zero threshold level, $u_{0jk}^{(l)} = v_{0k}^{(l-1)} = 1$ and $\varpi_{0j}^{(l)} = \theta$.

The basic purpose of the training is to minimize the difference between the desired output t_k and the actual outputs o_k , obtained when i_k is at network input. Thus, the error function can be defined as follows:

$$\epsilon_k = \frac{1}{2} \sum_{s=1}^m (o_{sk} - t_{sk})^2 = \frac{1}{2} \sum_{s=1}^m (v_{sk}^{(N_L)} - t_{sk})^2 \tag{3}$$

The weights are determined iteratively, so the partial derivatives of the error function over the weights have to be determined:

$$\frac{\partial \epsilon_k}{\partial \varpi_{ij}^{(l)}} = \frac{\partial \epsilon_k}{\partial x_{jk}^{(l)}} \frac{\partial x_{jk}^{(l)}}{\partial \varpi_{ij}^{(l)}} \tag{4}$$

In this case, it is necessary to know not only the neuron states from layer below but also partial derivatives from layer above.

This problem can be solved successfully by using backpropagation algorithm which calculates recursively the partial derivative through two fazes (backward faze and forward faze). Both fazes are applied sequencely to all samples from the training set. The whole training set processing is called an "epoch". A number of epochs should be done in order to train the network as long as the satisfied accuracy of network output is accomplished. There are modifications of this algorithm with higher convergence order. The most important of them are conjugate gradient and quasi-Newton methods.

III. RELATIONS DESCRIBING TRANSISTOR NOISE MODEL

The equivalent circuit of MESFET noise model is shown in Fig.2 (the intrinsic circuit is framed with a broken line). The noise contributions of the resistance R_{gs} and conductance G_{ds} are modeled by voltage noise source e_{gs} and current noise source i_{ds} , respectively, which are in correlation. The equivalent temperatures T_g and T_d are assigned to the voltage source e_{gs} and current source i_{ds} , respectively, while the correlation between them is presented by the complex equivalent temperature $T_c = |T_c| e^{j\omega\tau_c}$. The corresponding relations are:

$$\langle |e_{gs}|^2 \rangle = 4kT_g R_{gs} B, \tag{5}$$

$$\langle |i_{ds}|^2 \rangle = 4kT_d G_{ds} B, \tag{6}$$

$$\langle e_{gs} i_{ds}^* \rangle = \rho_c \sqrt{\langle |e_{gs}|^2 \rangle \langle |i_{ds}|^2 \rangle} = 4kT_c B, \tag{7}$$

where k is Boltzmann constant, B is incremental bandwidth and $\langle \rangle$ represents time average.

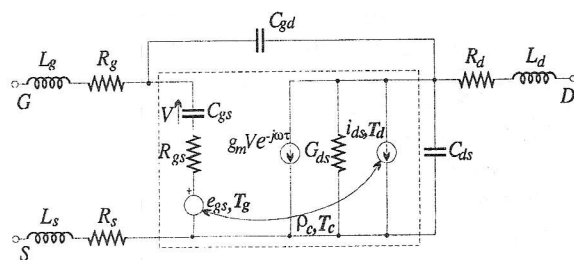


Fig.2. Equivalent transistor circuit

Intrinsic transistor circuit noise parameters can be expressed as function of equivalent circuit elements, three equivalent temperatures and frequency as follows [2]:

$$F_{min} = 10 \log \left\{ 1 - j \frac{2Q_3}{g_m T_o} \left[R_{gs} T_g G_{ds} T_d - \frac{R_{gs}^2 T_d^2 G_{ds}^2 Q_3^2}{g_m^2} \right. \right. \\ \left. \left. - \left(|T_c| P_1 \right)^2 - j \frac{2R_{gs} G_{ds} T_d |T_c| P_2 Q_3}{g_m} \right]^{1/2} \right. \\ \left. - \frac{2Q_3^2 R_{gs} T_d G_{ds}}{g_m^2 T_o} - j \frac{2|T_c| P_2 Q_3}{g_m T_o} \right\}, \quad (8)$$

$$R_n = \frac{T_g}{T_o} R_{gs} + \frac{G_{ds} T_d Q_1 Q_2}{g_m T_o} + 2 \frac{|T_c|}{g_m T_o} (P_1 - j R_{gs} P_2 Q_3), \quad (9)$$

$$X_{opt} = -\frac{1}{jQ_3} + j \frac{g_m |T_c| P_1}{G_{ds} T_d Q_3}, \quad (10)$$

$$R_{opt} = \sqrt{R_{gs}^2 - \frac{g_m^2}{Q_3^2} \left[\frac{R_{gs} T_g}{G_{ds} T_d} - \left(\frac{|T_c| P_1}{G_{ds} T_d} \right)^2 \right] + j 2 \frac{g_m R_{gs} |T_c| P_2}{G_{ds} T_d Q_3}}, \quad (11)$$

$$\Gamma_{opt} = \frac{R_{opt} + jX_{opt} - Z_o}{R_{opt} - jX_{opt} + Z_o}, \quad (12)$$

where: $T_o = 290$ K, $Z_o = 50$ Ω ,

$$Q_1 = 1 + j\omega C_{gs} R_{gs}, \quad Q_2 = 1 - j\omega C_{gs} R_{gs}, \\ Q_3 = j\omega C_{gs}, \quad P_1 = \cos[\omega(\tau_c - \tau)] \quad \text{and} \\ P_2 = \sin[\omega(\tau_c - \tau)].$$

IV. MESFET NOISE MODELING BY USING NEURAL NETWORK

With the aim to realize a neural model, MLP3 conception (with three layers i.e. one hidden layer) and MLP4 conception (with four layers i.e. two hidden layers) were used. In neural network training on the given set of samples, we have used quasi-Newton and conjugate gradient methods with the aim to reduce an output error. Models were trained on the sets with 500, 1000 and 1600 training samples and are denoted in the following way:

- Mm-3-nP-model of MLP3 structure with n neurons in hidden layer, trained on the set of m samples, by method P.

- Mm-4-n-kP-model of MLP4 structure with n neurons in the first hidden layer and k neurons in the second hidden layer (observed from input to output) trained by method P on the set of m samples.

Neural models that correspond to noise representation described above have ten inputs and four outputs. The inputs are intrinsic equivalent circuit elements (C_{gs} (pF), R_{gs} (Ω), g_m (mS), τ (ps), G_{ds} (S)), equivalent temperatures (T_g (K), T_d (K), $|T_c|$ (K), τ_c (ps)) and frequency f (GHz). Model

outputs are noise parameters: minimum noise figure F_{min} , normalized equivalent noise resistance r_n , magnitude and angle of optimum reflection coefficient Γ_{opt}

As noise parameter measurement in microwave frequency range requires expensive and complex equipment, and noise parameter data available in manufacturer's catalogue are not often quite enough and appropriated for training purposes, this process is accomplished by data obtained by FORTRAN program developed on noise parameter mathematical model (equations (8)-(12)).

Equivalent circuit parameter values used for training data generation are from ranges typical for MESFET transistors [6].

After training process, the models were tested for NEC transistor N71000A. For this transistor there are manufacturer's S-parameter data in the frequency range (1.5-26.5) GHz and noise parameter data at several discrete frequencies in the range (2-18) GHz. The elements of the MESFET intrinsic equivalent circuit as well as equivalent temperatures are extracted by using standard circuit simulator Libra, in the way given in [2]. The following values are obtained:

$$C_{gs} = 0.28 \text{ pF}, \quad R_{gs} = 3.1 \Omega, \quad g_m = 0.05 \text{ S}, \quad \tau = 3.34 \text{ ps}, \\ G_{ds} = 0.004 \text{ S}, \quad T_g = 154 \text{ K}, \quad T_d = 2019 \text{ K}, \quad |T_c| = 37.2 \text{ K}, \\ \tau_c = 11.3 \text{ ps},$$

In this way obtained equivalent noise model parameters are used as inputs in neural network for test process. The average error (AE) and the worst case error (WCE) between neural model outputs and referent (measured) data in general and for each noise parameter are given in Table I. Shown results refer to the best model of MLP3 structure and for two of the best models of MLP4 structure for each model group trained by the same sample number. Thus, on the basis of minimal error criteria, it can be concluded that the best modeling of MESFET N71000A transistor noise parameter is achieved by model M1600-4-15-15Q.

The results for MESFET noise parameters referring to whole equivalent transistor circuit including parasitic effects are represented in Fig.3. The characteristics obtained by using MLP4 neural network (denoted by NN4) are compared with the ones assigned to the measured data (MEAS). It should be pointed out that a very well agreement between these two curves is accomplished for all noise parameters in whole frequency range.

V. CONCLUSION

Noise parameter modeling of MESFET transistor is performed by using MLP3 and MLP4 structure of neural network with different number of neurons in hidden layers. Neural models are trained on three training data sets by using quasi-Newton

and conjugate gradient methods. The obtained results show that better agreement between modeled and referent (measured) data is accomplished by using MLP4 models than by using MLP3 models (Table I.). Also, it can be concluded that models trained with higher number of samples (for example

1600) give better results than the ones trained on 500 and 1000 samples and that quasi-Newton training method gives the best results for both MLP structures. Thus, the best modeling is achieved by using M1600-4-15-15q model.

TABLE I. TESTING RESULTS

Model	General		Fmin		Rn		Γ_{opt}		Ang (Γ_{opt})	
	AE [%]	WCE [%]	AE [%]	WCE [%]	AE [%]	WCE [%]	AE [%]	WCE [%]	AE [%]	WCE [%]
M500-3-15Q	8.742	29.473	4.844	8.318	5.678	6.911	22.125	29.473	2.318	3.991
M500-4-15-10Q	2.260	6.544	2.292	5.217	1.589	2.457	2.351	4.483	2.814	6.544
M500-4-15-15Q	5.314	13.101	1.706	5.559	2.289	4.270	6.127	8.958	11.134	13.100
M1000-3-14-Q	2.083	7.593	1.251	2.438	0.410	0.951	4.046	7.593	2.625	3.508
M1000-4-10-10Q	1.763	5.112	1.219	2.188	0.778	1.018	3.226	5.112	1.828	3.452
M1000-4-10-12Q	1.567	5.991	1.015	2.290	0.985	5.734	3.619	5.991	0.642	1.635
M1600-3-12Q	1.170	4.655	0.881	2.103	0.342	1.007	2.366	4.655	1.093	1.925
M1600-4-15-15Q	0.827	3.068	0.373	0.962	0.602	0.885	1.578	3.068	0.755	2.031
M1600-4-18-15Q	0.921	3.455	0.605	0.959	0.458	1.326	1.954	3.455	0.667	1.713

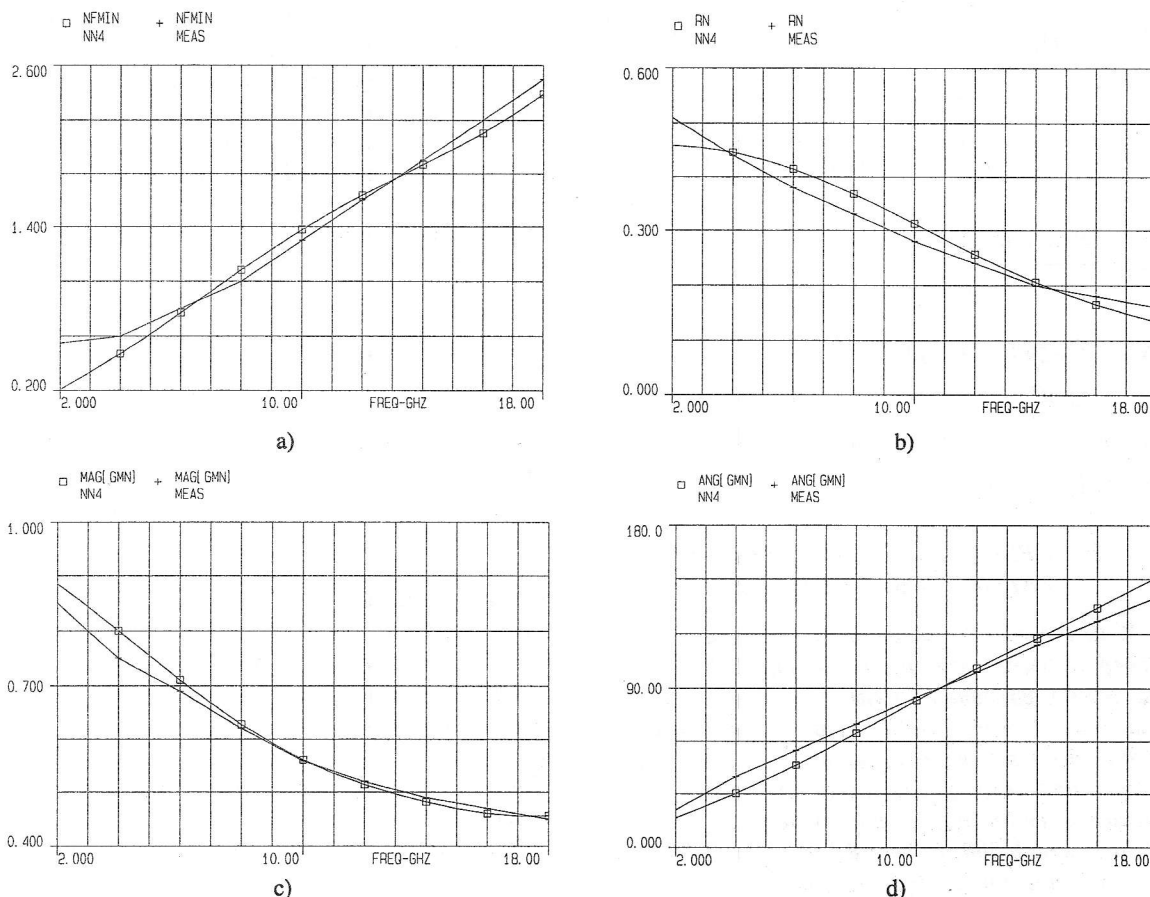


Fig. 3. Noise parameters: a) Minimum noise figure; b) Normalized noise resistance; c) Magnitude and d) Angle of optimum reflection coefficient

BIBLIOGRAPHY

- [1] F. Wang, Q.J. Zhang, "Knowledge-Based Neural Models for Microwave Design", *IEEE Trans., Microwave Theory Tech.*, Vol. 45, No-12, pp-2333-2343, December 1997.
- [2] V. Marković, B. Milovanović, N. Maleš-Ilić, "MESFET Noise Modeling Based on Three Equivalent Temperatures", *Proceedings of the*
- [3] M.W. Pospieszalski, "Modeling of Noise Parameters of MESFET's and MODFET's and Their Frequency and Temperature Dependence", *Conference EUMC'97*, pp.966-971, Jerusalem, Israel, September 1997.
- [4] *IEEE Trans. Microwave Theory Tech.*, vol.MTT-37, pp. 1340-1350, Sept. 1989.
- [5] "Touchstone and Libra Users Manual", EEsof, Inc. 1990.
- [6] S. Milenković, "Veštačke neuronske mreže", *Zaduzbina Andrejević*, Beograd, 1997.
- [7] P. H. Ladbrooke, "MMIC Design: GaAs FET-s and HEMT-s", *Artech House*, Ma, U.S.A., 1989

MESFET NOISE MODELING BASED ON NOISE WAVE TEMPERATURES

Olivera Pronić, Nataša Maleš-Ilić

Faculty of Electronic Engineering, University of Niš, Yugoslavia

Abstract - A simple procedure for extraction the intrinsic noise wave temperatures in the wave representations of microwave transistors is presented in this paper. A set of equation describing the noise parameters as the function of three equivalent noise temperatures is implemented within the circuit simulator Libra. After that, the wave noise model is defined as new user-defined element of program Libra library. Good agreement between modeled and measured noise parameters is observed.

INTRODUCTION

Small-signal low noise microwave transistors are usually represented by their equivalent circuits which include noise sources. There are several different representations of a noisy two-port circuit, [1]. Each representation is characterised by the existence of a noiseless two-port network and two additional correlated noise sources. Noise is typically characterised using combinations of equivalent voltage and current sources.

A significant contribution to the MESFET noise modeling was made by Pospieszalski, [2]. The model he presented is based on H representation of MESFET intrinsic circuit with two uncorrelated noise sources. On the basis of that approach, the authors of this paper developed a CAD oriented procedure for MESFET, HEMT and DUAL-GATE MESFET noise parameters prediction [3], [4]. We also extended the Pospieszalski's noise model by introducing the correlation between noise sources, [5].

For high frequency circuit applications, however, a wave interpretation of noise seems more appropriate. Wedge and Rutledge showed, [6], that wave approach can be useful for noise modeling and measurement of microwave FETs. They derived the expressions for noise wave parameters of device intrinsic circuit as the functions of equivalent circuit elements, equivalent gate and drain temperature. Based on that, an extraction procedure for noise wave sources in MESFET wave representations was suggested in [7].

The aim of this paper is to present a new simple procedure for noise modeling of microwave transistors by using three noise wave temperatures. The complete procedure is CAD-oriented and can be implemented in the commercial microwave circuit simulator Libra [8]. However, with the aim to avoid the repetition of this routine whenever a new transistor should be analyzed, we applied a procedure for creating new Libra library three-port element for

MESFET signal and noise simulations, that can be used like all other standard Libra library elements by using only one instruction. This procedure was performed by using special program Libra support for defining new user's elements named Libra Sr. [9].

NOISE WAVE REPRESENTATIONS OF TWO-PORT CIRCUITS

A linear noisy two-port network can be represented by noise waves and scattering parameters as shown schematically in Fig. 1. a). Noise waves b_{n1} and b_{n2} contribute to the scattered waves such that the wave variables and scattering parameters satisfy the following equation

$$\begin{bmatrix} b_1 \\ b_2 \end{bmatrix} = \begin{bmatrix} S_{11} & S_{12} \\ S_{21} & S_{22} \end{bmatrix} \begin{bmatrix} a_1 \\ a_2 \end{bmatrix} + \begin{bmatrix} b_{n1} \\ b_{n2} \end{bmatrix}. \quad (1)$$

The other wave representation of a noisy two-port using two input noise wave sources a_n and b_n and transfer scattering parameters $[T]$ is shown in Fig. 1. b). The matrix equation for this representation is

$$\begin{bmatrix} a_1 \\ b_1 \end{bmatrix} = \begin{bmatrix} T_{11} & T_{12} \\ T_{21} & T_{22} \end{bmatrix} \begin{bmatrix} b_2 \\ a_2 \end{bmatrix} + \begin{bmatrix} a_n \\ b_n \end{bmatrix}. \quad (2)$$

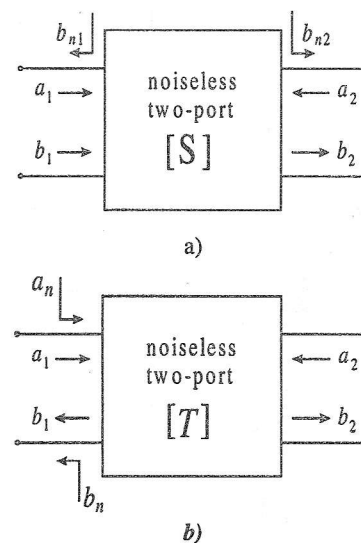


Figure 1. The schematic representation of a noisy two-port: a) using scattering parameters and noise waves, b) using transfer scattering parameters and noise waves

The elements of noise source vector generally are correlated and characterised by correlation matrices C_S and C_T , respectively, given by

$$C_S = \begin{bmatrix} \langle |b_{n1}|^2 \rangle & \langle b_{n1} b_{n2}^* \rangle \\ \langle b_{n2} b_{n1}^* \rangle & \langle |b_{n2}|^2 \rangle \end{bmatrix}, \quad (3)$$

and

$$C_T = \begin{bmatrix} \langle |a_n|^2 \rangle & \langle -a_n b_n^* \rangle \\ \langle -b_n a_n^* \rangle & \langle |b_n|^2 \rangle \end{bmatrix} \quad (4)$$

where brackets $\langle \rangle$ indicate time average of the quantity inside and * indicates complex conjugation.

However, for noise temperature calculations, we concluded that it is most usefully to express the correlation matrix C_T in the following form, [10],

$$C_T = k\Delta f \begin{bmatrix} T_a & T_c^* \\ T_c & T_b \end{bmatrix}, \quad (5)$$

where k is Boltzmann's constant and Δf is the frequency interval of interest. In this way the noise performance of a two-port network is completely characterised by two real temperatures T_a and T_b and a complex correlation temperature $T_c = |T_c| e^{j\omega\tau_c} = |T_c| e^{j\phi_c}$.

The noise wave correlation matrix C_S , describing the circuit in Fig. 1. a), can be easily expressed as a function of C_T matrix, [1].

EXTRACTION OF NOISE WAVE TEMPERATURES

A typical equivalent circuit of MESFET and HEMT chip is considered, as it is shown in Fig. 2. The intrinsic part of the circuit is denoted by the broken line.

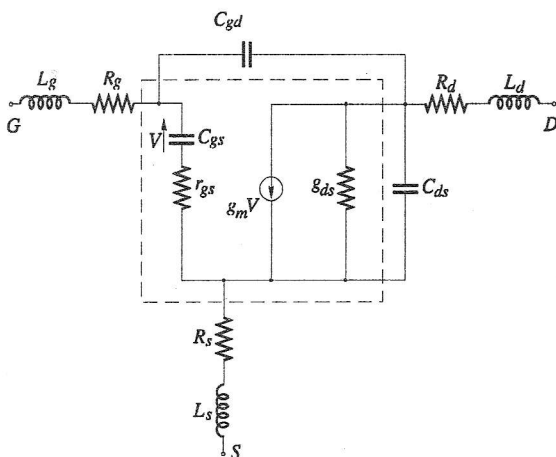


Figure 2. Equivalent circuit of MESFET and HEMT chip

Noise wave temperatures can be expressed in term of intrinsic circuit noise parameters - minimum noise

figure F_{min} , noise resistance R_n and optimum reflection coefficient $\Gamma_{opt} = |\Gamma_{opt}| e^{j\phi_{opt}}$, [11], as

$$T_a = T_0 (F_{min} - 1) + \frac{4R_n T_0 |\Gamma_{opt}|^2}{Z_0 |1 + \Gamma_{opt}|^2}, \quad (6)$$

$$T_b = \frac{4R_n T_0}{Z_0 |1 + \Gamma_{opt}|^2} - T_0 (F_{min} - 1), \quad (7)$$

$$T_c = - \frac{4R_n T_0 |\Gamma_{opt}| e^{-j\phi_{opt}}}{Z_0 |1 + \Gamma_{opt}|^2}, \quad (8)$$

where Z_0 is the normalisation impedance (50Ω) and T_0 is standard reference temperature (290K).

For CAD purposes it is most convenient to use noise parameters data measured at a limited number of frequencies, that can be found in manufacturer data books.

The intrinsic circuit noise parameters, needed for the equivalent noise temperatures calculation, can be obtained from the noise parameter data for the whole transistor in chip or packaged form. For this purpose, a de-embedding process is done by Libra, by adding parasitic elements with negative values and in reverse order to the device two-port circuit. The values of the MESFET equivalent circuit elements are extracted from the S parameter data. Noise analysis applied by Libra in this way, gives the noise parameters of transistor intrinsic circuit.

As example, the results concerning the noise wave temperatures extraction for NEC MESFET type N71000A will be presented. Element values obtained for the equivalent circuit shown in Fig. 2 are: $R_g=0.24\Omega$, $L_g=0.158nH$, $R_d=2.20\Omega$, $L_d=0.131nH$, $R_s=4.13\Omega$, $L_s=0.036nH$, $g_m=48mS$, $C_{gd}=0.046pF$, $r_{gs}=2.91\Omega$, $C_{gs}=0.311pF$, $r_{ds}=245\Omega$, $C_{ds}=0.097pF$.

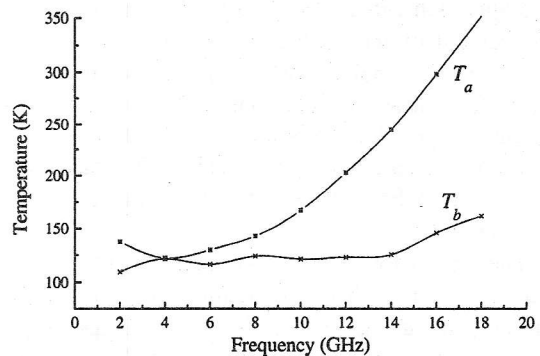


Figure 3. Noise wave temperatures T_a and T_b versus frequency

Noise wave temperatures T_a and T_b versus frequency are shown in Fig. 3. Magnitude and angle of correlation temperature T_c are shown in Fig. 4.

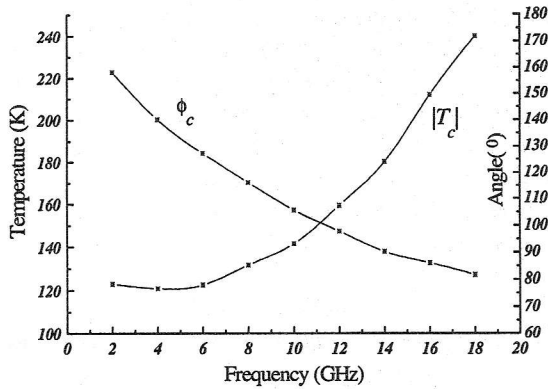


Figure 4. Magnitude and angle of correlation temperature T_c versus frequency

TRANSISTOR NOISE MODELING USING NOISE WAVE TEMPERATURES

Using the relationships between noise wave temperatures and noise parameters, a procedure for CAD prediction of MESFET noise parameters behaviour can be implemented within the circuit simulator Libra. For this purpose, inverse relations to Eqs. (6) - (8) are found as

$$|\Gamma_{opt}| = \frac{T_a + T_b}{2|T_c|} - \sqrt{\left(\frac{T_a + T_b}{2|T_c|}\right)^2 - 1} \tag{9}$$

$$\phi_{opt} = \pi - \phi_c \tag{10}$$

$$R_n = Z_0 \frac{|T_c|}{4T_0|\Gamma_{opt}|} \left[1 + 2|\Gamma_{opt}| \cos \phi_{opt} + |\Gamma_{opt}|^2 \right] \tag{11}$$

$$F_{min} = 1 + \frac{T_a - T_b}{2T_0} + \frac{1}{2T_0} \sqrt{(T_a + T_b)^2 - 4|T_c|^2} \tag{12}$$

It is obvious that intrinsic noise parameters are functions only of noise wave temperatures. So, these are the simpler expressions than Pospieszalski's one, where noise parameters are defined as functions of equivalent circuit elements as well as noise temperatures.

The set of equations (9) - (12) is programmed in Libra using "equation" capability of circuit simulator. After that, the remaining parasitic transistor elements were connected and a simple optimisation procedure is applied to extract frequency independent equivalent

noise wave temperatures. Obtained values for the transistor N71000A are: $T_a=120,6K$, $T_b=84,5K$, $|T_c|=127,4K$, $\tau_c=14,1ps$. By using these values, four noise parameters: minimum noise figure, noise resistance, magnitude and angle of optimum reflection coefficient for the whole transistor are obtained. The noise parameter characteristics are shown in Figs. 5 - 8. The curves obtained by using the proposed model are denoted by MOD1. The referent curves (REF) are based on the data measured by manufacturer.

The comparison between curves in Figs. 5 - 8. has shown a very good agreement between measured and modeled noise parameters. Several other transistors have been analysed and modeled with similar results.

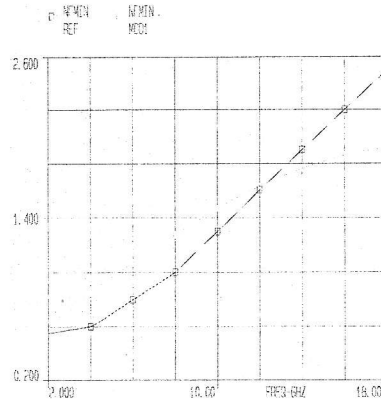


Figure 5. Minimum noise figure

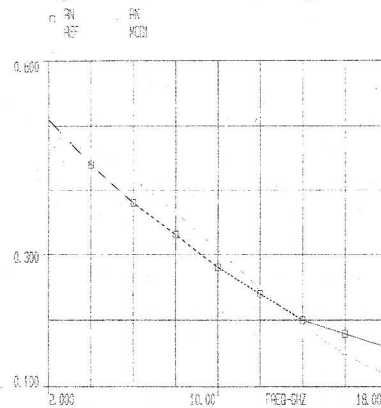


Figure 6. Noise resistance

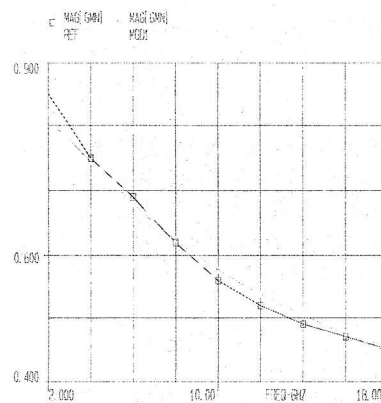


Figure 7. Magnitude of optimum reflection coefficient

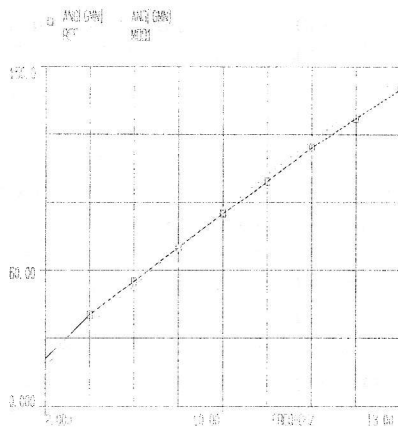


Figure 8. Angle of optimum reflection coefficient

PROCEDURE FOR DEFINING NEW ELEMENTS

The program Libra Senior (Libra Sr.) was used for defining new element. For this purpose, it is necessary to modify Userproc.c file by an appropriated user algorithm.

A procedure for defining element for intrinsic circuit transistor noise modeling based on previously described wave model can be present through few steps: Firstly, S-parameters of an intrinsic equivalent circuit observed as three-port element should be defined. After that, four noise parameters are defined according to corresponding relationships (9)-(12). The noise parameters are joined to a three port element defined by S parameters using function

active-noise (fmin, gammag, gamang, rn, rnorm), where *fmin* is minimum noise figure in dB, *gammag* and *gamang* are magnitude and angle of optimum reflection coefficient, *rn* is normalized equivalent noise resistance, *rnorm* is normalization resistance. After algorithm incorporation in Userproc.c file it is necessary to compile a modified file in an object code and to link module with Libra. The both processes are doing by the instruction MAKELBRA XXX, where XXX presents an arbitrary new three character extension of Userproc.c file.

A new program Libra code is on current folder and can be called by the following instruction: LBRAXXX.

In this way defined three-port element represents an element of program Libra library and can be included within CKT block of program Libra by the following instruction:

```
U3PA 1 2 3 D1^Cgs D2^Rgs D3^gm D4^τ
D5^Gds D6^Ta D7^Tb D8^Tc 9^tc.
```

The results obtained by using the user defined element are in completely agreement with previously mentioned ones.

CONCLUSION

A simple extraction procedure for intrinsic noise wave temperatures in the wave representation of microwave transistors is presented. Noise wave

temperatures for MESFET N71000A are calculated and shown graphically as a function of frequency. A set of equation describing the noise parameters as the function of three equivalent noise temperatures is implemented within the circuit simulator Libra. The undoubted benefit of created new Libra library three-port elements for MESFET signal and noise simulations is that one can be used like all other standard program Libra library elements by using only one instruction. Noise parameter characteristics obtained by proposed modeling procedure are compared to measured ones and quite good agreement is observed.

REFERENCES

- [1] J. A. Dobrowolski, *Introduction to Computer Methods for Microwave Circuit Analysis and Design*, London, Artech House, 1991.
- [2] M. W. Pospieszalski, "Modeling of noise parameters of MESFET's and MODFET's and their frequency and temperature dependence", *IEEE Trans. Microwave Theory Tech.*, vol.MTT-37, pp. 1340-1350, September 1989.
- [3] V. Marković, B. Milovanović, O. Pronić, N. Maleš-Ilić, "Efficient Extraction of Intrinsic Transistor Noise Temperatures by Standard Microwave Software Tools", *Conference Proceedings ANTEM'96*, pp. 501-504, Montreal, Canada, 1996.
- [4] V. Marković, B. Milovanović and N. Maleš, "Noise modeling of dual-gate MESFET", *Electronic Letters*, vol.33, No.9, pp. 820-821, April 1997.
- [5] V. Marković, B. Milovanović, O. Pronić, N. Maleš-Ilić, "MESFET noise modeling by using explicit relations for three equivalent temperatures", *Conference Proceedings MELECON'98*, pp. 311-315, Tel-Aviv, Israel, 1998.
- [6] S. W. Wedge and D.B.Rutledge, "Wave Techniques for noise modeling and measurement", *IEEE Trans. Microwave Theory Tech.*, vol.MTT-40, pp. 2004-2012, November 1992.
- [7] V. Marković, B. Milovanović, O. Pronić, M. Ilić, "Extraction of Noise Wave Sources in MESFET wave representations", *Int. Conf. on Microwave and Millimeter Wave Technology*, pp. 108-111, Beijing, China, 1998.
- [8] *Touchstone and Libra Users Manual*, EEsof, Inc. 1990.
- [9] *Touchstone Sr. and Libra Sr., Users Guide*, Version 2.1, 1989.
- [10] R. P. Meys, "A wave approach to the noise properties of linear microwave devices", *IEEE Trans. Microwave Theory Tech.*, vol.MTT-26, pp. 34-37, January 1978.
- [11] T. O. Grosch, L. A. Carpenter, "Two-Port to Three-Port Noise-Wave Transformation for CAD Applications", *IEEE Trans. Microwave Theory Tech.*, vol.MTT-41, pp. 1543-1548, September 1993.

NEW GENERATION OF MILLIMETER-WAVE COMMUNICATION SYSTEMS

Aleksandar Nešić¹, Veselin Branković², Ivana Radnović¹

¹Institut IMTEL, Beograd

²Telecommunication Research & Development Europe (TRDE); SONY International GmbH, Germany

Abstract The vision of future high data rate in-door communication systems is presented. The key technological requirements and possible solutions for RF technologies are outlined. Integration of front-end with antenna in the mm-wave range and incorporation of the dual frequency operation may provide a major step toward a low cost solution. The key technology features are verified by prototyping, showing encouraging results.

I INTRODUCTION

The main goals in the development of new generation mobile communication systems operating in 60 GHz range with capacities up to 150 Mb/s are, among others, increase of capacity and great number of specific applications such as high resolution image transfer in medical, industrial and economic buildings, as well as in institutions dealing with informatics. One of the very important objectives is also compatibility with existing 3rd generation mobile communication systems.

Concepts, solutions and standards that are considered are:

- Internet Protocol (IP)
- Universal Mobile Telecommunication System (UMTS)
- Asynchronous Transfer Mode (ATM)
- Integrated Services Digital Network (ISDN)

These new systems will provide a broadband access to applications which will appear in the result of the converging business areas Telecommunications, Information technology, and mass MEdia – the so called TIME-Markets (see Figure 1). Future access technologies must support mobility – which is a clear indication for the growing importance of wireless systems (see Figure 2).

II CHOICE OF THE FREQUENCY RANGE

At the moment, mobile communication systems of the 2nd (GSM) and 3rd (UMTS - Universal Mobile Telecommunication System) generations are in use and they are not compatible. New wireless systems are considered in various world projects: RACE (European investigation project within which the UMTS is created) and ACTS (Advanced Communications Technologies and Services) which is the most remarkable European project in this field at the moment. Future systems conceived within these projects are:

- RACE MBS (Mobile Broadband System),
- ACTS MEDIAN (system at 60 GHz),
- ACTS SAMBA (High-data Communication System at 40 i 60 GHz),
- ANSIBLE (system that is being investigated and developed at the moment).

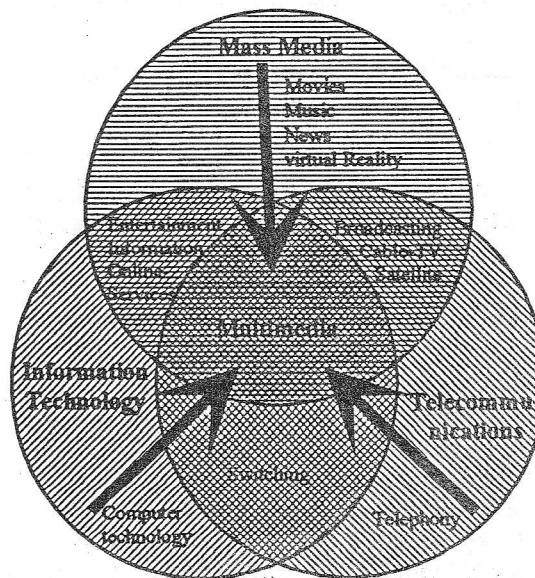


Figure 1. Convergence of the TIME-markets.

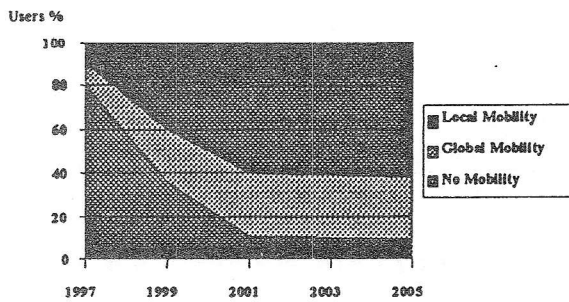


Figure 2 Requirement for mobility support.

On the basis of previously mentioned considerations, key requirements for the ANSIBLE system are defined:

- Enhancement of the existing broadband wireless LAN concepts in 60 GHz range,
- Enabling of high data rates – up to 150 Mb/s,
- Compatibility with a new HIPERLAN 2 system operating in 5 GHz range, e.g. fast transition from 60 GHz system to a 5 GHz system and reverse.
- Wide frequency range in order to enable high density of users and therefore services from a few kb/s to 150 Mb/s,
- Peer-to-peer mode (also called direct mode) – terminals close enough to each other could communicate directly and not via the basestation that benefits in more efficient use of the system resources.
- Acceptable dimensions of terminal devices,
- Low-cost.

III MAIN ACTIVITIES DURING THE INVESTIGATION AND DEVELOPMENT

- Theoretical investigations,
- Simulation of the functional blocks and sub-systems,
- Design, prototyping and measurements of the demonstration system operating at lower frequency (24 GHz),
- Design, prototyping and measurements of different key sub-parts of 60 GHz system,
- Integration of 60 GHz front-ends (with new MMIC components) with antennas.

The key problems in the theoretical investigation and design of a MW part are antennas of different types that have to be used in the ANSIBLE system [1], low noise amplifiers and high power amplifiers.

Expected characteristics of the ANSIBLE system, as well as those of the demonstration model are shown in the following table, Fig. 3, [2].

	System	Demonstrator
Technology	OFDM/TDMA/ATDD	COFDM single link
Radio frequency	5/ 24/ 60 GHz	5/ 24 GHz
Channel BW	15 - 30 MHz	20 MHz
User data rate	up to 155 Mbit/s	up to 40 Mbit/s
SC modulation	(D)(4,8,16)PSK, 16 QAM	D4PSK, D8PSK (D16PSK)
FFT length	64 (128)	64 - 512
Code rate	1/2, 2/3	1/2, 2/3

Figure 3 Characteristics of the ANSIBLE system and of the demonstration model.

IV ANTENNAS IN THE ANSIBLE SYSTEM IN 5 GHz, 24 GHz AND 60 GHz RANGES

The following types of antennas integrated with convenient microwave circuits are planned to be used:

- SMART antennas with digital beam-forming,,
- Space diversity antennas,
- Antennas with circular polarization,
- Antennas with circular polarization and conical beam,
- High-gain antennas for 24 GHz and 60 GHz ranges.

V ARRAY FOR SMART ANTENNA SYSTEM

SMART antenna system enables:

- Automatic adjustment of direction and shape of the antenna pattern,
- Tracking of receiving signals,
- Suppression of co-channel interference.

In the presented version of the array for SMART antenna system, 8 printed dipoles operating on third resonance are used and each of them is integrated with preamplifier and a mixer. After mixing, signal is being processed in the baseband in order to form desired antenna beam, [3]. The array is shown in Fig. 4.

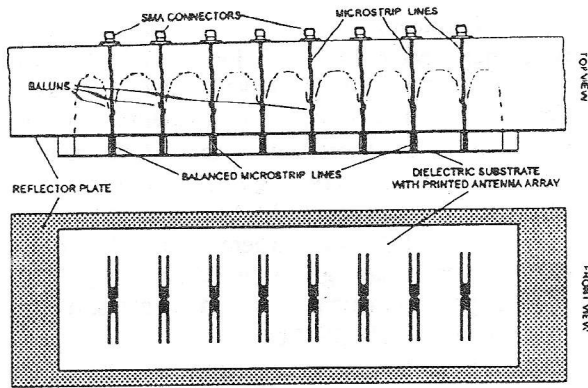


Figure 4 Array of 8 printed dipoles operating on third resonance.

VI SPACE DIVERSITY ANTENNA

This antenna is used for the 5-6 GHz range in cases when there is no line of sight and when direction of the incoming signal is uncertain.

Antenna is cube-shaped with 6cm sides. On the four of them, there are triangular slots (complementary with bow-tie dipoles) behind which is a "corner" reflector plate. Bandwidth of this antenna is relatively wide and its radiation pattern is very suitable for above-mentioned application. Drawing of the antenna is given in Fig.5.

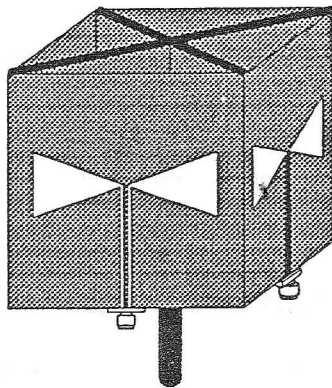


Figure 5 Space diversity antenna.

VII ANTENNAS WITH CIRCULAR POLARIZATION

Antennas with circular polarization are practically unavoidable in mobile communications due to the fact that there is no need for the antenna orientation. Beside this, the special advantage of the circularly polarized antennas is their feature of additional physical attenuation of reflected waves (due to polarization direction changing) which makes propagation channel much better and the overall system more resistant in the case of multipath propagation.

Printed antenna realized in the IMTEL Institute has much wider bandwidth, better axial ratio and lesser VSWR comparing to conventional printed antennas with circular polarization, [4].

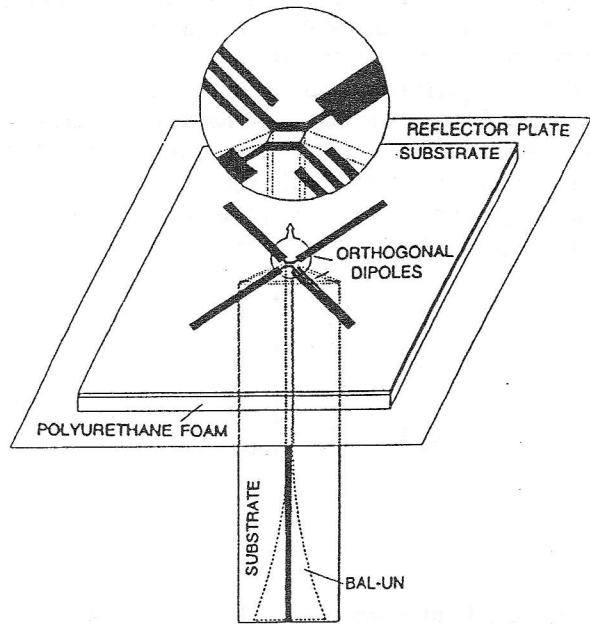


Figure 6 Two orthogonal dipoles fed by a symmetrical microstrip line.

VIII ANTENNAS WITH CIRCULAR POLARIZATION AND CONICAL BEAM

These antennas will be used as base station antennas for in-door applications in order to achieve approximately uniform field in a whole room. Diagram that shows principle of use and radiation pattern of the antenna with circular polarization and conical beam is given in Fig. 7, [5].

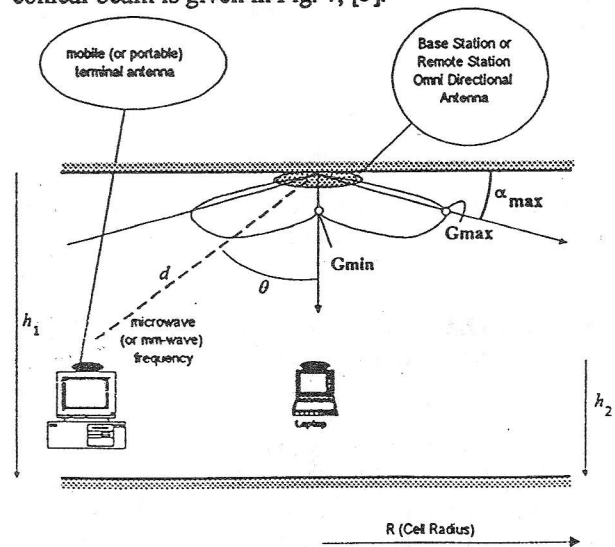


Figure 7 In-door application scenario for the antenna with circular polarization and conical beam.

IX HIGH-GAIN ANTENNAS FOR 24 GHz AND 60 GHz RANGES

These antennas will be used for terminal devices, mostly in 60 GHz range. Novel and inventive solutions are implemented and obtained characteristics are much better than those of known printed antennas operating in millimeter range, [6]. Main advantages are: extremely wide bandwidth, relatively low losses and miniature dimensions. Layouts of printed antennas for 60 GHz range with 64 and 256 radiating elements and with gains of 20 dBi and 25 dBi, respectively are shown in Figs. 8 and 9.

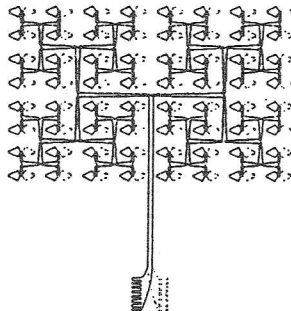


Figure 8 Printed array with 8x8 dipoles for 60 GHz range.

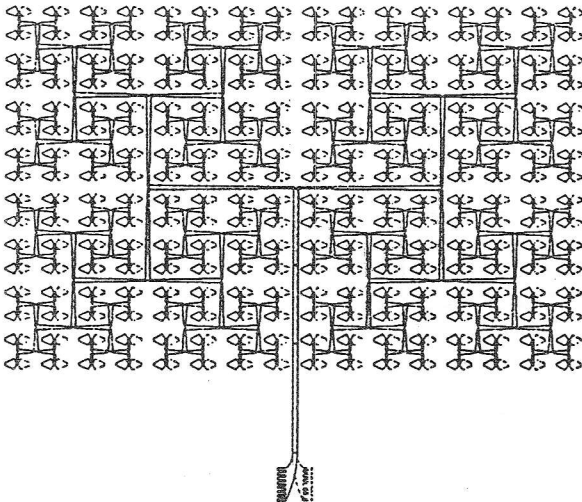


Figure 9 Printed array with 16x16 dipoles for 60 GHz range.

X REALIZATION OF THE DEMONSTRATION MODEL AT 5GHz AND 24GHz

The main requirement which have to fulfill future systems is to simultaneously exploit advantages of lower and higher frequency bands. In order to prove the system concept, dual-frequency demonstrator working at 24 GHz (ISM band) and 5

GHz (Non-licensed band) is being under development. Modulation solution is OFDM based, followed by features of adaptive change of spectral efficiency. Full integration of the antenna assembly with up/down converters from 5 to 24 GHz band is achieved in low cost way. High data rate system for in-door communication in MM-wave range is the main objective of the work, where presented up/down converters are playing an important role. The proposed system functions at two frequencies, having the priority at 24 GHz (ISM band).

The system tries at first to approach users in one room (one communication cell) at the higher frequency -24 GHz. This frequency may allow to use also sector antenna with medium gain (small size, also with tracking option) resulting in better communication channel. On the other hand, good propagation conditions allow higher spectrum efficiency and peak user data rates. At the same time, if the channel conditions are becoming worse or the user prefers that, lower frequency (non licensed 5 GHz band) is switched, allowing wall penetration of severe NLOS communication. This lower frequency is at the same time intermediate frequency of the RF system, so that the chip sets for 5 GHz system may also be used for 24 GHz system. The main idea standing behind proposed approach is that in both operational cases the same baseband hardware may be utilized. The channel bandwidth may remain the same.

Major blocks in the system are up converter (5GHz/24GHz) with integrated sector antenna in the transmitter and down converter (24GHz/5GHz) with integrated highly directed antenna, having relatively high gain, in the receiver. Block diagram of the communication system operating at 5 GHz and 24 GHz is shown in Fig. 10.

XI UP CONVERTER 5 GHz - 24 GHz

Signal at the first intermediate frequency is brought to the input of up converter (this signal is also used as a transmitting signal when the system operates in 5 GHz range). LO signal at 19 GHz is brought from a synthesizer whose oscillator has a dielectric resonator (DRO) at the working frequency in order to generate signal with low phase noise.

DRO is stabilized by a referent quartz oscillator (TCXO) through a phase locked loop (PLL). The same TCXO is also used as a reference in synthesizer in the 5 GHz range. Layout of the up converter 5/24 GHz is shown in Fig. 11. As it can be seen, the converter is realized on the same dielectric substrate with active printed antenna.

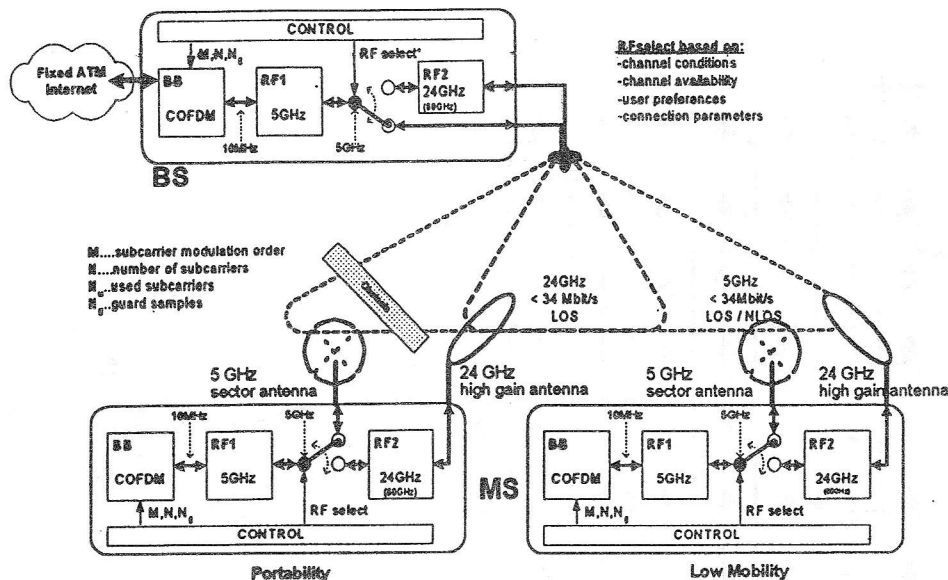


Figure 10 Block diagram of the communication system on 5 GHz and 24 GHz.

Incoming signal in 5 GHz range passes through a band-pass filter which attenuates LO- and converted RF-signal. Signal from the transmitter in 5 GHz range is led through a low-pass filter providing satisfactory attenuation of LO- and RF- signal (24 GHz) at the input.

Signal is then brought to a single-diode mixer with GaAs Schottky barrier diode (DMK 2790, Alpha Ind.) in flip-chip package. Diode biasing is performed so as to obtain optimal mixing performance i.e. to minimize conversion loss.

Outgoing signal is from the mixer led to a band-pass filter and to the first MMIC power amplifier (Alpha Ind. AA022P1-65). After that, it is being led to the second band-pass filter and another power amplifier (same as the first one) in whose output circuit there is an active printed antenna array. The array is realized with four wideband dipoles behind which is a reflector plate at the distance of

about 0.275λ . Between the antenna and the reflector plate, there is a polyurethane foam with $\epsilon_r=1.03$.

All units of the presented up converter with integrated antenna are realized on the same dielectric substrate – teflon-fiberglass ($\epsilon_r=2.17$, $h=0.254\text{mm}$), Fig. 11, [7].

XII DOWN CONVERTER 24 GHz – 5 GHz

Down converter is shown in Fig. 12. Printed wideband receiving antenna with 64 dipoles is integrated with converter. Signal from the antenna is brought to a band-pass filter (24 GHz) and afterwards to a low-noise MMIC amplifier (AA022N1-65, Alpha Ind.). The signal is then led to a rat-race balanced mixer with two GaAs Schottky barrier diodes in flip-chip package (DMK 2790, Alpha Ind.). Diodes are biased (through a chock) with 4.5 mA current in order to optimize mixing performance, Fig. 13, [7].

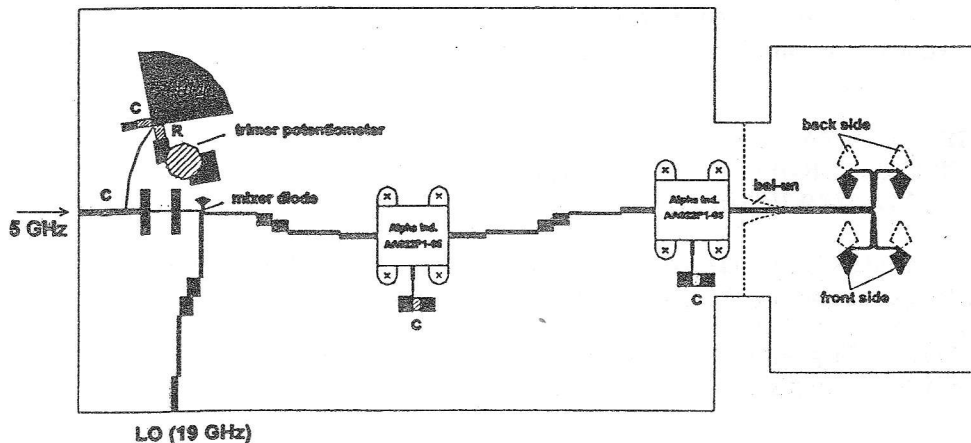


Figure 11 Layout of the up converter (5GHz/24GHz).

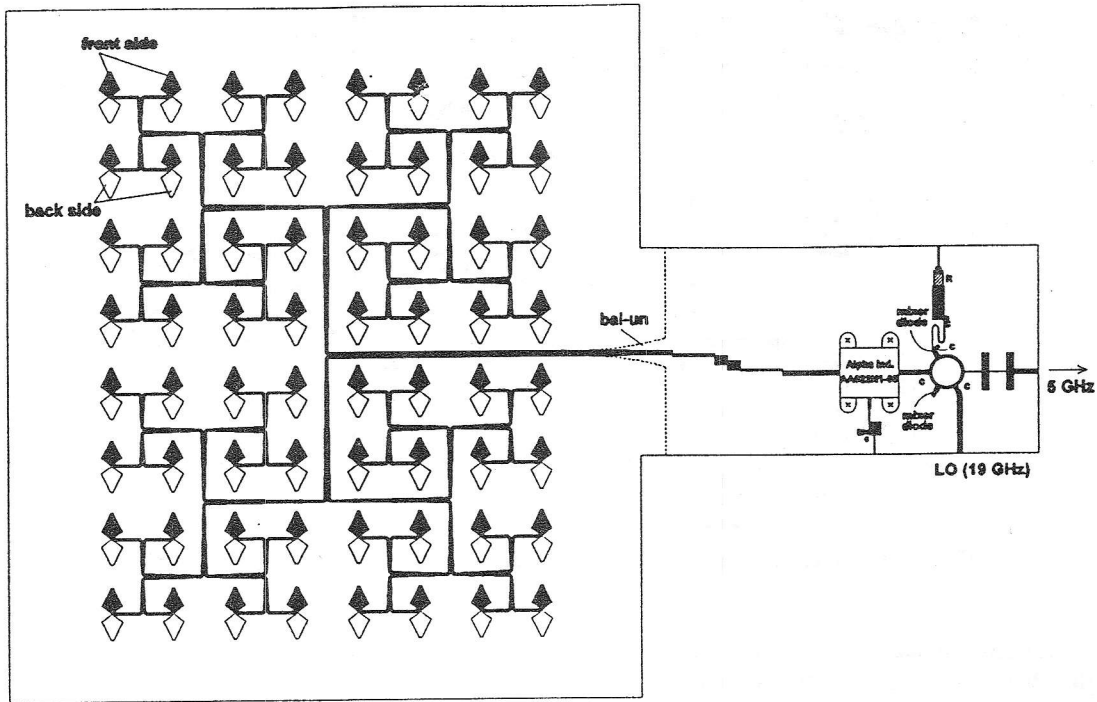


Figure 12 Layout of the down converter (24 GHz/5 GHz).

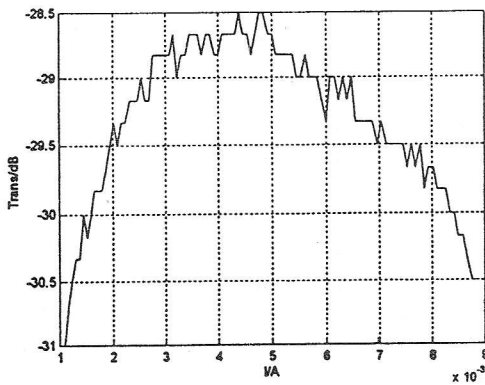


Figure 13 Influence of diode biasing on received IF power measured in the system with up/down converters.

XIII REALIZATION OF THE DEMONSTRATION MODEL AT 24 GHZ AND OBTAINED RESULTS

Both converters are realized on teflon-fiberglass dielectric substrate ($\epsilon_r=2.17$, $h=0.254\text{mm}$).

Realized up converter is shown on the photograph, Fig. 15. Diagram of the radiated power versus level of the incoming signal at 5 GHz is given in Fig. 14.

Total conversion gain is 20 dB. Dynamic range of more than 50 dB with practical ideal linearity is obtained. Saturation begins with output signal levels of about 26 dBm.

Photo of the down converter is given in Fig. 16. Total isotropic conversion gain of the down converter is 20 dB.

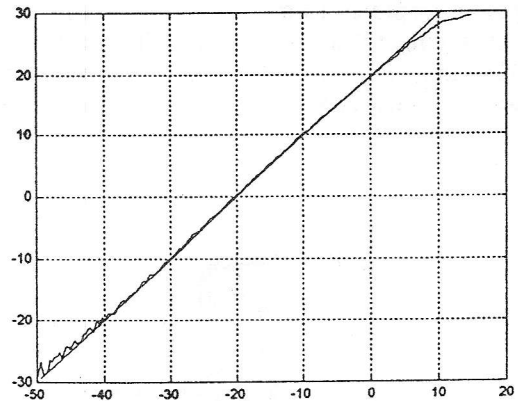


Figure 14 Tx radiated power measured with reference antenna at specified distance.

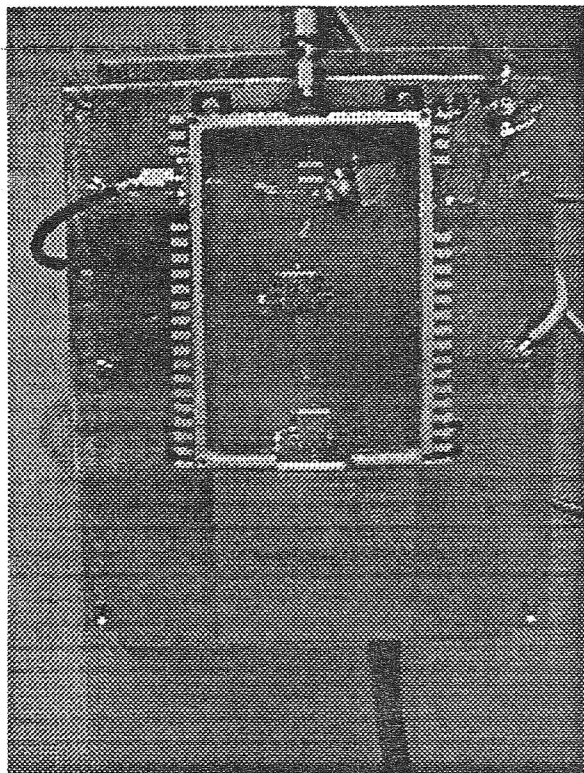


Figure 15 Photograph of the realized up converter.

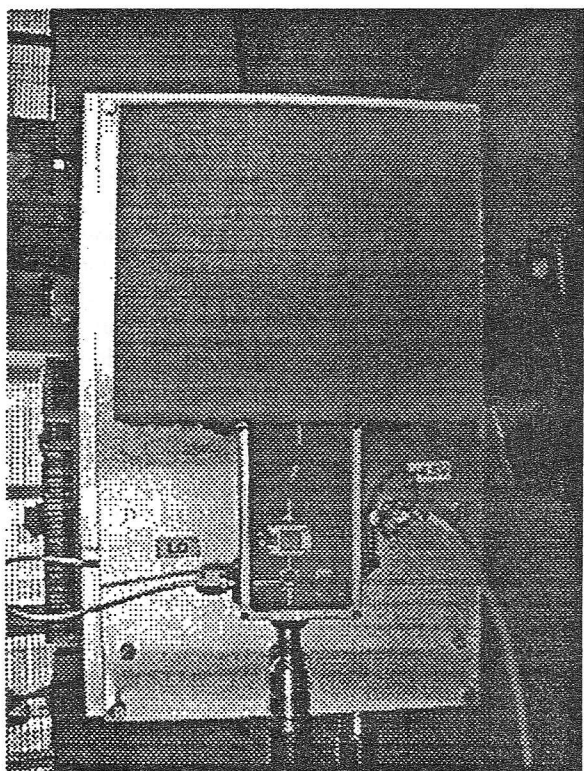


Figure 16 Photograph of the realized down converter.

CONCLUSION

Concept and possibilities of the new generation of mobile communication systems especially suitable for in-door communications is presented. System operates in microwave frequency range of 5 GHz and millimeter-wave range of 60 GHz with data rates up to 150Mb/s. Several solutions for expected problems during the investigation are proposed. The demonstration model operating at 5 GHz and 24 GHz is realized in order to perform experiments and to verify the basic concept.

All new ideas as well as new solutions will be applied also to new generation of microwave communication systems that are being under development in the IMTEL Institute.

REFERENCES:

- [1] Branković, V., Nešić, A., Zimmermann, S.: "Antenna Solution for High Data Rate In-Door Communication System in MM-wave Range", pp. 411-416, Mobile Comm. Summit, Rhodos, 1998.
- [2] Branković, V., Dölle, T., Korschak, T., Krupžević, D., Nešić, A.: "Dual Frequency (24/5) GHz OFDM Based Front-end for In-door Communication Systems", 4th Acts Mobile Communication Summit, June 1999, Sorrento, Italy.
- [3] Nešić, A., Jovanović, S., Branković, V.: "Design of Printed Dipoles Near the Third Resonance", IEEE AP-S, Atlanta, June 1998, Vol. 2. pp. 928-931.
- [4] Nešić, A., Radnović, I., Mikavica, M.: "Printed Antenna and Array with Circular Polarization", Electronics Letters, Vol. 32, No. 9, pp. 785-786, April 1996.
- [5] Nešić, A., Branković, V., Radnović, I.: "New Circularly Polarized Printed Antenna with Conical Beam", Electronics Letters, Vol. 32, No. 12, pp. 1165-1166, June 1998.
- [6] Nešić, A., Radnović, I., Branković, V.: "Ultrawideband Printed Antenna Array for 60GHz Frequency Range", IEEE AP-S International Symposium 1997, Montreal, Canada, July 1997, Conference Proceedings, Vol. 2, pp. 1272-1275.
- [7] Nešić, A., Branković, V., Krupžević, D., Radnović, I.: "24 to 5 GHz Up/Down Converters with Integrated Antennas", 29th European Microwave Conference, Munich 1999, Germany, Conference Proceedings, pp. 153-156.

NOVEL MICROWAVE AND MILLIMETER-WAVE BIOMEDICAL APPLICATIONS

Olga Boric-Lubecke¹, Yoshio Nikawa², Wesley Snyder³, James Lin⁴, and Koji Mizuno⁵

¹ Bell Laboratories, Lucent Technologies, Murray Hill, USA

² Faculty of Engineering, Kokushikan University, Tokyo, Japan

³ North Carolina State University, USA

⁴ University of Illinois at Chicago, USA

⁵ Tohoku University, Japan

Abstract — Three biomedical applications of microwave and millimeter-wave technology are reviewed: thermal burn imaging, dental diagnostics, and non-invasive vital signs detection. Burn imaging and dental diagnostics are possible due to changes in dielectric properties of damaged tissue as compared to the normal tissues. Therefore, it is critical to evaluate complex dielectric permittivity for the tissue and frequency of interest. Vital signs detection uses motion sensor principle of a Doppler effect, which requires phase demodulation. Dental diagnostics and vital signs detection use active systems, while burn evaluation would use a passive imaging system.

I. INTRODUCTION

Recent surge in commercial use of microwave technology, especially in wireless communications, has produced widely available, cheap and compact, microwave components, circuits and systems. With the similar advances in computational power and information technology, a new ground was created for the use of microwaves and millimeter-waves in applications ranging from land mine detection to cancer therapy [1,2]. Due to the growing diversity and intensity of the electromagnetic fields that we are all immersed in every day, a great deal of effort has been concentrated on evaluation of possible effects of these fields on the human tissue [3,4]. Various other biomedical applications have been developed, including microwave balloon angioplasty in cardiology [5], and medical imaging [6], to mention just a few. In this paper, we would like to introduce the following three lesser known microwave and millimeter-wave applications: thermal burn imaging, dental diagnostics, and non-invasive detection of vital signs.

Thermal burn evaluation is based on the difference in black body radiation between normal and damaged tissue. Depending on the water content and physical temperature of the skin, it might be possible to determine if tissue has been partially or completely destroyed. Preliminary complex dielectric permittivity measurements in the frequency range of 30-40 GHz indicate that there might be sufficient difference between the normal skin and burn to enable the diagnostics [7]. Since this approach is passive, there would be no additional heating and damage done

during the examination. Also, this technique might be useful for determining healing progress under the bandages and clothing, since millimeter waves penetrate through thin layers of moderately lossy materials, unlike infrared radiation.

Dental diagnostics is based on detecting areas of higher absorption of electromagnetic radiation in a tooth, which correspond to areas affected by dental caries [8]. While healthy enamel and dentin have a low water content, and therefore exhibit low loss at microwave and millimeter wave frequencies, caries affected areas are more moist and therefore more lossy. It was shown that transmission coefficient for healthy and diseased parts of the tooth vary as much as 10 dB in the frequency range of 75-110 GHz [9]. Compared to X-ray imaging, besides the safety issue, this technique offers a more quantitative approach capable of early disease detection. Based on the same principle of increased absorption in caries areas, hyperthermia treatment of dental caries was also proposed [8,10].

Non-invasive detection of vital signs, such as heart rate and respiration rate, is possible using a radar microwave system, due to a Doppler shift caused by body movements during respiratory and circulatory contractions and expansions [11]. Periodic movement of lungs and heart results in frequency modulation of the back-scattered signal, with the modulation frequency proportional to velocity, and thus phase proportional to the displacement. This technique was demonstrated for detection of respiratory rate in 1975 [12], and heart rate in 1979 [13]. Since no sensor is required on the patient's body, and only minimal training is necessary for the use of the radar instrument, this approach is very attractive for use in home care and monitoring applications.

II. THERMAL BURN IMAGING

An accurate assessment of burn severity is crucial in determining the need for hospital admission and in guiding initial fluid restitution, as well as establishing a prognosis. Thermal burns are typically evaluated by simply looking at the patient, and estimating the percentage of the body area affected by the injury, as well as the thickness of the damaged tissue. There is a need for an accurate and automated system for burn diagnostics, which would allow for prompt evaluation

of burn severity, and determination of necessary treatment. An infrared camera is one candidate for such a system, however since it only records surface temperature it might not provide sufficient information on burn depth. Millimeter-wave camera in the 30-40 GHz frequency range might be able to provide additional information on burn thickness, since at such frequencies millimeter waves penetrate the skin to about physical thickness of normal skin and provide sufficient resolution.

Electromagnetic energy radiated from the skin depends on the physical temperature, as well as skin emissivity and penetration depth. All of these three parameters are expected to be altered in a different way in case of first, second and third degree burns. For first degree burns such as sunburn, dryer skin and increased physical temperature can be expected. However, in some cases sunburn is more of an immune response than a literal burn, and it is difficult to predict whether the skin will appear wetter or dryer. For second degree burns, or blister burns, lower emissivity due to the increased water content is expected, whereas it is not known how would physical temperature be affected. In the case of third degree or full thickness burns, extremely dry tissue would result in increased emissivity, and physical temperature reduced to room temperature is expected.

In passive imaging, the received signal is a weighted average of brightness temperatures over a volume of tissue viewed by an antenna. The volume of tissue viewed by the antenna is determined by the penetration depth of the electromagnetic energy at the observation frequency. The "penetration depth" of electromagnetic waves into a human body can be estimated from the "skin" depth for non-ideal conductors:

$$\delta = 1/\sqrt{\pi \mu f \sigma} \quad (1)$$

where μ is vacuum permeability, f frequency in Hz, and σ conductivity in S/m. At a distance of one "skin" depth from the surface, electric field would decrease to $1/e$ of its value at the surface, and most of (more than 90%) the electromagnetic energy would be dissipated as ohmic loss. Conductivity increases with frequency, and also depends very strongly on the water content of the tissue. As mentioned previously in regard to dental diagnostics, tissue with high water content, such as skin and muscle, as well as tissue with high blood infiltration, has very high conductivity, which means high loss and poor penetration. On the other hand, tissue with low water and blood content such as bones, fat, and healthy tooth enamel have low conductivity and allow penetration. Brightness temperature is a product of object emissivity and physical temperature. Emissivity represents a mismatch between an object and air, and depends on the dielectric and surface properties of the object. Increased water content

increases the dielectric constant, and thus reduces emissivity.

Millimeter-wave imaging will provide lower resolution than the infrared imaging, but this may be adequate, especially for very large burns. If a far field antenna is used (for example 0.5 m away from the subject), resolution of about 1 cm could be achieved with a lens (or dish antenna) of 0.5 m diameter, at 35 GHz. Higher resolution could be obtained using a small diameter (order of mm) transmission line probe (applicator) in close proximity to the observed area.

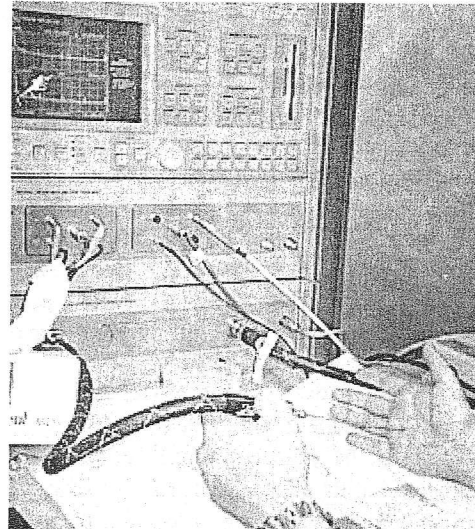


Fig. 1 Measurement test set-up for skin dielectric property evaluation. Reflection coefficient of open-ended coaxial probe terminated at the sample is measured using an Anritsu-Wiltron 360B network analyzer. Coaxial probe is 100 mm long, and has a diameter of 2.2 mm.

Complex dielectric permittivity provides a clue for determining emissivity and penetration depth, and it is thus important to evaluate it. Skin conductivity, and thus penetration depth can be calculated from the imaginary part, whereas both real and imaginary parts affect the air-dielectric reflection coefficient, and hence emissivity. While calculated data up to 100 GHz has been reported, measured data only up to 20 GHz can be found in the literature [14]. The technique described in [15] was used for the measurements. The reflection coefficient of an open coaxial probe in direct contact with the sample was measured using an Anritsu-Wiltron 360B network analyzer. Measurement test set-up is shown in Figure 4. Coaxial probe was 100 mm long, and had a diameter of 2.2 mm. The complex permittivity was calculated from the reflection coefficient, assuming that the impedance of the open coaxial line attached to a lossy medium of permittivity ϵ^* can be calculated as [15]:

$$Z(\omega, \epsilon^*) = 1/(j \omega \epsilon^* C), \quad (2)$$

where ω is the angular frequency, and C is the capacitance of the coaxial line open into free space,

related to the static capacitance [16]. The network analyzer was initially calibrated using a standard one-port calibration procedure at the input of the coaxial line. Next, an additional calibration was performed at the open end of the coaxial probe, using open, short, and deionized water as a known standard, to account for the parasitics between the probe and the sample, and to provide a reference impedance for determining C. The diameter of the coaxial probe was 2.2 mm, less than the expected wavelength in the 30-40 GHz range inside the skin tissue, and thus good accuracy could be achieved. All measurements were repeated five to ten times for similar probe positions, and an average was calculated.

Initially, the assumption that penetration depth in the 30-40 GHz range is less than physical thickness of the skin was verified. The complex permittivity of elbow skin was measured on one subject (Fig. 2), and the penetration depth was calculated from the imaginary part. Since "skin" depth varies between 0.5 mm and 0.7 mm [7], most of the electromagnetic energy would be absorbed within the typical physical thickness of the skin, and thus under-skin tissue does not affect the measured results.

Measured results for a small blister burn on the forearm, with a diameter of about 2 cm (Fig. 2), were compared with the adjacent unharmed skin on the same subject. An increase of about 10% was observed for both real and imaginary parts of the complex dielectric permittivity as compared to the adjacent unharmed skin, due to the increased water content under the skin surface. For the same reason, penetration depth is somewhat decreased. Even though this difference appears to be small, it still might significantly affect (decrease) emissivity and thus passive measurements, especially in the case of larger burns. While it would be difficult to distinguish such data absolutely from normal skin measurements, comparative measurements between adjacent normal and injured skin might provide sufficient sensitivity for burn diagnostics.

Next, measurements were done on the palm and back of the hand of three subjects. Skin on the back of the hand has very similar dielectric permittivity (Fig. 7) to elbow skin, and is probably representative for skin on most parts of the body. Palm skin (Fig. 8) has significantly lower dielectric permittivity, probably because it is a different type of skin with a thick horny layer (without hair cells), which appears equivalent to lower water content. A wet measurement was also made on the back of the hand on person 2, and a wet palm was measured on person 3. In both cases the dielectric permittivity is higher than that measured for corresponding dry skin on any of the three subjects (dashed lines in Fig. 7 and Fig. 8). While the increase in the real part of complex permittivity for the back of the hand is not very high, the imaginary part which represents loss is altered more significantly in both cases. In the case of wet

palm skin, an increase of about 50% was observed for the imaginary part of the complex permittivity.

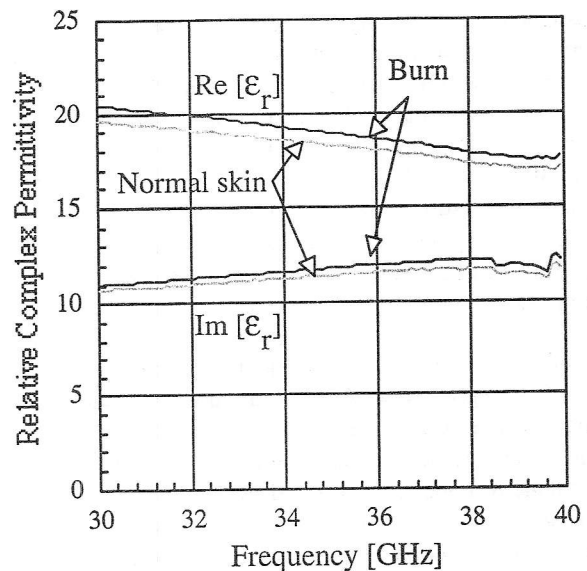


Fig. 2 Comparison of burn and normal skin dielectric permittivity. Both real and imaginary parts are increased in the case of a burn, due to the water content in the resulting blister.

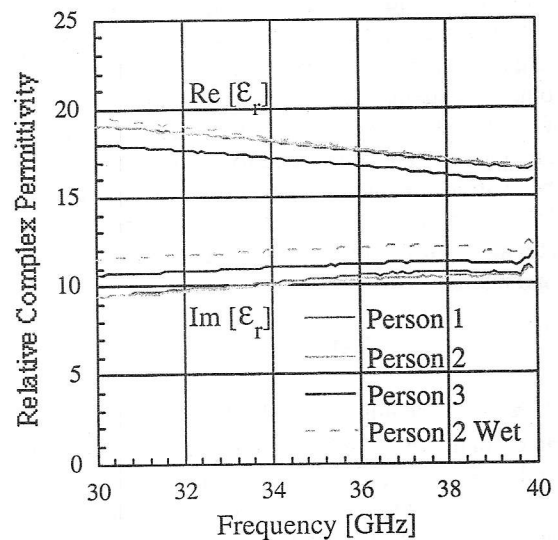


Fig. 3 Back of hand dielectric permittivity measured on three people. Wet hand data for Person 2 is higher than dry hand data for any of the subjects.

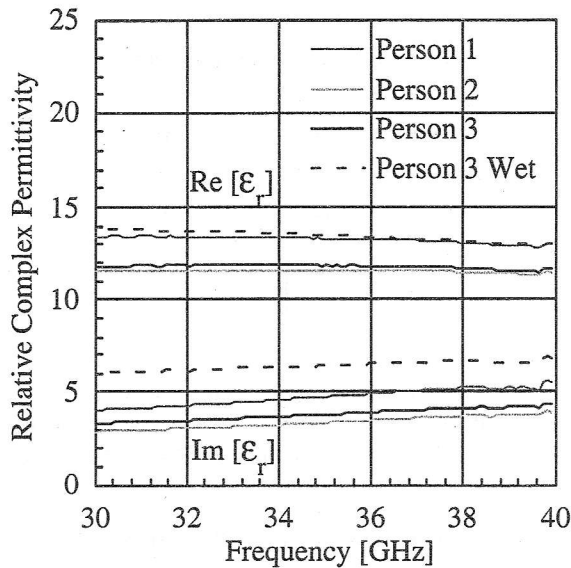


Fig. 4 Palm dielectric permittivity measured on three people. Wet palm data for Person 3 is higher than dry hand data for any of the subjects.

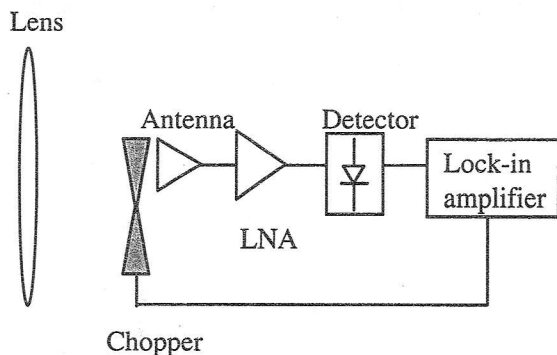


Fig. 5 Possible architecture for a direct detection radiometer for thermal burn evaluation.

Evaluated skin complex permittivity for the case of normal skin and blister burn, palm and back of the hand, and wet and dry skin, up to 40 GHz, shows clear difference in three cases. This indicates that different emissivity and penetration depth can be expected for normal skin and different burn types, which might allow for millimeter-wave thermal burn diagnostics. Further radiometric measurements are necessary to confirm this. Direct detection total power radiometer, such as one shown in Figure 5 could be used for such measurements. This system uses a small aperture antenna placed in the focal point of a large dielectric lens (0.5m diameter for 30-40 GHz), to achieve centimeter resolution at a distance of 0.5m. Received signal is amplified using a broad-band low noise amplifier chain, with the total gain of 50-60 dB, and rectified using a square law detector such as Schottky diode. Use of a lock-in amplifier and a mechanical chopper improves the sensitivity of the receiver. If a receiver array is used, measurement can

be performed in real time, otherwise single element would have to be scanned to retrieve the image.

III. DENTAL DIAGNOSTICS

Dental diagnostics is commonly done using dentist's subjective observation of tooth properties, such as color and surface hardness, as well as clinical symptoms such as pain and discomfort. More objective diagnostics can be obtained using X-ray imaging. However use of X-rays has two main drawbacks: X-rays are well known to cause damage to the human tissue, and in the initial stages of the dental caries it is difficult to distinguish healthy tissue from the tissue affected by the disease in an X-ray image.

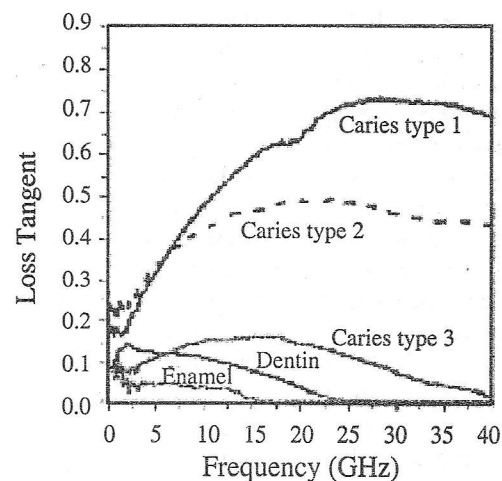


Fig. 6 Loss tangent as a function of frequency for three types of caries, dentin, and enamel. All types of caries exhibit significantly higher loss tangent above 20 GHz.

Possibility of using microwave and millimeter-wave technology for dental diagnostics and treatment has been investigated by measuring the complex dielectric permittivity of enamel, dentin and dental caries [8]. Reflection coefficients of healthy and diseased teeth were measured in the frequency range of 0-40 GHz, using the procedure described in the previous section for skin measurements. The tooth material was classified as enamel, dentin, and dental caries of Type 1, 2, and 3, with Type 1 indicating the highest moisture content. Both real and imaginary part of the relative dielectric permittivity are increased significantly in caries samples as compared to the normal tooth, due to increased water content. Figure 1 shows the loss tangent for three types of caries, enamel and dentin, indicating that even the least lossy caries sample, Type 3, has significantly higher loss tangent than both enamel and dentin, particularly above 20 GHz. Areas of dental caries are soft, and have higher water content than areas of healthy tooth. It is therefore expected that transmission coefficient through a healthy tooth would be higher than through

a diseased tooth, providing a quantitative measure of caries.

Transmission coefficients for a healthy tooth and a tooth affected by dental caries were measured at 35 GHz, using the experimental set-up shown in Figure 2. Tooth samples were irradiated from the rectangular waveguide, and the transmitted wave was received by another waveguide on the opposite side of the sample. Silicone rubber sheets were placed in the apertures of both waveguides, to reduce the mismatch between the air-filled waveguide and the sample and to provide a smooth interface. The aperture size of the waveguide was 3.5 mm by 7.0 mm. Transmission coefficients for five samples of extracted adult teeth, measured using a network analyzer, are shown in Figure 3. Sample one, with the severe case of caries, was divided into parts with less advanced and more advanced caries. Samples two to five were divided into a healthy part and a part with caries. Figure 3 shows that transmission coefficient is very similar for healthy teeth samples, whereas it is at least 1 dB lower for caries areas, and varies with the severity of the disease. In this case, waveguide aperture size was large compared to the caries sites, and it was not possible to determine the position of caries accurately.

To improve resolution, transmission coefficient was measured for healthy and diseased tooth samples in the frequency range from 33 to 110 GHz [8]. Three sizes of waveguide applicators were used: 5.6 mm by 2.8 mm for frequency range of 33-50 GHz, 3.8 mm by 1.9 mm for frequency range of 50-75 GHz, and 2.6 mm by 1.3 mm for frequency range of 75-100 GHz. Silicon rubber was not used for these measurements. Transmitted power was received using horn antennas of the appropriate size on the opposite side of the samples. Since the aperture size was very small, it was possible to measure specific areas on each sample. It was found that difference in transmission coefficients between the healthy and diseased sites increases as aperture size decreases. While this difference was about 4 dB in the frequency range of 33-50 GHz, it increased to about 7 dB in the frequency range of 50-75 GHz, and to about 10 dB in the frequency range of 75-110 GHz.

The attenuation of millimeter-waves in the caries infected areas suggests that these areas can be heated selectively in order to kill the microorganisms causing the disease. It has been reported that some portions of the caries affected areas can be re-calcified if these areas are kept septic. Therefore it might be possible to provide a caries treatment using millimeter-waves. Well focused, high frequency millimeter-waves would be required for such treatment, in order not to heat and damage the surrounding healthy tissue.

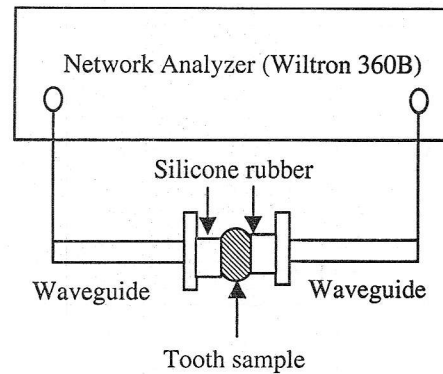


Fig. 7 Experimental set-up for measuring transmission coefficient through teeth samples. Pieces of silicone rubber were used to improve the coupling from the waveguide to the sample.

IV. VITAL SIGNS DETECTION

Remote sensing of body movements associated with the expansion and contraction of the circulatory and the respiratory systems provides a non-invasive, "no-sensor" technique for vital signs detection. It has been shown [11] that heart rate and respiratory rate can be determined using a microwave radar-like system shown in Figure 8.

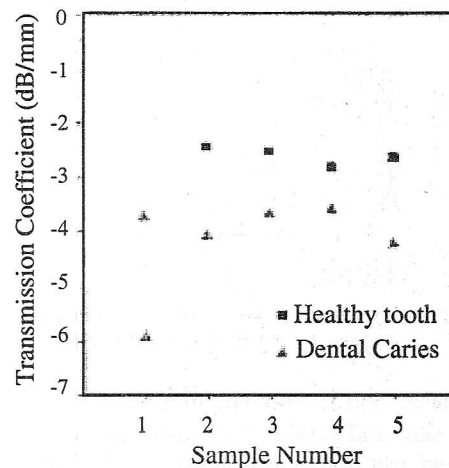


Fig. 8 Transmission coefficient measured at 35 GHz for five samples of extracted adult teeth. Caries samples exhibit 1dB or more loss than healthy samples.

A back-scattered signal contains the Doppler shift due to the movement of heart and lungs. Doppler shift f_d , for a signal at frequency f , and a constant target velocity v in the direction of interrogation, can be calculated as:

$$f_d = 2vf/c, \quad (3)$$

where c is a speed of light. Since heart and lung movements are periodic, these movements will produce a phase shift in the reflection signal, analogous to the phase shift due to the varying termination location on the transmission line (Fig. 10).

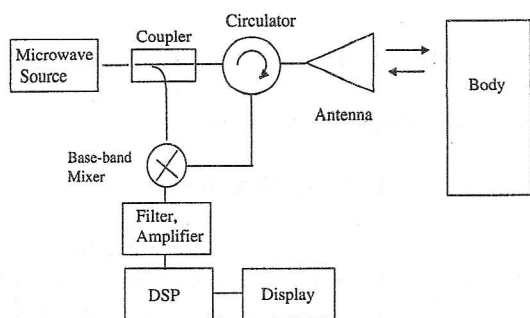


Fig. 9 Experimental set-up for non-invasive detection of heart rate and respiration rate. A small portion of the transmitted signal is typically used to provide a local oscillator for a base-band mixer.

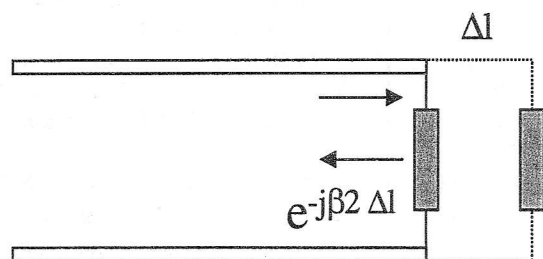


Fig. 10 Doppler shift for periodic motion is analogous to the phase shift due to the variation of the termination position on a transmission line.

Transmitted and received signals are typically isolated using a circulator or a directional coupler. Received signal is mixed down to base-band, using a small portion of the transmitted signal as a local oscillator. At this point, received signal is frequency demodulated, and it is necessary to integrate it to obtain phase demodulation. Integration can be performed using hardware such as low-pass or a band-pass filter, or using digital signal processing.

Transmitted signal undergoes multiple reflection at interfaces between different tissue layers, before reaching the heart. We can assume that body is composed of layers of skin, fat, muscle and bone. At frequencies below 10 GHz, about half of the incident power is reflected from the body [17]. The other half propagates further, being attenuated in each layer, and partially reflected at each interface. On the average, signal reflected from the heart is about 20-30 dB lower than the signal reflected for the chest. Since most of the breathing pattern is typically contained within less than 0.5 Hz, and heart pattern within the frequency range of 0.5-50 Hz, it is possible to separate these two signals through the appropriate filtering [18]. Figure 11 shows a breathing pattern and a heart beat pattern recorded simultaneously with such filtering. An X-band Doppler transceiver operating at 10.5 GHz, with the output power of 5-10mW was used for these measurements.

Since the phase demodulated received signal is proportional to displacement, it is possible to obtain more information on the heart behavior besides the

simple heart rate. Figure 12 shows the microwave apexcardiogram obtained at 2.45 GHz, along with the phonocardiogram and electrocardiogram (ECG) that were recorded simultaneously [13]. Microwave measurements were done using a 2.45 GHz radar system, with a coaxial applicator antenna. Antenna was placed over the apex of the heart with a distance of about 3 cm between the applicator surface and the chest wall of the subject. Subject was holding breath during the measurements to simplify the procedure. All three recording show the same periodicity, and events identified by ECG can also be identified in a microwave signature. Microwave signature also provides additional information due to the fact that it tracks motion, while ECG tracks the electrical activity.

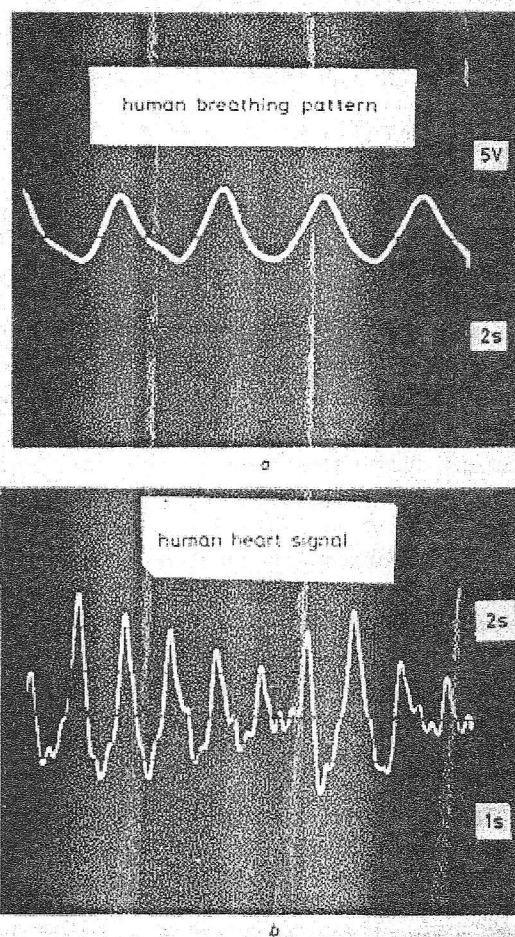


Fig. 11 Breathing pattern (a) and a heart beating pattern (b) recorded simultaneously using an X-band Doppler radar.

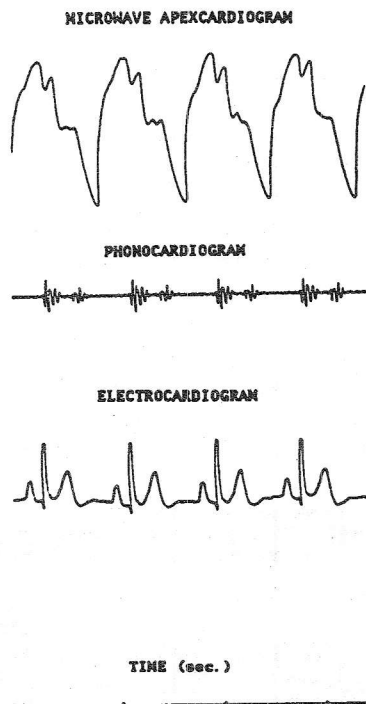


Fig. 12 Microwave apexcardiogram, phonocardiogram, and electrocardiogram recorded simultaneously. Microwave measurements were done at 2.4 GHz.

CONCLUSIONS

Three microwave/millimeter-wave biomedical applications have been reviewed: thermal burn imaging, dental diagnostics, and non-invasive detection of vital signs. Passive millimeter-wave imaging might provide ways for accurate and timely assessment of thermal burn severity. Preliminary experiments indicate that significant change in dielectric properties might be expected in case of burns, and thus provide sufficient sensitivity for accurate millimeter-wave characterization. However, radiometric experiments are necessary to confirm the usefulness of this technique. Use of millimeter waves for dental diagnostics, based on increased absorption of electromagnetic waves in the parts of teeth affected by caries due to increased water content, is a promising new technique which may complement or even eliminate the use of X-rays. Potential for the treatment of caries using millimeter-waves due to selective heating has also been indicated. Finally, non-invasive detection of vital signs based on Doppler effect due to respiratory and vascular movement has been revisited. This technique might be particularly useful in cases where direct contact with the patient is not desirable, for example if patient has severe burns, and also in cases when contact is not possible, such as in search and rescue operations.

ACKNOWLEDGMENT

We would like to thank Y. Abiru and Y. Akutsu for assistance in skin measurements, and V. M. Lubecke for his help in preparing the manuscript.

BIBLIOGRAPHY

- [1] A. W. Guy, "History of biological effects and medical applications of microwave energy," *IEEE Tran. Microwave Theory and Technique*, vol. 32, pp. 1182-1200, 1984.
- [2] Special issue on "Hyperthermia and cancer therapy," *IEEE Tran. Microwave Theory and Technique*, vol. 34, 1986.
- [3] V. Hombach, K. Meier, M. Burkhardt, E. Kuhn, and N. Kuster, "The dependence of EM energy absorption upon human head modeling at 900 MHz," *IEEE Tran. Microwave Theory and Technique*, vol. 44, pp. 1865-1873, October 1996.
- [4] A. Vander Vorst and F. Duhamel, "1990-1995 advances in investigating the interactions of microwave fields with the nervous system," *IEEE Tran. Microwave Theory and Technique*, vol. 44, no. 10, pp. 1898-1909, October 1996.
- [5] A. Rosen, P. Wallinsky, D. Smith, Y. Shi, Z. Kosman, A. Martinez-Hernandez, H. Rosen, F. Sterzer, D. Mawhinney, A. Presser, J. Chou, P. Goth, and G. Lowery, "Percutaneous transluminal microwave balloon angioplasty," *IEEE Tran. Microwave Theory and Technique*, vol. 38, pp. 90-93, 1990.
- [6] J. C. Bolomey, "Recent European developments in active microwave imaging for industrial, scientific and medical applications," *IEEE Tran. Microwave Theory and Technique*, vol. 37, no. 12, pp. 2109-2117, December 1989.
- [7] O. Boric-Lubecke, Y. Nikawa, W. Snyder, and K. Mizuno, "Skin Properties at Millimeter Waves," Accepted for presentation at the 1998 *Asia-Pacific Microwave Conference*, December 8-11, 1998, Yokohama, Japan.
- [8] N. Hoshi, Y. Nikawa, K. Kawai, and Shigeyuki Ebisu, "Applications of Microwaves and Millimeter Wave for the Characterization of Teeth for Dental Diagnostics and Treatment," *IEEE Tran. Microwave Theory and Technique*, vol. MTT-46, no. 6, pp. 834-838, June 1998.
- [9] N. Hoshi, Y. Nikawa, K. Kawai, and Shigeyuki Ebisu, "Study on Diagnosis for Tooth Using Millimeter-Waves," *1998 IEEE MTT-S Digest*, pp., Baltimore, Maryland
- [10] E. Eildelman, S. B. Finn, and T. Koulrises, "Remineralization of carious dentine treated with calcium hydroxide," *J. Dent. Child*, vol. 32, pp. 218-225, 1965.
- [11] J. C. Lin, "Microwave Sensing of Physiological Movement and Volume Change,"

- Bioelectromagnetics*, vol. 13, pp. 557-565, December, 1992.
- [12] J.C. Lin, "Non-invasive microwave measurement of respiration," *Proc. of IEEE*, vol. 63, pp.1530, 1979.
- [13] J. C. Lin, J. Kiernicki, M. Kiernich, P. B. Wollschaefer, "Microwave apexcardiography," *IEEE Tran. Microwave Theory and Technique*, vol. 27, pp. 618-620, 1979.
- [14] S. Gabriel, R. W. Lau, and C. Gabriel, "The Dielectric Properties of Biological Tissues: II, III," *Phys. Med. Biol.* 41, pp. 2251-2293, 1996.
- [15] E. C. Burdette, F. L. Cain, and J. Seals, "In Vivo Probe Measurement Technique for Determining Dielectric Properties at VHF Through Microwave Frequencies, " *IEEE Tran. Microwave Theory and Technique*, vol. MTT-28, no. 4, pp. 414-427, April 1980.
- [16] M. A. Stuchly and S. S. Stuchly, "Coaxial Line Reflection Methods for Measuring Dielectric Properties of Biological Substances at Radio and Microwave Frequencies-A Review," *IEEE Trans. Instrum. Meas.*, vol. IM-29, no. 3, pp.176-183, September 1980.
- [17] J. C. Lin, "Electromagnetic interaction with biological systems," Plenum Press, New York, 1989.
- [18] K. H. Chan and J. C. Lin, "Microprocessor-based cardiopulmonary rate monitor," *Medical & Biological Engineering & Computing*, vol. 25, pp. 41-44, January 1987.

AN IMPROVED WEATHER RADAR SIGNAL PROCESSING ALGORITHM IMPLEMENTED ON MITSUBISHI RC-34A RADAR

*Aleksandar T.Kostić**, *Bratislav D.Milovanović***, *Predrag D.Vuković***, *Predrag M.Eferica***,
*Dejan D.Rančić***

* *Military Technical Institut, Beograd*

** *Elektronski Fakultet, Niš*

ABSTRACT: A precise estimation of C_b (cumulonimbus) cloud cells reflectivity is essential for effectiveness of the rocket method seeding in the hail suppression activities. An improved weather radar signal processing algorithm implemented on MITSUBISHI RC-34A radar, described in this paper, is contribution to this efficiency. The algorithm involves radar finite bandwidth receiver calibration, time, angle and range averaging of radar signals and transforms radar signal amplitude at the receiver output in corrected equivalent reflectivity factor. The equivalent number of independent samples as a measure of uncertainty related to the variance of the radar signal processed by the finite bandwidth radar receiver is also given in the paper.

KEYWORDS: Weather radar, Receiver calibration, Weather echo averaging, Finite bandwidth receiver, Signal correction.

EQUIVALENT REFLECTIVITY FACTOR

In radar meteorology, the average of the weather echo power is used in the computation of reflectivity, liquid water content, rainfall rate, etc. Since the main objective of radar observation is to obtain as precise estimate of target's reflectivity as possible, the raw receiver signal must undergo several processing steps, transforming receiver output voltage to standard reflectivity measure, dBZ (reflectivity factor in dB).

The weather radar equation that gives the mean power, of the weather signal samples, in terms of Z_e , equivalent reflectivity factor, expressed in units conventional to the radar meteorologist, [4], [3], as:

$$(1) \quad \bar{P}_o(mW) = \frac{\pi^5 10^{-17} P_t(W) g^2 g_s \tau (\mu s) \theta_1^2 (^\circ) |K_w|^2 Z_e (mm^6 / m^3)}{6.75 \times 2^{14} (\ln 2) r_0^2 (km) \lambda^2 (cm) \ell^2 \ell_r \ell_{T-R}}$$

where: P_t - transmitter peak power, g - antenna gain, g_s - system power gain, $|K_w|^2$ - refractive index, τ - pulse width, θ_1 - beamwidth, r_0 - range, λ - wavelength, ℓ - atmospheric attenuation loss, ℓ_r - receiver finite bandwidth loss factor, ℓ_{T-R} - transmitter-receiver loss. Then, equivalent reflectivity factor is:

$$(2) \quad Z_e = \frac{\bar{P}_i r_0^2 \ell_r \ell^2}{C_1}$$

C_1 - constant including parameters from equation (1)

RECEIVER CALIBRATION

Power measurements are always made at the receiver output and we must relate this to reflectivity. This requires a calibration of the receiver to determine the losses (gain) in echo power as it passes through the receiver. Calibration can be done with a signal generator of known power, stable amplitude, and continuous wave. Calibration corrections are necessary to account for weather echo amplitude fluctuations if nonlinear receiver is employed. Logarithmic module is used in MITSUBISHI RC34A radar receiver.

Receiver frequency response will attenuate echo power even if the cw (continuous wave) calibrating source indicates no losses in the receiver. Although attenuation of different spectral components by the receiver is not the same, we can conveniently account for this loss by a receiver finite bandwidth loss factor. This loss is a function of both the shape of the transmitted pulse and the receiver's frequency response.

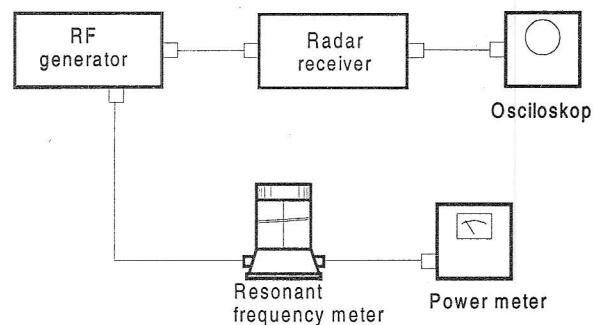


Figure 1. Measurement method

The calibration curves and receiver's frequency response measurement method is established according to the figure 1. Of course, a network analyzer is better solution, but it is not a usual part of maintenance tools or instruments.

Calibration and receiver frequency response curves measurement is the first step which should provide the parameter values used in signal processing algorithm.

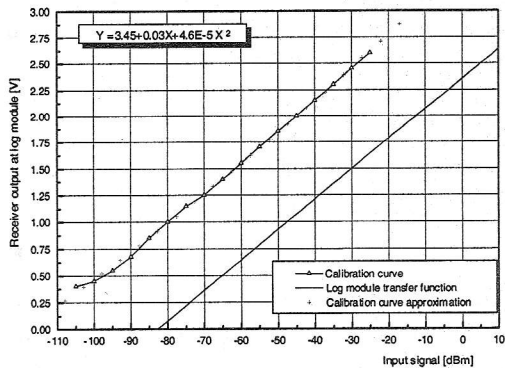


Figure 2. Receiver calibration curve and transfer function of logarithmic module at the Kukavica radar site

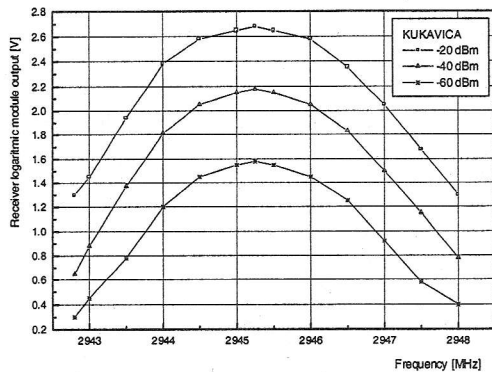


Figure 3. Receiver frequency response measured at the logarithmic module output at the Kukavica radar site

Calibration curve, figure 2, plots the relation between RF power at the input and measured values of signal amplitude at the receiver output, whereas receiver bandwidth, obtained from receiver frequency response curve, figure 3, is needed for receiver finite bandwidth loss factor calculations, [1], [2].

Because of the large weather echo dynamic range, the receiver chain with logarithmic module at the end of it performs weather echo signals amplification in MIT-SUBISHI RC34A. For the analysis purpose, the receiver is divided into two parts, linear, consisting of RF preamplifier, mixer, IF amplifier, and nonlinear logarithmic amplifier-detector module. Installed logarithmic module has frequency bandwidth (greater than 10 MHz) much wider than echo signal spectrum (0.5 MHz), and bandwidth of the receiver linear part (about 2 MHz). Therefore, it is assumed that the logarithmic module frequency bandwidth is infinity and its influence on the receiver bandwidth doesn't exist. Taking into consideration previous assumption, one

can, using the logarithmic module gain curve supplied by manufacturer, transform frequency response measured values into those, corresponding to the bandwidth of receiver linear part. The obtained frequency response of the receiver linear part is, then, normalized and approximated with:

$$(3) \quad G(f) = g_0 + \frac{A}{B_6} \sqrt{\frac{4 \ln 2}{\pi}} \exp \left[-\frac{4 \ln 2 f^2}{B_6^2} \right]$$

and, it gives the finite receiver bandwidth that is necessary for losses calculations, figure 4. B_6 is 6dB frequency band and A -area below approximation curve, g_0 -bias (adopted to be zero)

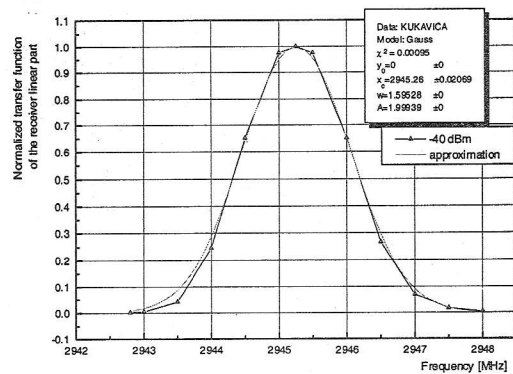


Figure 4. Receiver linear part normalized frequency response function at the Kukavica radar site

Knowing the receiver bandwidth, one can calculate pulse shape at the output of the receiver linear part using the following equation:

$$(4) \quad V_{0LIN}(t) = A_0 \left\{ g_0 + \frac{A}{B_6} \sqrt{\frac{\ln 2}{\pi}} \left\{ \operatorname{erf} \left[\frac{\pi B_6}{\sqrt{4 \ln 2}} \left(t + \frac{\tau}{2} \right) \right] - \operatorname{erf} \left[\frac{\pi B_6}{\sqrt{4 \ln 2}} \left(t - \frac{\tau}{2} \right) \right] \right\} \right\}$$

and get the range weighting function as:

$$(5) \quad W(r) = g_0 + \frac{A}{B_6} \sqrt{\frac{\ln 2}{\pi}} \left\{ \operatorname{erf} \left[\frac{2\pi B_6}{c\sqrt{4 \ln 2}} \left(r_0 - r + \frac{c\tau}{4} \right) \right] - \operatorname{erf} \left[\frac{2\pi B_6}{c\sqrt{4 \ln 2}} \left(r_0 - r - \frac{c\tau}{4} \right) \right] \right\}$$

Since the integral of $|W(r)|^2$ is equal $c\tau/2$ for infinite bandwidth, the finite bandwidth loss factor, [14], [4], can be defined as:

$$(6) \quad \ell_r \equiv \frac{c\tau}{2} \int_0^\infty |W(r)|^2 dr$$

which is the weather signal power loss caused by the finite bandwidth of the receiver.

Including attenuation in gases and the finite bandwidth loss factor in eq. (2), it can be calculated equivalent reflectivity factor vs. signal level at the receiver output and display that data on the screen. The Kukavica radar is treated as example on figure 5.

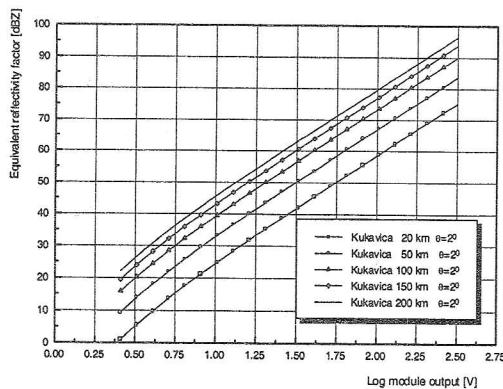


Figure 5. Equivalent reflectivity factor in dBZ (eq.2) vs. signal level at the log module output for Kukavica radar

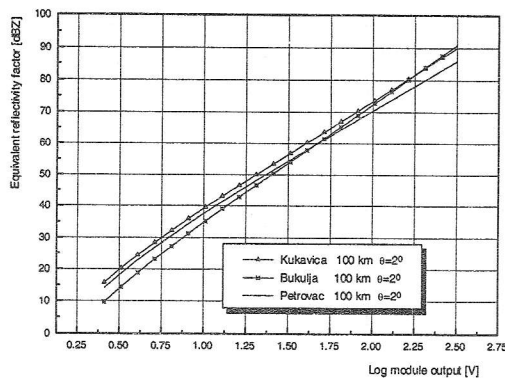


Figure 6. Same as fig.5 for three radars

Figure 6 shows differences between three radars of the same type, MITSUBISHI RC34A. Knowing these differences is of essential importance for composite radar pictures calculations in a radar network.

SIGNAL PROCESSING ALGORITHMS

step 1: Sweep-to-sweep averaging

The role of the receiver output signal averaging is twofold: a) to obtain an estimate of mean reflected

power, P_k , since rain echo signal is random, b) to limit receiver thermal noise influence to detection process, [15]. The samples of receiver output voltage, $U_{n,k}$ [V], are converted to corresponding power at receiver input by means of look-up table implementing radar calibration curve (in our case it was enough to use 2nd order polynomial with coefficients A_i , $i=0,1,2$ obtained from measured calibration curve by minimum square error second order polynomial fit), [8]:

$$(7) \quad P_{n,k} [\text{dBm}] = A_2 (U_{n,k})^2 + A_1 U_{n,k} + A_0$$

The corresponding samples of the receiver input power (i.e. corresponding range gates) from successive sweeps, $P_{i,k}$, are averaged by means of moving window, [5], N sweeps long, with equal weights:

$$(8) \quad \hat{P}_{n,k} = \frac{1}{N} \sum_{i=n-N/2+1}^{n+N/2} P_{i,k} = \frac{1}{N} [N\hat{P}_{n-1,k} + P_{n+N/2,k} - P_{n-N/2,k}]$$

for $N \in \{2,4,8,16,32\}$

This kind of averaging is chosen since it lends itself to very efficient recurrent implementation. Provided that $N\hat{P}_{n-1,k}$ is stored from previous calculations, only three operations are required per sample – addition, subtraction and shift. However, the estimation problem is complicated due to the fact that the receiver input-output transfer function, $P_{n,k} = g(A_{n,k})$ ($A_{n,k}$ is n -th sweep, k -th range gate receiver input signal envelope), is nonlinear since MITSUBISHI RC34-A weather radar employs logarithmic receiver. Under assumption of Rayleigh distributed receiver input envelope, i.e.,

$$(9) \quad p(A_{n,k}) = \frac{2A_{n,k}}{\bar{P}_{n,k}} \exp\left(-\frac{A_{n,k}^2}{\bar{P}_{n,k}}\right)$$

the mean power estimate $\hat{P}_{n,k}$, obtained using eq.(8), is biased by constant factor (in dB) (compared to unbiased one, obtained by averaging of input power in linear domain, which would be prohibitively time consuming due to need for mean power estimate logarithm calculation in order to obtain reflectivity [dBZ]). The expected value and the standard deviation of signal power estimation $\hat{P}_{n,k}$, for logarithmic receiver-detector are, respectively:

$$(10) \quad E(\hat{P}_{n,k}) = \Gamma^N \left(1 + \frac{1}{N}\right) \bar{P}_{n,k}$$

$$\sigma(\hat{P}_{n,k}) = \left(\Gamma^N \left(1 + \frac{2}{N}\right) - \Gamma^{2N} \left(1 + \frac{1}{N}\right)^2 \right)^{0.5} \bar{P}_{n,k}$$

where Γ denotes the gamma function, [12].

step 2: Block averaging

When observing more distant ranges, resulting range gate may give rise to sampling frequency under the Nyquist frequency determined by receiver bandwidth. In order to prevent aliasing, radar echo is sampled at 2, 4 or 8 times higher rate than determined from Δr . After performing step 1, samples blocks of length equal to oversampling factor are averaged in order to reduce amount of data.

step 3: Detection

Influence of the receiver thermal noise on the meteorological products display is limited by comparing averaged signal level with threshold obtained by slightly modified well-known CA-CFAR algorithm, applied on periodically estimated mean noise power. Estimation is obtained by averaging noise samples, from a few gates belonging to the time interval beyond maximum range of radar, under assumption that the time interval is clear of clutter and meteorological targets. Threshold value is determined from estimated mean noise power, desired false alarm rate and overall averaging factor $N_a = N + N_b$, according to the CFAR algorithm. Only the signals above threshold undergo step 4 processing.

step 4: Signal corrections

This step integrates several corrections that have to be applied to averaged signal in order to obtain reflectivity from it. As the first, the estimate of mean input signal power is corrected for the bias arising from the fact that the estimate is obtained by averaging in logarithmic domain. After that, a compensation for atmospheric and attenuation due to distance of the observed distributed scatterers (an analogue to Sensitivity Time Control in classic radar designs) is effected. Thus, the reflectivity measure expressed in dBZ is obtained:

$$(11) \quad 10 \log Z_{n,k} [dBZ] = \hat{P}_{n,k,dB} + C_{bias,dB} - C_{1dB} + 20 \log r_0 + 20 \log \ell + 10 \log \ell_r$$

TIME, ANGLE AND RANGE AVERAGING OF RADAR ECHOES

The uncertainty in measuring or estimating average weather echo power is important in establishing confidence in the computed values. To help establish a confidence level, we note that there exists a unique

relationship between the weather radar echo correlation function and the receiver detected output correlation function. This unique relationship is used here to calculate the variance of the average weather echo estimates. Another measure of uncertainty related to the variance is the equivalent number of independent samples. In this work, the equivalent number of independent samples for average weather echoes at the output of logarithmic receiver with finite bandwidth is calculated.

Kerr, [6], relates the normalized correlation function of the output signal for logarithmic module of the receiver to the correlation function ρ of signal at the input of it, as:

$$(12) \quad \rho_{\log}(\tau) = \frac{6}{\pi^2} \sum_{m=1}^{\infty} \rho^{2m} m^{-2}$$

Correlation function need not be restricted to explicit function of time, and is a function of the input signal correlation which may include time, angle and range as independent variables. It can be shown that the normalized correlation function is:

$$(13) \quad \rho(\delta\tau, \Delta, \delta T_s) = \rho(\delta\tau)\rho(\Delta)\rho(\delta T_s)$$

where, $\rho(\Delta)$, $\rho(\delta T_s)$ and $\rho(\delta\tau)$ are the normalized correlation functions for time, angle and range, respectively, [11], [10].

The equivalent number N_i of independent samples has been defined as the ratio of the variance of a single sample to the variance of the sampled mean (Nathanson [16]). For discrete sampling N_i is given as:

$$(14) \quad N_i^{-1} = \frac{1}{N_q} + \frac{2}{N_q^2} \sum_{K_q=1}^{(N_q-1)} (N_q - K_q) \cdot \rho_q(K_q \ell_q)$$

Averaging in range space. A rectangular transmitted pulse shape of length τ is considered. Correlation function at the output of linear part of the receiver is:

$$(15) \quad R_{vv}(\delta\tau_s) = B_6^2 \sqrt{\frac{\pi}{8 \ln 2}} \cdot \tau \bar{P}_r \int_{-1}^{+1} (1 - |x|) \exp \left[-\frac{(\pi \tau B_6)^2}{8 \ln 2} \left(x - \frac{\delta\tau_s}{\tau} \right)^2 \right] dx$$

and its normalized form:

$$(16) \quad \rho_{vv}(\delta\tau_s) = \frac{R_{vv}(\delta\tau_s)}{R_{vv}(0)}$$

Combining equation (16) with equation (12), the receiver correlation function at the output of logarithmic module (including finite receiver bandwidth) becomes

$$(17) \quad \rho_{\log}(\delta\tau_s) = \frac{6}{\pi^2} \sum_{m=1}^{\infty} \rho_{vv}(\delta\tau_s)^{2m} m^{-2}$$

and equivalent number of independent samples:

(18)

$$N_i^{-1} = \begin{cases} \frac{1}{N} + \frac{12}{N^2\pi^2} \sum_{k=1}^{K_u} (N-k) \sum_{m=1}^{\infty} \rho(k\ell_r)^{2m} m^{-2}, & K_u \leq \frac{\tau}{\ell_r} \\ \frac{1}{N}, & \ell_r > \tau \end{cases}$$

is shown on the next picture 7.

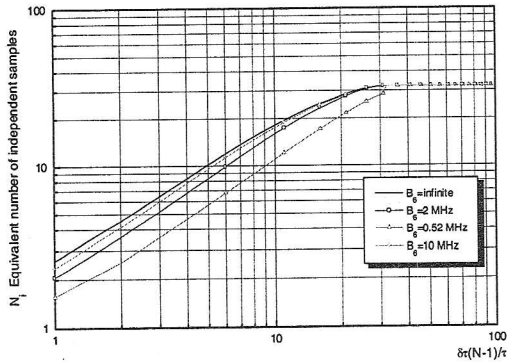


Figure 7. Equivalent number of independent samples for averaging in range space (finite receiver bandwidth as parameter)

Averaging in time and angle space. In a typical pulsed radar system, e.g. MITSUBISHI RC34A, weather echo signals are sampled at fixed ranges and regularly spaced times while the antenna axis changes angular position at a constant rate. Under these conditions, one need only to consider time and range as independent variables. Angle sampling is then related to time in terms of a constant rotation rate. Correlation function for angle and time at one range, at the output of linear part of the receiver, is:

(19)

$$R_{vv}(\theta_e, \delta T_s) = B_c^2 \sqrt{\frac{\pi}{8 \ln 2}} \cdot \bar{P}_r \int_{-\infty}^{+\infty} \exp \left[-\frac{\epsilon^2}{2(\sigma_r')^2} - \frac{(\delta T_s - \epsilon)^2}{2\sigma_h^2} \right] d\epsilon$$

and its normalized form:

$$(20) \quad \rho_{vv}(\theta_e, \delta T_s) = \frac{R_{vv}(\theta_e, \delta T_s)}{R_{vv}(\theta_e, 0)}$$

Combining equation (20) with equation (12), the receiver correlation function at the output of logarithmic module (including finite receiver bandwidth) become

$$(21) \quad \rho_{\log}(\theta_e, \delta T_s) = \frac{6}{\pi^2} \sum_{j=1}^{\infty} \rho_{vv}(\theta_e, \delta T_s)^{2j} j^{-2}$$

and equivalent number of independent samples for combined time and angle sampling:

(22)

$$N_i^{-1} = \frac{1}{N} + \frac{12}{N^2\pi^2} \sum_{m=1}^{N-1} (N-m) \sum_{j=1}^{\infty} \rho_{\log}(\theta_e, mT_s)^{2j} j^{-2}$$

is shown on the picture 8.

To include range with the combined time and angle sampling, N_i , would be the number computed (for time-angle) multiplied by the number of independent samples in range.

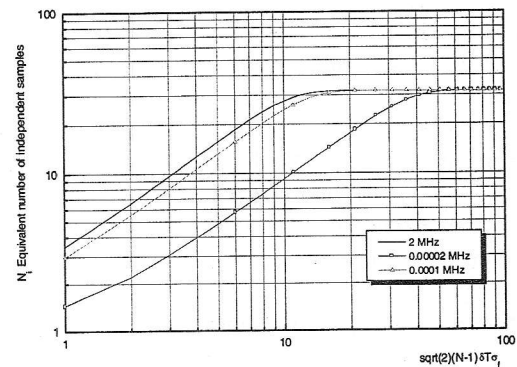


Figure 8. Equivalent number of independent samples for averaging in time and angle space (finite receiver bandwidth as parameter)

Let's take as numerical example radar MITSUBISHI RC-34A at Kukavica radar site with the following parameters: pulse width $\tau = 2\mu s$, antenna beamwidth $\theta_1 = 2^\circ$, antenna elevation $\theta_e = 0^\circ$, antenna speed $\alpha = 36^\circ/s$, Doppler spectrum width $\sigma_f = 20Hz$, pulse repetition interval $T_s = 5ms$, range sampling interval $\ell_r = 1/f_{smpr} = 322.58ns$, and number of averaged pulses $N = 32$.

From figure 7 one can get the equivalent number of independent samples in range space, 8.25, for typical receiver bandwidth of $B_c = 2MHz$ and from figure 8, considering the same set of radar parameters, the equivalent number of independent samples in angle and time space, 13.7. Finally, sampling in all three domains gives the equivalent number of independent samples, 112.75, as the product of the equivalent numbers of independent samples in angle and time space and range space.

CONCLUSION

Manual implementation of classical non-Doppler radar MITSUBISHI RC-34A in hail suppression activities has been used till now. Automation of this process including digital radar signal processing, radar data processing, cloud cell tracking, precise launching of rockets with seeding material, etc. increased efficiency of hail suppression system in Serbia. Proposed improved weather radar signal processing algorithm thanks to receiver calibration accuracy, taking into consideration receiver non matched bandwidth losses and propagation losses, gives more accurate estimation of equivalent reflectivity factor, the most important measure for rocket launching decisions in hail suppression system and, as a consequence, increasing system efficiency.

REFERENCES

- [1] DOVIK, J., AND ZRNIC, D.: "The weather radar equation-receiver bandwidth considerations". Preprints, 18th Radar Meteorol. Conf., Atlanta, 1978., AMS.
- [2] DOVIK, J., AND ZRNIC, D.: "Receiver Bandwidth Effect on Reflectivity and Doppler Velocity Estimates". Journal of Applied Meteorology., Volume 18, 69-76, 1979a
- [3] DOVIK R., ZRNIC D. AND SIRMAN D.: "Doppler Weather Radar", Proc. IEEE., Vol. 67, No. 11, Nov. 1979b.
- [4] DOVIK R. AND ZRNIC D.: "Doppler Radar And Weather Observation", 2nd Ed., Academic Press, 1993.
- [5] EFERICA P., VUKOVIĆ P., KOSTIĆ A., MILOVANOVIC B., RANČIĆ D., SMILJANIĆ M. AND BABIĆ Z.: "Weather Radar Signal Processing for Hail Suppression; Radar Products Enhancement and Hybrid Antenna Control Techniques", Conference on Radar Meteorology RADME98, Rome, 1998a
- [6] KERR D.: "Propagation of Short Radio Waves", McGraw Hill, 1951.
- [7] KOSTIĆ A., EFERICA P., VUKOVIĆ P., RANČIĆ D., STANKOVIĆ Z.: "An Approach to Weather Radar Signal Processing by DSP for PC", 3rd International Conference TELSIS'97, Niš, 1997a.
- [8] KOSTIĆ A., MILOVANOVIC B., EFERICA P., VUKOVIĆ P. AND RANČIĆ D.: "Weather radar signal and data processing in hail suppression system", Facta Universitatis, Vol 10, No.2, 1997b.
- [9] PROBERT-JONES, J.R., 1962: "The Radar Equation in Meteorology", Quart. J. Roy. Meteor. Soc., 88, 485-495.
- [10] ROGERS R.R. AND WALKER G. : "Autocorrelations of Detected Radar Signals", Journal of Applied Meteorology, Vol. 12, Sep. 1973.
- [11] WALKER G.B., RAY P.S., ZRNIC D., DOVIK R.: "Time, Angle and Range Averaging of Radar Echoes from Distributed Targets", Journal of Applied Meteorology, 1980.
- [12] ZRNIC D.S.: "Moments of Estimated Input Power for Finite Sample Averages of Radar Receiver Outputs", IEEE Trans. Aerosp. Electron. Syst., Vol. AES-11, January 1975a.
- [13] ZRNIC D.S.: "Signal-to-Noise Ratio in the Output of Nonlinear Devices", IEEE Trans. on Inf. Theory., Nov. 1975b.
- [14] ZRNIC, D., AND DOVIK, J. "Matched Filter Criteria and Range Weighting for Weather Radar". IEEE Trans. Aerospace Electron. Syst., AES-14, 925-930, 1978.
- [15] ZRNIC D.S.: "Estimation of Spectral Moments for Weather Echoes", IEEE Trans. on Geoscience electronics, Vol. GE-17, No. 4, Oct 1979.
- [16] NATHANSON, F.E.: "Radar Design Principles". McGraw Hill, 1969

REALIZATIONS OF A DIGITAL CLOCK RECOVERY IN A 8MBIT/S 4-FSK DIGITAL RADIO RELAY SYSTEM

Perić Dragana, Perić Miroslav
Institute IMTEL, Belgrade, Yugoslavia

Abstract - Realization of a digital clock recovery circuit (DCR) for 2 and 8Mbit/s digital radio-relay systems (DRRS) with 4-FSK modulation is described. This circuit is realized in Lattice ispLSI devices, with speed 60 MHz and 110 MHz, which means that gate delays are near phase increment of digital oscillator. The highlights of this realization are: (i) reduced influence of great zero crossing jitter, due to averaging in transition detector and (ii) work under relatively low E_b/N_0 (about 10 dB). At higher bit rates, given DCR can be used as pre-shaper for analog PLL, for extraction of a discrete component at symbol clock frequency.

I. INTRODUCTION

A. Specifics on DCR in a DRRS

Features of clock recovery circuit in DRRS are:

1. Great zero-crossing jitter caused by Nyquist filtering of four-level signal at the end of demodulator. This is most evident in cases of multilevel eye-patterns. For 4-FSK modulation this jitter varies from 0.3 UI to 0.7 UI, depending on the value of equivalent Nyquist filter's roll-off factor (α) (Fig. 1.), and
2. Work under relatively low ratios E_b/N_0 (about 10dB), because DRRS medium is susceptible to fading influence.

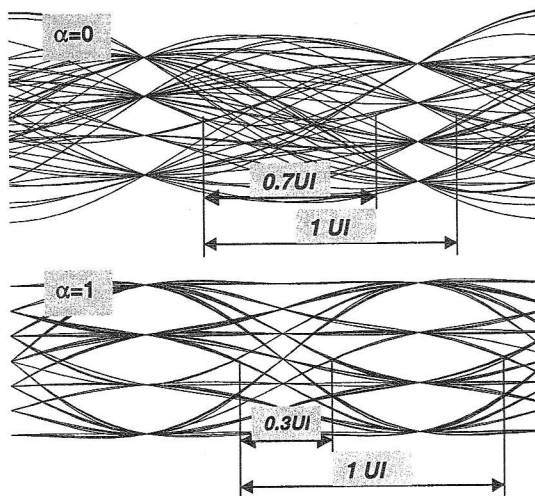


Fig. 1. Eye-patterns of 4-FSK

Joined technological problem is that a baseband processing unit is usually part of outdoor unit (ODU), so it has to work in extended temperature range

(-30°C to +55°C). For that reason, in practical realizations industrial and military grade components must be used, that inevitably increase the equipment price.

Considerable problem in practical realization of DCR is the need for several times (N) higher clock (f_{fast}) than the bit rate. Usually is $N \geq 8$. In modern equipment, DCR circuits are implemented usually up to 2.5Mbit/s (f_{fast} is up to 20MHz). At higher bit rates, typically up to 60MHz, PLL with VCXO is implemented, that is, concerning wide temperature range and aging, more costly and probably less reliable solution.

In the theory, there are numerous DCR realizations; from them most typical are [1]-[5]:

- a) with threshold-crossing detectors (usually zero-crossing)
- b) maximum likelihood estimators

Former have easier realization, but poorer behavior under low E_b/N_0 , while latter have more complex realization and often imply much higher clock than symbol rate ($N=16, 32, 64, [2],[4]$). Regardless of realization type, brought up jitter increase due to the bandwidth limiting with equivalent Nyquist filter certainly degrades DCR performance. This problem was investigated in [1], but for two-level case where this kind of jitter is less apparent (from 0 for $\alpha=1$, which is common case, to 0.55 for $\alpha=0$). For simplicity of realization, we decided for the first group.

B. General requests on DCR

Requests on DCR concerning jitter are specified under ITU-T recommendations [6]. They are:

1. *Intrinsic output jitter.* The most critical are fast jitter components (above 3 kHz) that have to be less than 0.2 UI. This means that phase increment of DCR mustn't exceed this margin.
2. *Resistance to jitter at the input ports.* DCR in line systems are usually first order, so jitter at the input ports is not a problem [5]. However, when minimizing the zero-crossing jitter by averaging, DCR bandwidth becomes narrower, the effect which degrades this characteristic.
3. *Transfer function.* Repeaters must not increase jitter at input for more than 1 dB, under assumption that artificially added jitter is much larger than intrinsic output jitter. Therefore, N should be large enough, and averaging moderate.

As one can see, requests puts on jitter performance are contradicted concerning DCR bandwidth [7].

II. PRACTICAL REALIZATION

A. Hardware

Part of DRRS's base band processing that considers digital clock recovery is shown in Fig 2.

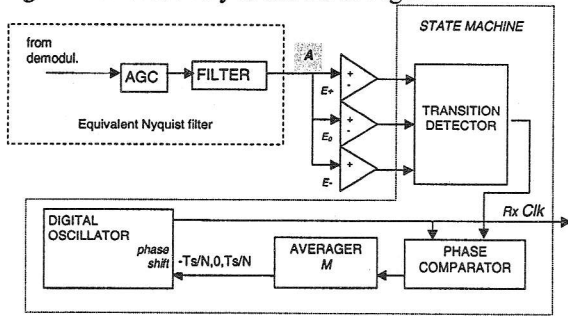


Fig. 2 Block scheme of DCR circuit

Signal from demodulator is filtered by low pass filter, therefore a signal in point A is shaped as raised cosine, which satisfies Nyquist criterion. This signal is brought to three comparators whose thresholds are settled on maximum eye opening, using an AGC circuit. Transition detector gives indication if the transition happened inside one period of the fast clock (f_{fast}). In the moment of transition, the phase of recovered clock ($RxClk$) is examined and decision is made about the phase shifting in a digital oscillator clock. Phase is shifted for a value of a quant $+Ts/N$, 0 or $-Ts/N$, where T_s is duration of a symbol interval. This decision is made after averaging of preceding $M = 2 M_{1/2} - 1$ phase comparator results. Circuit is realized as the state machine working on clock $f_{fast} = Nfs$ in Lattice ispLSI devices with maximal speed 60 and 110 MHz.

The most complex part of DCR hardware is averager. It is implemented in following way (Fig. 3):

The phase increment ($-Ts/N$, 0 or $+Ts/N$) is coded by two bits:

- CAI - indicates that phase shift exists and
- !U/D - indicates the direction of the shift

This signals are obtained from phase comparator and they are valid when transition ($TRANS=1$) occurs. The up/down counter averages them, and when it reaches a limit value of $M_{1/2}$ or $-M_{1/2}$ (second complement) it enables phase shift of digital oscillator, and another averaging cycle begins. If the counter does not reach limit values within $M = 2 M_{1/2} - 1$ transitions, the phase shift of digital clock is disabled, counters are reset and another averaging cycle begins. The averager of up to $M=13$ occupies 2.5 GLBs of Lattice chip [8], while if M enlarges up to 61 it occupies 4 GLBs. Complete DCR occupies one Lattice Megablock (8 GLBs).

B. Measurement Results

Measurements shows that in case of infinite bandwidth, without zero-crossing jitter, (e.g. directly from transmitting digital circuitry), without averaging, amplitude of the intrinsic output jitter A_{jsop} is $1/N + \delta$. It does not depend on difference between real symbol fs rate and clock f_{fast}/N ($\Delta f = fs - f_{fast}/N$) (Fig. 4.). Factor δ depends on implementation, mostly of logical devices speed, so it has slightly lower value for circuit implementation in 110MHz device (0.132UI), than for 60MHz device (0.169).

On the other hand, frequency of intrinsic output jitter (f_{jsop}) depends on Δf and can be approximately determined from the relation:

$$f_{jsop} = 1/T_{jsop} = N \cdot \Delta f \tag{1}$$

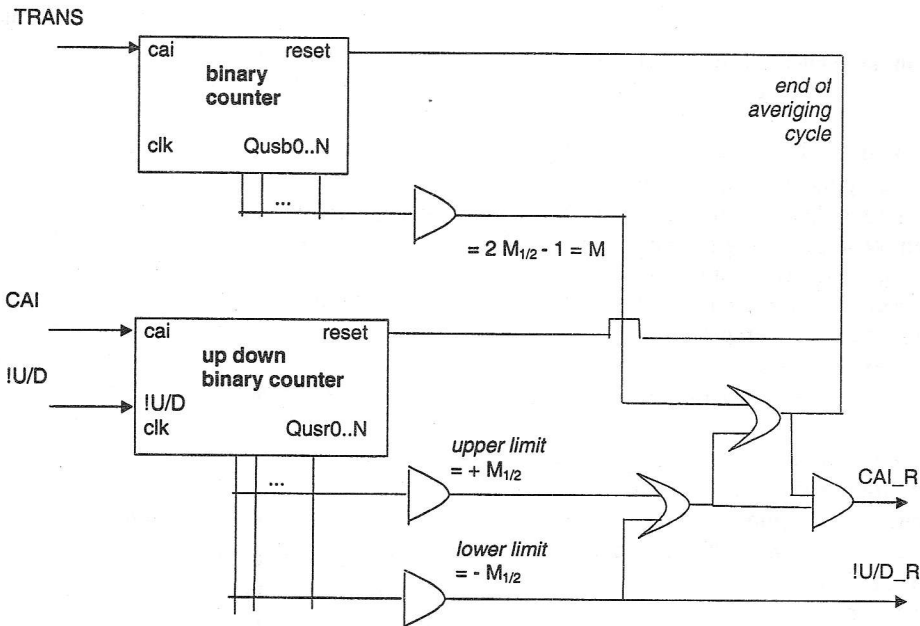


Fig 3. Averager structure

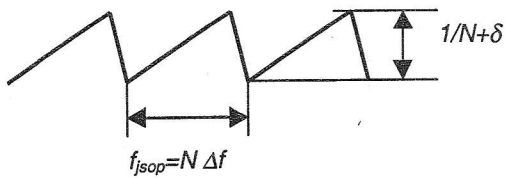


Fig. 4. Intrinsic jitter of infinite bandwidth system

But, when eye-pattern is shaped by Nyquist filter intrinsic jitter is drastically increased by increasing zero-crossing jitter (factor η). Measurement show that effect is more emphasized if zero-crossing jitter is larger than $1/N$. The components of zero crossing jitter are very fast. They are superimposed to components of infinite bandwidth DCR intrinsic jitter (Fig 5.).

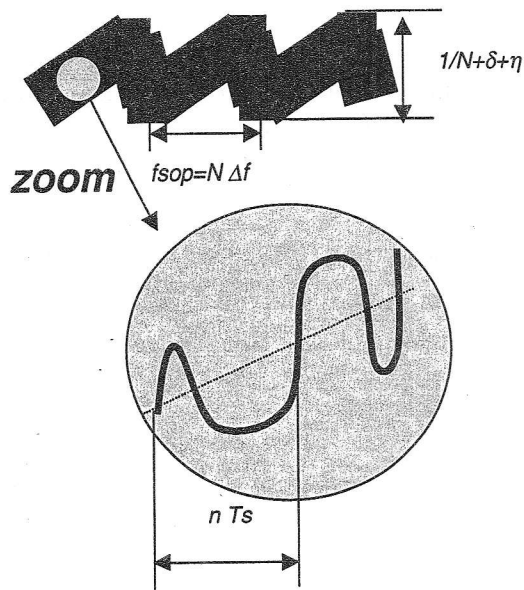


Fig. 4. Intrinsic jitter of Niquist system without averaging

This effect could be decreased, but not completely avoided by averaging (fig 6). Some amount of intrinsic jitter larger than in infinite bandwidth case still exists even for large averaging factors M ($M > 10$). It is interesting that averaging slightly decrease intrinsic jitter even for infinite bandwidth case.

The main drawback of averaging is lower resistance to incoming jitter, because of lower bandwidth of DCR, so it is not capable of tracking incoming signal (Fig 7.).

Clock recovery circuit follows jitter at the input ports without suppression in case $M=1$. At low frequencies, circuit adds jitter with factor less than 1 dB (0.8 dB at $f_{jit}=300\text{Hz}$, excited by $A_{jit}=0.8UI > 0.125UI$).

Circuit works properly until maximal distance between transitions L_{max} is much less than product of averaging factor and period of intrinsic output jitter

($M \cdot T_{sop}$), which is another reason for avoiding sufficiently large M to minimize zero-crossing jitter. L_{max} could be kept reasonably low (30 to 50) by good scrambling [9].

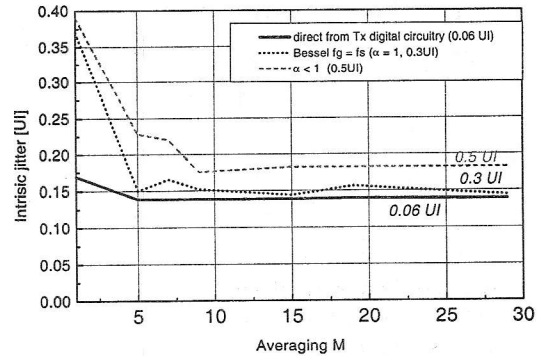


Fig. 6. Symbol recovery intrinsic jitter for DCR operation on 8Mbit/s (4Msymb/s) and $N=8$ ($f_{fast} = 32\text{MHz}$)

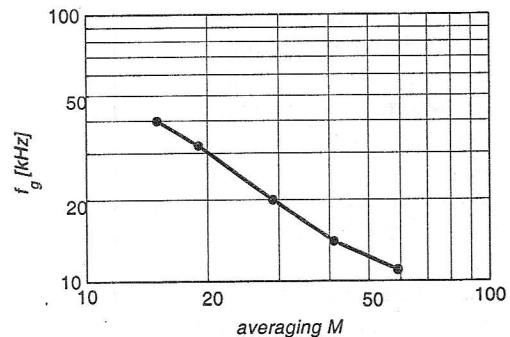


Fig. 7. DCR 3dB bandwidth

Unfortunately, intrinsic jitter at bit rate for 4-FSK case, is about twice larger than at symbol rate, for 8Mbit/s it does not satisfy ITU-T request for its high frequency components if $\Delta f = f_s - f_{fast}/N$ is too large, which practically means up to $\pm 5\text{ppm}$. This requires greater N for operation, at least 8 times bit rate, rather than symbol rate, which means around 67MHz. This bit rate is too large for realization not only in mentioned Lattice chips, and more expensive chips are required. This is the reason why this realization for 8Mbit/s remains only laboratorial experiment, but for bit rates lower than 4Mbit/s it could be easily applied. We already use this full digital DCR, with $N=16$ and $M=9$, in digital radio-relay system RRU13/2.

C. Possibility of work on higher bit rates

In the process of analogue clock recovery from a 4-level signal the most critical part is pre-shaper which has to extract discrete component on the symbol frequency. Afterwards, this component is locked in analogue PLL, which is as simpler as the extraction of

the discrete component is better. Described DCR can be used as good discrete component extractor for rates up to 6Msymbol/s in mentioned chips, but for higher rates faster chips are needed. Thus this idea could be applied for up to 12Mbit/s 4-FSK system or for 24Mbit/s 16QAM system.

Since DCR as pre-shaper gives at the output signal which frequency is the same as clock of incoming signal, phase-frequency comparator PFC [10] could be used. The main advantage of PFC is it does not require additional acquisition circuit even in a case of steep oscillator characteristic. Filter in PLL can be passive, and oscillator can be RC type with prescaling, and can have very steep characteristic (e.g.: $f_{osc}(V_{min})=0.5fs$, $f_{osc}(V_{max})=1.5fs$). This conditions could be easily achieved by '4046 or similar circuit. For this frequencies (about 10MHz) simple analogue PLL with passive filter usually has bandwidth from 3 to 50kHz, so it would suppress zero-crossing jitter and averaging is not needed. For suppressing higher intrinsic jitter components (for 8Mbit/s system this means from 3kHz to 400kHz) that comes from DCR's phase step (1/N) its frequency (f_{jso}) should be kept above analogue PLL's bandwidth. This could be done by mismatching DCR's master clock (increasing Δf), but carefully to maintain requirement:

$$L_{max} \ll M \cdot T_{sop} \approx M \cdot N \cdot \Delta f \quad (2)$$

PLL realized like this is repetitive, low-priced and easy to adjust. Such DCR circuitry we implemented in new generation of digital radio relay links RRU13/8

CONCLUSION

Described full digital DCR is experimentally realized in 8Mbit/s (4Msymbol/s) system. Amplitude of intrinsic output jitter is $1/N+\delta$ and it doesn't depend on clock difference, but on realization (delays of logical devices). Frequency of intrinsic output jitter depends on difference between real symbol rate and local oscillator clock in case of first order loop. Great zero-crossing jitter is decreased when averaging is applied in transition detector. Averaging should not be on a large number of samples because of the resistance to jitter at input ports. Measuring results show that ITU-T recommendation concerning jitter are not satisfied in case $N=8$ ($f_{fast} = 32MHz$) only for

high jitter components. For lower rates, up to 4Mbit/s, this digital DCR with $N=16$ satisfy all ITU-T recommendations. For higher bit rates (e.g. 8Mbit/s) this DCR, without averaging, can be used for extraction of discrete component at symbol frequency, that is phase filtered by simple analogue PLL, so traditional narrow band filtering for complete analogue clock recovery becomes unnecessary.

BIBLIOGRAPHY

- [1] Fogel E., Gavish M., "Performance Evaluation of Zero-Crossing-Based Bit Synchronizers", IEEE Transactions on Communications, Vol.37, No.6, June 1989.
- [2] Brugel H., Dreisen P., "Variable Bandwidth DPLL Bit Synchronizers with Rapid Acquisition Implemented as a Finite State Machine", IEEE Transactions on Communications, Vol.42, No.9, September 1994.
- [3] K.C. Chen, J. M. Lee, "A Family of Pure Digital Signal Processing Bit Synchronizers", IEEE Transactions on Communications, Vol.45, No 3, 1997.
- [4] Payzin E., *Analysis of a Digital Bit Synchronizer*, IEEE Transactions on Communications, Vol.31, No.4, April 1983.
- [5] Kalezić N., Radenović R., *Digitalno izdvajanje takta pritočnih kanala u sekundarnom plesiosinhronom multiplekseru IM8*, XL Konferencija za ETRAN, Budva, 4-7. juna 1996.
- [6] ITU-T Recommendation G.823 *Digital Networks Transmission Systems and Multiplexing Equipment* VOLUME III-FASCICLE III.3
- [7] Bellamy C. J. *Digital Network Synchronization*, IEEE Communications Magazine, April 1995., Vol 33, No 4.
- [8] Lattice semiconductor data book, January 1998.
- [9] Perić M., Perić D. *One Method for Avoiding Long Same-symbol Sequences as a Result of Self-synchronous Scrambling*, Conference Telsiks 97, p.567-660, Niš, 1997.
- [10] Gardner M.F., *Phaselock Techniques*, John Wiley & Sons, New York, 1979.



4th INTERNATIONAL CONFERENCE
ON TELECOMMUNICATIONS IN MODERN
SATELLITE,
CABLE AND BROADCASTING SERVICES

TELSIKS'99

Niš, Yugoslavia, 13-15 October 1999.



IEEE
Networking the World™

REPORT OF THE TELSIKS'99 CONFERENCE

The 4th Conference on Telecommunications in Modern Satellite, Cable and Broadcasting Services - TELSIKS'99 was held from October 13 through 15, 1999, at the Faculty of Electronic Engineering, University of Nis, Yugoslavia. It was organized by the Faculty of Electronic Engineering - Nis, Ei HOLDING Co. - Nis and Radio-Television of Serbia - Belgrade.

This year the conference was organized under the auspices of

- Serbian Academy of Science and Art
- Yugoslav Ministry of Telecommunications
- Yugoslav Ministry for Development, Science and Environment
- Serbian Ministry of Science and Technology
- Serbian Ministry of Traffic and Communications.

Having in mind that the last conference was evaluated as a high-level international meeting, TELSIKS Organizing Committee made much efforts during the time between TELSIKS'97 and TELSIKS'99 to provide the new IEEE sponsorships, in addition to *IEEE MTT-S* co-operative sponsorship, obtained earlier. First of all, MTT-S technical co-operative sponsorship was confirmed to be valid for this year conference too. Further, after a common procedure, technical co-sponsorships are obtained from *Antennas and Propagation Society (AP-S)*, *IEEE Communications Society (ComSoc)* and *IEEE Region 8* as well. In addition, for the first time, this year the Conference Proceedings is accepted as an IEEE publication. Also, IEEE Yugoslavia Section, Yugoslav Society for Microwave Techniques and Technology, Yugoslav Society for Telecommunications and others helped very much the organization of the Conference.

In the time when the preparation of the TELSIKS'99 Conference was very intensive, a war started in our country. The building of the Faculty of Electronic Engineering in Nis, where all activities about TELSIKS conference have been made, was damaged significantly by many attacks in its neighborhood. The conditions for any work at the faculty were very bad. The Organizing Committee faced with a difficult question: break preparing the conference, move the conference to the following year or go on with the preparation? It has to be noted that in that time the Conference Chairman and the Organizing Committee received many letters from the foreign participants, reviewers and other people, who wanted to express their support. Finally, the decision was made: go on! Despite such enormously difficult conditions including the problems with mail communications with other countries, the organizers almost accomplished, during the wartime, a very important job in conference organizing: the reviewing of the papers by international review board.

After the reviewing procedure and the paper selection, the Program and Organizing Committee carried out further activities in TELSIXS'99 organizing. Final manuscripts of the accepted papers were received and prepared for publishing in the Conference Proceedings. The final Conference and Workshop Program was defined.

The Conference topics were: Satellite communications, Cable communication systems, Radio communications, Mobile communication systems, Satellite and terrestrial broadcast systems, Television technique, Applied electromagnetics, Antennas and propagation, RF and microwave technique, Optical communication systems, Telecommunication and DSP integrated circuits, Modulations and Coding, Signal processing, Multimedia, Telecommunication networks, etc. TELSIXS'99 focused on modern broadcasting technologies.

122 regular contributed papers have been accepted for oral or poster presentation. In addition, a number of experts in the areas of the conference topics were asked to present their research results, so 26 invited papers were included in the Conference program. The authors of regular and invited papers were from 20 countries (USA, Canada, Japan, India, Australia, China, *New Zealand, United Kingdom*, France, Germany, *Switzerland, Poland*, Hungary, *Romania, Russia, Republic of Belarus, Ukraine, Macedonia, Bosnia & Herzegovina and Yugoslavia*).

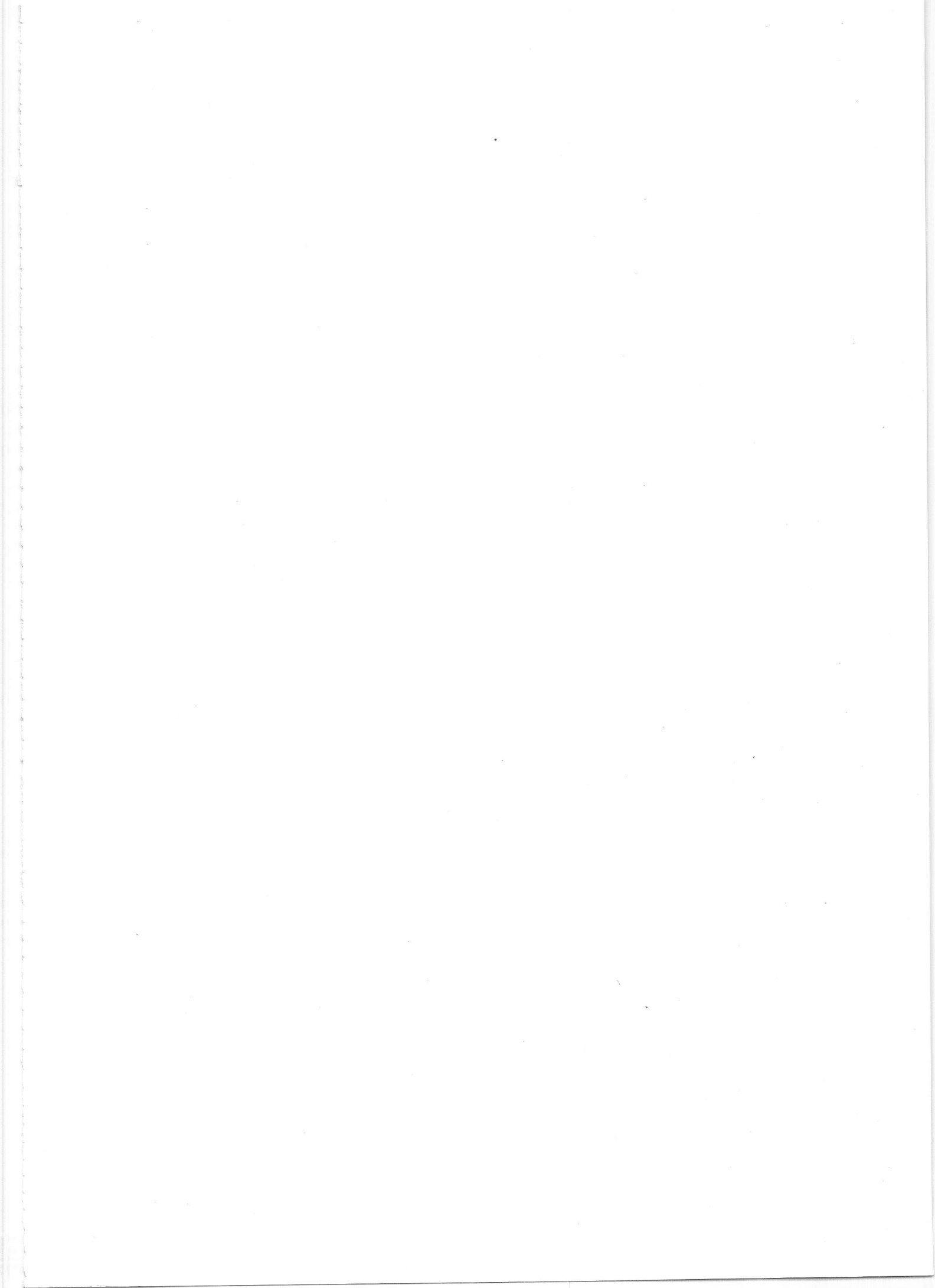
The Opening Session started by the speeches of Prof. Bratislav Milovanovic (Conference Chairman), Prof. Branimir Djordjevic (rector of the University of Nis), M.Sc. Branka Jokanovic (Chair of Yugoslav IEEE MTT Chapter), Zoran Zivkovic (Nis Mayor) and other speakers. The Conference was opened by the minister of Science and Technology of the Republic of Serbia. After that, a plenary session with two invited papers was held. First of them was a paper of Prof. Ilija Stojanovic, Academy Member, Serbian Academy of Science and Art, Belgrade, Yugoslavia. His invited paper called "*Radio at the Outset of the New Millennium*". *The second invited paper called "Human Exposure to Electromagnetic Fields from Mobile Phones" was presented by Dr. Bela Szentpali from Research Institute for Technical Physics and Materials Science, Budapest, Hungary.*

The other invited papers and the regular papers were presented in the scope of 17 parallel oral sessions and 4 poster sessions. Almost each session started by one or several invited papers. Unfortunately, it should be said that a number of participants from abroad did not attend the conference, mostly because of problems related to the sanctions applied to our country. Despite of that, the sessions were well-visited and paper presentations were followed by many useful discussions.

In addition, the technical program included a workshop which name was "*Terrestrial Broadcasting*" (in Serbian language). It was held during the second day of the conference, simultaneously with the other activities. The workshop program included three parts called: "*Law in Broadcasting*", "*Design and Equipment of Broadcasting Stations*" and "*Future of Broadcasting*". The speakers were from Yugoslav Ministry of Telecommunications, Radio-Television of Serbia and Universities of Belgrade and Nis. The workshop was followed by a round table about the state and future of broadcasting in Yugoslavia. The interest in the workshop and round table was great because of topics actuality.

The Conference was accompanied, traditionally, by an exhibition of research results and industrial products related to the Conference topics. This was an occasion for exhibitors to make many contacts with people who work in the field of broadcasting, telecommunication equipment and so on. This year 25 exhibitors took a part in the exhibition, for instance "TELEKOM-Serbia", "ELECTRONIC INDUSTRY"-Nis, "IMTEL"-Belgrade, "SKY SAT COMMUNICATIONS" from Montenegro, etc.

During the exhibition, several presentations were performed; for instance some companies as *VF-TEL SIEMENS, IMTEL, NEXT, POGLED, SkySAT, etc.* presented their



INSTRUCTIONS FOR AUTHORS

In the journal "Electronics", we publish the scientific and professional papers from different fields of electronics in the broadest sense like: automatics, telecommunications, computer techniques, energetic, nuclear and medical electronics, analysis and synthesis of electronic circuits and systems, new technologies and materials in electronics etc. In addition to the scientific, reviewal and professional papers, we present new products, new books, M. Sc. and Ph. D. theses.

In order to enable the unification of the technical arrangement of the papers, to simplify the printing of the review "ELECTRONICS", we are giving this instruction for the authors of the papers to be published in this professional paper.

The papers are to be delivered to the editor of the journal by the e-mail or to the address of the Faculty of Electrical Engineering on a floppy and printed in three folds.

All of the three folds are to be printed on one side of the paper A4 format, 210x297 mm, i.e., 8.27" width and 11.69" height, upper and lower margins of 1", left and right margins of 1" and the header and footer are 0,5". The paper may be written in Serbian or English language. Obligatory, the paper has to be written in two columns with the spacing between columns of 0.5 cm. Our suggestion to the authors is to make their papers on a PC using the word processor Word for Windows, and for the figures to use the graphic program Corel Draw. The graphs are going from the original programs, i.e. from the programs received. The papers should not be finished at the beginning of a page. If the last manuscript page is not full, the columns on that page should be made even.

The title of the paper shall be written on the first page, in bold and 12 pts size. Also, on the first page, one line space below the title, the author's name together with the name of his institution shall be printed in the letter size of the remaining parts of the text. The remaining parts of the manuscript shall be done in two columns with 10 mm space between them. The paper shall be typed with line spacing 1 and size not less than 10 pts. After the title of the paper and the name of the author, a short content follows, written in italics. The subtitles in the text shall be written in bold, capital letters of the size as in the text (not less than 10 pts). Each paper shall, at the beginning, comprise a subtitle INTRODUCTION, and, at the end, the subtitles CONCLUSION and REFERENCES. At the end of the paper, there shall be a short abstract and the title in English accompanied with the names of authors (if the paper is not written in English).

The operators and size marks that do not use numerical values, shall be written in common letters. The size marks that can use numerical values shall be written in italics. The equations shall be written in one column with right edge numeration. If the breaking of equations or figures is not desired, those may be placed over both columns.

Illustrations (tables, figures, graphs etc.) may be wider than one column if necessary. Above a table there shall be a title for instance: Table 2. *The experimental measuring results*. The same applies to figures and graphs but the accompanying text comes underneath the figure of graphs. At the end of each paper, the used literature shall be listed in order as used in the text. The literature in the text, shall be enclosed in square brackets, for instance: ...in [2] shown is...

ELECTRONICS

Vol. 3, No. 2, December 1999

CONTENTS

Guest editor	1
Preface	2
Large Signal Characterisation of Heterojunction Bipolar Transistors	3
<i>Akhil Garlapati, Sheila Prasad</i>	
MEMS Technologies for Enabling High Frequency Communications Circuits	8
<i>Victor M. Lubecke, Jung-Chin Chiao</i>	
Approximation of GaAs FET Two-Port Network z-parameters by Rational Functions.....	17
<i>Vidosav Stojanović, Saša Radovanović</i>	
HF Bipolar Integrated Circuits	23
<i>Nataša Banović, Branko Dokić</i>	
Analyses of Structure Design and Ids, Nonlinear Modeling for 5-Watt Multi-cell Microwave GaAs MESFET	28
<i>Yifan Gao, Cong Gu</i>	
Microwave FET Transistor Noise Modeling Using Neural Networks	31
<i>Vera Marković, Zlatica Marinković</i>	
MESFET Noise Modeling Based on Noise Wave Temperatures	35
<i>Olivera Pronić, Nataša Maleš-Ilić</i>	
New Generation of Millimeter-Wave Communication Systems	39
<i>Aleksandar Nestic, Veselin Brankovic, Ivana Radnovic</i>	
Novel Microwave and Millimeter-Wave Biomedical Applications	46
<i>Olga Boric-Lubecke, Yoshio Nikawa, Wesley Snyder, James Lin, Koji Mizuno</i>	
An Improved Weather Radar Signal Processing Algorithm Implemented on MITSUBISHI RC-34A Radar	54
<i>Aleksandar T.Kostić, Bratislav D.Milovanović, Predrag D.Vuković, Predrag M.Eferica, Dejan D.Rančić</i>	
Realizations of a Digital Clock Recovery in a 8Mbit/s 4-FKS Digital Radio Relay System ..	60
<i>Dragana Perić, Miroslav Perić</i>	
Report of the TELSIXS'99 Conference	64